Numerical study of the wake acceleration effect using CFD approach

Zur Erlangung des akademischen Grades
Doktor der Ingenieurwissenschaften
der Fakultät für Maschinenbau
Karlsruher Institut für Technologie (KIT)

genehmigte
Dissertation
von

M. Sc. Xiang Chai
aus Anhui, VR China

Tag der mündlichen Prüfung: 12. September 2014

Hauptreferent: Prof. Dr.-Ing. Xu Cheng

Korreferent: Prof. Dr.-Ing. Thomas Schulenberg

Karlsruher Institut für Technologie (KIT)
Institut für Fusionstechnologie und Reaktortechnik (IFRT)

Eidesstattliche Erklärung

Hiermit erkläre ich, dass ich die vorliegende Arbeit selbständig angefertigt und keine anderen als die angegebenen Quellen und Hilfsmittel benutzt sowie die wörtlich und inhaltlich übernommenen Stellen als solche kenntlich gemacht und die Satzung des Karlsruher Institutes für Technologie (KIT) zur Sicherung guter wissenschaftlicher Praxis in der jeweils gültigen Fassung beachtet habe.

Karlsruhe, 4. Juli 2014

Xiang Chai

Acknowledgements

I would like to express my gratitude to all those who helped me during the writing of this thesis. My deepest gratitude goes first and foremost to Professor Xu Cheng, for his constant encouragement and guidance. In the past several years, he has spent much time reading through each draft and provided me with inspiring advice. Without her patient instruction, insightful criticism and expert guidance, the completion of this thesis would not have been possible.

Second, I would like to express my gratitude to Professor Thomas Schulenberg, from whose valuable advice in the academic studies, I have benefited a lot and academically prepared for the thesis. Without his consistent and illuminating instruction, this thesis could not have reached its present form.

Next, I am also greatly indebted to Dr. Ivan Otic, who have instructed and helped me a lot in the past several years. It benefited from his numerous, valuable comments and the helpful discussions.I also owe my sincere gratitude to all colleagues in IFRT who help me work out my problems during the difficult course of the thesis.

I want to thank my beloved family and my wife Yi for their loving consideration and great confidence in me all through these years.

Karlsruhe, 4. Juli 2014

Xiang Chai

Abstract

Two phase bubbly flow, which is often encountered in a broad range of engineering application, plays an important role in nuclear industry. CFD approach is a very popular method to investigate flow properties of bubbly flow. Prediction accuracy is strongly dependent on interphase momentum transfer in which a correct modeling of drag force is extremely essential [99]. Despite their wide range of applications, the main challenge arising in the simulation of bubbly flow is the modeling of the complex hydrodynamic interactions between neighboring bubbles. Extensive studies have been undertaken on the fundamental understanding of this topic, and it has been recognized that the wake effect is the dominating factor responsible for the interactions between bubbles [85]. When a bubble is affected by the wake, it shows an increased rising velocity [89]. However, physical mechanism of the wake acceleration effect is not yet well understood. The present study is devoted to the development of a drag force model which considers the wake acceleration effect and its application to RANS simulation of bubbly flow.

Disregarding the influence from bubble deformation and employing several strong simplifications, several analytical and semi-analytic correlations were proposed to describe the wake acceleration effect for spherical bubbles. Most of them were devoted to examine the hydrodynamic interactions of a pair of identical bubbles rising in line. Harper [28] introduced an analytical approximation based on Moore's boundary layer approximation [50]. The vorticity diffusion between bubbles was also included in his theory. However, one noticeable drawback of his model is that it ceases to be valid as bubble diameter increases. On the other hand, several models with introduction of a new relative velocity were proposed, while the drag force of the affected bubble was evaluated by considering the same drag coefficient as a single bubble [98]. However, the physical description of an artificial factor employed in the proposed models is not yet well clarified. Its value is taken based on optimized analysis of experimental data [64, 65]. On the other hand, the separation of boundary layer is observed as bubble diameter increases. This phenomenon leads to a greater complexity of vortex structure in the wake [54]. Hence, the achievement of predicting the velocity profile of unstable wake is still quite limited. All these mentioned drawbacks reveal that the prediction accuracy of the wake acceleration effect needs further improvements when deformed bubbles and unstable wakes are involved.

Improvement of drag force modeling should be performed in two aspects. Firstly, influences from bubble deformation and unstable wake should be considered. Secondly, physical meanings of the employed factors should be clear. In the current study, based on the concept of defining a new proper reference velocity [34], a detailed investigation of velocity field around an oblate bubble was carried out. Key constitutive relation of the new drag force model was proposed, with which the relationship between the bubble increased rising velocity and the wake velocity was modeled. Hence, it is required to estimate the wake velocity profile.

In order to determine the required parameter, laminar boundary layer theory was employed to give a solution of laminar wake and CFD approach was used to provide detailed information about the turbulent wake velocity. In the current study, VOF method was employed to capture

the interface movements between bubble and liquid phase, with LES model to predict the turbulent properties in the flow field. Validation of the employed CFD approach was performed by recalculating the experimental and DNS studies of a large diameter bubble conducted by Brücker [11] and Gaudlitz and Adams [25]. It demonstrated the capability of the employed CFD approach to capture the interface movements and predict the wake properties when a deformed bubble is involved.

With the validated CFD approach, simulation and analysis of the velocity profile of turbulent wake was carried out. A close examination of wake velocity profile revealed that turbulent boundary layer theory has potential to evaluate the velocity profile of unstable wake in both vertical and radial directions. The approximation of constant turbulent viscosity [86] was also justified. Based on a systematic simulation covering a wide range of bubble diameter, correlations were proposed to provide an estimation of wake velocity profile in terms of bubble terminal velocity and bubble diameter.

The above proposed drag force model, i.e. correlations of increased bubble rising velocity and wake velocity profile, was validated against experimental and numerical results of interactive bubbles aligned in line vertically. It was also implemented into the two-fluid model. RANS model was employed to predict the turbulent properties in the liquid field. Application of the proposed drag force model was performed by recalculating experiments of bubbly flow conducted by Shawkat et al. [81] and Serizawa et al. [80]. It revealed that the proposed drag force model provides a better prediction accuracy of relative velocity than the existing models which are currently available in most CFD codes. Especially, the proposed model gives a best overall estimation with acceptable errors when the profile of relative velocity is not uniform in the radial direction. Moreover, comparing to the existing models, one important feature of the proposed model is the dependency of relative velocity on volume fraction. With the proposed approach, a more physical interpretation of the wake acceleration effect is established without introducing additional parameters.

Finally, the proposed drag force model with different BIT models was employed to assess the enhanced turbulence caused by the relative motions between bubbles and liquid phase. It revealed that the models proposed by Rzehak [70] and Morel [52] show overall the best prediction accuracy and are hence recommended to predict the bubble induced turbulence in the future work.

Zusammenfassung

Zweiphasen-Blasenströmungen sind in einer Vielzahl an technischen Anwendungen anzutreffen. Auch in der Nukleartechnik spielen sie eine wichtige Rolle. Die Numerische Strömungssimulation ist ein beliebter Ansatz, um die Eigenschaften dieser Blasenströmungen zu untersuchen. Die Genauigkeit dieser Berechnungsmethoden hängt sehr stark von der Modellierung des Momentenaustauschs der beiden Phasen ab [99]. Insbesondere die korrekte Beschreibung der sogenannten Widerstandskraft ist essenziell. Trotz der Vielzahl ihrer Anwendungsgebiete, liegt die größte Herausforderung bei der Simulation von Blasenströmungen in der Modellierung der komplexen hydrodynamischen Interaktionen zwischen benachbarten Blasen bei hohen Dampfvolumenanteilen und hohen Blasen-Reynoldszahlen. Umfangreiche Arbeiten zum Grundverständnis dieser Phänomene wurden bereits durchgeführt und kamen zu der Erkenntnis, dass der Nachlauf einer Blase der dominierende Faktor für die Bestimmung der Blaseninteraktionen ist [85]. Ist eine Blase von einer solchen Nachlaufströmung betroffen, zeigt sie eine erhöhte Auftstiegsgeschwindigkeit [89]. Der physikalische Effekt dieser Nachlaufströmung ist jedoch noch nicht vollständig verstanden. Die hier vorgestellte Arbeit widmet sich der Aufgabe ein Modell für die Widerstandskraft zu entwickeln, welches die Beschleunigung der Blasen, hervorgerufen durch die Nachlaufströmung, berücksichtigt. Des Weiteren wird die Anwendung dieses Modells anhand von RANS Simulationen von Blasenströmungen demonstriert.

Unter Vernachlässigung der Deformation der Blasen und der Annahme weiterer starker Vereinfachungen, werden einige analytische, sowie semianalytische Korrelationen zur Beschreibung des Effekts der Nachlaufströmung unter niedrigen Blasen-Reynoldszahlen vorgeschlagen. Die meisten dieser Korrelationen beschreiben die hydrodynamischen Interaktionen von sphärischen, in einer Linie aufsteigenden, identischen Blasen. Harper [28] schlug eine analytische Approximation, basierend auf Moores Grenzschicht Theorie vor [50]. Seine Theorie beinhaltet bereits die Diffusion der Vortizität zwischen den Blasen. Dieses Modell verliert jedoch seine Gültigkeit bei höheren Blasen- Reynoldszahlen. Außerdem ist die Implementierung dieses Modells in CFD Programme äußerst kompliziert. Des Weiteren wurden noch einige Modelle vorgeschlagen, die auf einer neuen Relativgeschwindigkeit beruhen, während die Widerstandskraft einer betroffenen Blase unter der Annahme modelliert wird, dass sie den selben Wiederstandskoeffizienten besitzt wie eine einzige Blase [98]. Der physikalische Hintergrund eines künstlich hinzugefügten Faktors dieses Modells bleibt allerdings noch zu klären. Der Wert dieses Faktors wird aus optimierten Analysen von experimentellen Daten gewonnen [64, 65]. Auf der anderen Seite wird die Ablösung der Grenzschicht, sowie eine instabile Nachlaufströmung bei hohen Blasen-Reynoldszahlen beobachtet . Diese Phänomene führen zu einer erhöhten Komplexität der Wirbelstruktur im Nachlauf [54]. Dies wiederum erschwert die Vorhersage von Geschwindigkeitsprofilen in instabilen Nachlaufströmungen. All dieses Missstände zeigen, dass die Genauigkeit der Modellierung des Nachlaufeffekts weiter verbessert werden muss, im Falle von deformierten Blasen oder instabilen Nachlaufströmungen.

Die Verbesserung der Modellierung der Widerstandskraft sollte unter zwei Aspekten er-

folgen. Erstens sollten die Einflüsse von deformierten Blasen und instabilen Nachlaufströmungen berücksichtigt werden. Zweitens sollte die physikalische Bedeutung der eingeführten Faktoren klar sein. In der hier vorgestellten Arbeit, basierend auf der Einführung einer neuen, richtigen Referenzgeschwindigkeit [34], wurde eine detaillierte Studie des Geschwindigkeitsfeldes um eine abgeflachte Blase durchgeführt. Der grundlegende Zusammenhang des vorgestellten Modells der Widerstandskraft ermöglicht die Modellierung der Beziehung zwischen der erhÃűhten Aufstiegsgeschwindigkeit der Blase und der Geschwindigkeit in der Nachlaufströmung. In dem hier vorgeschlagenen Modell muss das Geschwindigkeitsprofil der instabilen Nachlaufströmung angegeben werden.

Um die oben genannten Schlüsselparameter zu bestimmen, wurde der Dampfvolumenanteil zur Berechnung des vertikalen Abstandes von benachbarten Blasen benutzt, sowie ein CFD Ansatz zur detaillierten Bestimmung des Geschwindigkeitsprofils von instabilen Nachlaufströmungen. Hierbei wurde die VOF Methode zum Erfassen der Phasengrenzschicht zwischen der Blase und der flüssigen Strömung eingesetzt. Zur Turbulenzmodellierung wurde ein LES Modell benutzt. Die Validierung des eingesetzten CFD Ansatzes wurde durch Nachrechnung von experimentellen Studien, sowie von Rechnungen basierend auf DNS Simulationen einer Blase mit großem Durchmesser, durchgeführt von Brücker [11] und Gaudlitz and Adams [25], vorgenommen. Diese Nachrechnungen zeigten die Fähigkeit des hier eingesetzten CFD Ansatzes die Bewegungen der Phasengrenzschicht, sowie die Eigenschaften der Nachlaufströmung einer deformierten Blase zu bestimmen.

Mit dem nun validierten CFD Ansatz wurden Simulationen und Analysen von Geschwindigkeitsprofilen von Nachlaufströmungen bei hohen Blasen-Reynoldszahlen durchgeführt. Eine genaue Beobachtung der Geschwindigkeitsprofile von Nachlaufströmungen zeigte, dass die Grenzschichttheorie das Potential besitzt, sowohl die vertikale, als auch die radiale Verteilung der Geschwindigkeitprofile von instabilen Nachlaufströmungen vorherzusagen. Die Annahme von konstanter turbulenter Viskosität wurde ebenfalls gerechtfertigt [86]. Basierend auf systematischen Simulationen, die einen breiten Bereich von Blasendurchmessern abdecken, wurden Korrelationen vorgeschlagen, um eine Abschätzung der Geschwindigkeitsprofile der Nachlaufströmungen in Abhängigkeit der Blasen Restgeschwindigkeit, Blasendurchmesser, usw. zu bieten.

Das oben vorgeschlagene Modell zur Beschreibung der Widerstandskraft, bestehend aus Korrelationen für eine erhöhte Blasen Aufstiegsgeschwindigkeit, den vertikalen Abstand zwischen Blasen und des Geschwindigkeitsprofils von Nachlaufströmungen wurde in das Two-Fluid-Modell implementiert. Ein RANS Modell wurde genutzt, um die turbulenten Eigenschaften der flüssigen Phase zu simulieren. Angewandt wurde das hier vorgeschlagene Modell bei Nachrechnungen von Experimenten von Blasenströmungen. Diese Experimente wurden von Shawkat et al. [81] und Serizawa et al. [80] durchgeführt. Es stellte sich heraus, dass das hier vorgeschlagene Modell für die Widerstandskraft mit einer höheren Genauigkeit die Relativgeschwindigkeit vorhersagen kann, als herkömmliche Modelle, die in den meisten gängigen CFD Programmen zu finden sind. Besonders im Fall von nicht gleichförmig in radialer Richtung verteilten relativen Geschwindigkeiten, lieferte das hier vorgeschlagene Modell die beste Vorhersage mit akzeptierbaren Abweichungen. Des Weiteren ist im Vergleich zu existierenden Modellen ein besonderes Alleinstellungsmerkmal des hier vorgeschlagenen Modells, die Abhängigkeit der Relativgeschwindigkeit von dem Dampfvolumenanteil. Mit dem hier vorgeschlagenen Ansatz wurde eine physikalische Interpretation des Nachlaufeffekts aufgezeigt, ohne zusätzliche Parameter einführen zu müssen.

Letztendlich wurde das hier vorgeschlagene Modell zur Widerstandskraft zusammen mit verschiedenen Modellen zur Blaseninduzierten Turbulenz eingesetzt, um die erhöhte Turbulenz, verursacht durch die Relativbewegung der Blasen und der flüssigen Phase, zu erfassen. Es zeigte sich, dass das von Rzehak [70] sowie Morel [52] vorgeschlagene Modell im allge-

meinen die beste Vorhersagegenauigkeit besitzt. Aus diesem Grund kann dieses Modell für zukünftige Arbeiten zur Vorhersage von Blaseninduzierter Turbulenz empfohlen werden.

Contents

Acknowledgements **v**

Abstract **vii**

Zusammenfassung **ix**

List of Figures **xvii**

List of Tables **xxi**

Nomenclature **xxiii**

1 Introduction **1**

1.1 Background 1

1.2 Objectives of this study 3

2 Previous and related work **5**

2.1 Dimensionless numbers 5

2.2 Drag force modeling of a single bubble 6

2.3 Experimental studies on the wake acceleration effect 7

2.3.1 Experimental studies: a brief summary 8

2.3.2 Conclusion 13

2.4 Numerical studies on the wake acceleration effect 14

2.4.1 Numerical studies: a brief summary 14

2.4.2 Conclusion 16

2.5 Modeling approaches of the wake acceleration effect 17

2.5.1 Analytic methods 17

2.5.2 Semi-analytic methods 19

3 Modeling of the wake acceleration effect **23**

3.1 Phenomenological description and basic assumptions 23

3.2 Velocity profile in the wake . . . 26
3.2.1 Low bubble Reynolds number case . . . 26
3.2.2 High bubble Reynolds number case . . . 27
3.3 Velocity distribution around bubble . . . 28
3.4 Model equations for rising velocity . . . 30
3.5 Simulation and analysis of the wake velocity profile under high bubble Reynolds number condition . . . 32
3.5.1 Description of interface-capture methodology and turbulence modeling . 32
3.5.2 Validation calculation of the employed CFD approach with experimental and numerical data . . . 38
3.5.3 Simulation and analysis of wake velocity profile using CFD approach . . 51
3.5.4 Summary and comparison of the proposed drag force model . . . 57
3.6 Conclusion . . . 61

4 Validation of the proposed drag force model for bubbles aligned in line 63
4.1 Bubble pairs at low bubble Reynolds number . . . 63
4.2 Bubble pairs at high bubble Reynolds number . . . 69
4.3 Conclusion and discussion . . . 69

5 Application of the proposed drag force model for simulation of bubbly flow 71
5.1 Computational methodology . . . 71
5.1.1 Two-fluid model . . . 71
5.1.2 Turbulence modeling . . . 74
5.1.3 Vertical distance between neighboring bubbles . . . 78
5.2 Description of selected experiments and numerical configurations . . . 80
5.3 Prediction of flow properties of bubbly flow using the proposed drag force model 83
5.3.1 Simulation and analysis of relative velocity . . . 83
5.3.2 Simulation and analysis of bubble induced turbulence . . . 87
5.3.3 Assessment of bubble induced turbulence models selected from literature 94
5.4 Conclusion and discussion . . . 97

6 Conclusion and outlook 99

Appendix A Wake velocity profile at low bubble Reynolds number 101

Appendix B Wake velocity profile at high bubble Reynolds number 105

Appendix C Velocity distribution around an oblate bubble 107

Bibliography **111**

List of Figures

2.1 Bubble release plate configuration (Stewart [85]) 9

2.2 Typical wake acceleration event for multi bubbles taken from Stewart [85] ($T_1 < T_2 < T_3$) 9

2.3 A schematic description of the experimental setup.(Katz and Meneveau [34]) . . 10

2.4 Rise velocities of a pair of 475 μm diameter bubbles.(Katz and Meneveau [34]) . 11

2.5 Schematic sketch of the vertical water channel facility and the optical components.(Brücker [11]) 11

2.6 Illustration of skeleton of the vortex chain (Brücker [11]) 12

2.7 Rise pattern of the two interacting bubbles within the counterflow (Brücker [11]) . 12

2.8 A schematic diagram of Chen's test section (Chen and Lu [15]) 13

2.9 Drag force coefficients of the affected sphere with relations to Re_b, θ and L/d taken from Chen and Lu [15] and Chen and Wu [16] 13

2.10 Portion of the computational grid for a bubble separation 4 times the diameter. (Yuan and Prosperetti [98]) 14

2.11 Drag force coefficients of the affected bubble and equilibrium distance with relations to Re_b and L/d taken from Yuan and Prosperetti [98] 15

2.12 Sketch of the flow configuration and coordinate system (Hallez and Legendre [26]) 16

2.13 Drag and lift force coefficients at Re_b=200 and L/d=3.75 versus θ taken from Hallez and Legendre [26] 16

3.1 Two equal-sized bubbles considered in the analysis. Z direction stands for the rising direction. 25

3.2 Decomposition of the wake velocity 26

3.3 Dependency of the averaged wake velocity $\overline{U_w}$ on the vertical distance to the bubble center when Re_b varies from 3 to 35 27

3.4 Surface coordinates of an oblate bubble 29

3.5 Tangential velocity at interface of a single bubble 30

3.6 Dependence of the velocity ratio $V_{T,2}/V_{T,1}$ on the averaged wake velocity $\overline{U_w}$ and the bubble aspect ratio E 31

3.7 Sketch of the surface tension force and related parameters within the transition region 35

3.8 Sketch of the simulation domain for simulating a single bubble rising in the stagnant water 40

3.9 Prediction of bubble terminal velocities with different mesh resolutions (d=5mm) 41

3.10 Snapshot of a deformed bubble obtained in Mesh3 (d=5mm) 42

3.11 Comparison of bubble aspect ratios with different mesh resolutions (d=5mm) . . 42

3.12 Rising velocity vs. time for an air bubble rising in the stagnant water obtained in Case A and Case B 45

3.13 Terminal velocities obtained in the simulation of bubbles with different diameters and compared with experimental data reproduced from Clift et al. [17] 45

3.14 Air bubble freely rising in water (Case A) 46

3.15 Contour of the wake velocity profiles at different times (Case A) 47

3.16 Rising trajectory of the simulated bubble obtained in Case A(x,y: horizontal axes). 47

3.17 Bubble lateral movements obtained in Case A (x,y: horizontal axes). 48

3.18 Bubble lateral velocities obtained in Case A (x,y: horizontal axes). 48

3.19 Bubble acceleration rate in direction of the instantaneous motion. 49

3.20 Simulation results of bubble wake structure in Case A 49

3.21 Contour of vorticity generated by a zigzagging bubble at a time instant, colored with vertical liquid velocity 50

3.22 Vertical vorticity in the bubble wake, seen from top view 51

3.23 Sketch of the simulation domain with the selected cross sections for sampling the wake velocity profile 53

3.24 Dependence of the turbulent viscosity ν_t on the vertical distance to the bubble center s ($d = 5mm$) 54

3.25 Dependence of the characteristics velocity U_s on the vertical distance to the bubble center ($d = 5mm$) 54

3.26 Dependence of the turbulent intensity I on the vertical distance to the bubble center ($d = 5mm$) 55

3.27 Dependence of the averaged turbulent viscosity $\overline{\nu_t}$ on the drag force coefficient . 57

3.28 Radial profiles of the predicted wake velocity normalized by its maximum value and compared with the proposed correlations (d=5mm) 58

3.29 Dependence of the normalized averaged wake velocity on the vertical distance to the bubble center and compared with the results predicted by the proposed correlations 59

3.30 Comparison of the proposed model and Zhang's model [101] when Re_b= 3. . . 60

3.31 Comparison of the proposed model and Marks' model [48] when d=5 mm. . . . 61

4.1 Velocity ratio between the affected bubble and a corresponding single one with relations to L/d predicted by the proposed model and compared with the experimental data provided by Katz and Meneveau [34] 65

4.2 Drag force ratio between the affected bubble and a corresponding single one with relations to L/d predicted by the proposed model and compared with DNS results provided by Yuan and Prosperetti [98] 67

4.3 Relative strength of the inviscid and wake attraction forces: $2F_{HDI}/(F_{d1} - F_{d2})$) 68

4.4 Equilibrium distance as a function of Re_b for Re_b = 50, 100 and 200 68

4.5 Velocity ratio between the affected bubble and a corresponding single one with relations to L/d predicted by the proposed model and compared with the experimental data provided by Tsuge and Hibino [91] 70

5.1 Simplification of the relative position between neighboring bubbles in bubbly flow 78

5.2 A schematic description of the lateral distance between neighboring bubbles . . 79

5.3 Dependency of the dimensionless vertical distance between neighboring bubbles $L/\bar{d}$ on volume fraction 80

5.4 Drag force coefficient of the affected bubble $C_{d,2}$ with relations to volume fraction α and Eo number predicted by the proposed drag force model 80

5.5 Sketch of the simulation domain in the 2D computational domain 82

5.6 Measured radial profiles of bubble diamter d for the selected cases from Shawkat et al. [81] 83

5.7 Volume fraction profiles obtained with different drag force models and compared with the experimental data provided by Shawkat et al. [81] 85

5.8 Relative velocity profiles obtained with different drag force models and compared with the experimental data provided by Shawkat et al. [81] 86

5.9 Typical photograph taken from Serizawa et al. [80] to indicate the distribution of bubble diameter (Bubbly flow) 87

5.10 Volume fraction profiles obtained with different drag force models and compared with the experimental data provided by Serizawa et al. [80] 88

5.11 Relative velocity profiles obtained with different drag force models and compared with the experimental data provided by Serizawa et al. [80] 89

5.12 Comparison of measured and predicted radial profiles of the square root of turbulent kinetic energy $\sqrt{k}$ for the single phase cases from Shawkat et al. [81] . 90

5.13 Comparison of measured and predicted radial profiles of volume fraction for the two-phase cases from Shawkat et al. [81] 90

5.14 Comparison of measured and predicted radial profiles of the square root of turbulent kinetic energy $\sqrt{k}$ for the two-phase cases from Shawkat et al. [81] . . 91

5.15 Comparison of measured and predicted radial profiles of liquid velocity for the two-phase cases from Shawkat et al. [81] 92

5.16 Comparison of measured and predicted radial profiles of the axial turbulent scale for the single phase case from Serizawa et al. [80] 92

5.17 Comparison of measured and predicted radial profiles of volume fraction for the two-phase cases from Serizawa et al. [80] 93

5.18 Comparison of measured and predicted radial profiles of the axial turbulent scale for the two-phase cases from Serizawa et al. [80] 93

5.19 Comparison of measured and predicted radial profiles of liquid velocity for the two-phase cases from Serizawa et al. [80] 94

5.20 Comparison of measured and predicted radial profiles of volume fraction for the two-phase cases from Shawkat et al. [81] 95

5.21 Comparison of measured and predicted radial profiles of the square root of turbulent kinetic energy $\sqrt{k}$ for the two-phase cases from Shawkat et al. [81] . . 96

5.22 Comparison of measured and predicted radial profiles of volume fraction for the two-phase cases from Serizawa et al. [80] 96

5.23 Comparison of measured and predicted radial profiles of the axial turbulent scale for the two-phase cases from Serizawa et al. [80] 97

A.1 Axis-symmetry control volume outside the considered bubble 101

List of Tables

2.1 Summary of typical drag force models depending on Re_b 7

2.2 Summary of typical drag force models depending on Eo 7

2.3 Summary of typical experimental studies of the wake acceleration effect 8

2.4 Summary of typical numerical studies of the wake acceleration effect 14

3.1 Physical properties of the investigated air-water system under room temperature 39

3.2 Summary of dimensionless numbers for the sensitive analysis of the numerical configuration 40

3.3 Summary of total mesh numbers for the sensitive analysis of mesh resolution . 41

3.4 Summary of geometry sizes for the sensitive analysis of simulation domain . . . 43

3.5 Summary of predicted terminal velocities in the sensitive analysis of geometry size 43

3.6 Comparison of predicted aspect ratios in the sensitive analysis of geometry size 43

3.7 Summary of LES models employed in the simulation 43

3.8 Comparison of predicted terminal velocities in the study of turbulence model . . 44

3.9 Comparison of predicted aspect ratios in the study of turbulence model 44

3.10 Bubble diameters with the corresponding dimensionless numbers for validation calculation of the employed CFD approach 44

3.11 Bubble diameters with the corresponding dimensionless numbers for the study of wake velocity profile 52

5.1 Summary of parameters used in the two-phase $k-\epsilon$ turbulence model 75

5.2 Summary of time scale models considered in the following study 78

5.3 Test cases from Shawkat et al. [81] selected for the present work 81

5.4 Test cases from Serizawa et al. [80] selected for the present work 81

A.1 Balance of volume flux and momentum on the control surface in Fig. A.1 102

Nomenclature

Latin letters

$\mathbf{V}$	Velocity field in VOF method	$[ms^{-1}]$
$\mathbf{I}$	Metric tensor	$[-]$
$\mathbf{n}$	Unit vector outward normal to bubble interface	$[-]$
$\overline{u_i' u_j'}$	Velocity fluctuation	$[m^2 s^{-2}]$
$\overline{u_k}$	Mean velocity in two-fluid model	$[ms^{-1}]$
$\overline{U_w}$	Radially averaged wake velocity over bubble projected area	$[ms^{-1}]$
Φ	Velocity potential	$[m^2 s^{-1}]$
ϕ_r	Volumetrical flux through the cell face	$[m^3 s^{-1}]$
$\tilde{S}$	Characteristic filter rate of strain	$[s^{-1}]$
a	Major axis of a deformed bubble	$[m]$
$A(t)$	Instantaneous acceleration of bubble	$[ms^{-2}]$
A^+	Semi-empirical constant	$[-]$
b	Minor axis of a deformed bubble	$[m]$
C_d	Drag force coefficient	$[-]$
C_l	Lift force coefficient	$[m]$
C_S	Smagorinsky coefficient	$[-]$
C_{S0}	Van Driest constant	$[-]$
C_{vm}	Virtual mass coefficient	$[-]$
d	Equivalent Bubble diameter	$[m]$
D_e	Non-dimensional equilibrium distance between two bubbles	$[m]$
E	Aspect ratio of a deformed bubble	$[-]$
Eo	Eötvös number	$[-]$
F_B	Basset force acting on bubble	$[kgms^{-2}]$
F_d	Drag force acting on bubble interface	$[kgms^{-2}]$

F_g	Buoyancy force acting on bubble	$[kgms^{-2}]$
F_k^{drag}	Drag force in two-fluid model	$[kgm^{-2}s^{-2}]$
F_k^{lift}	Lift force in two-fluid model	$[kgm^{-2}s^{-2}]$
F_k^{td}	Turbulent dispersion force in two-fluid model	$[kgm^{-2}s^{-2}]$
F_k^{vm}	Virtual mass force in two-fluid model	$[kgm^{-2}s^{-2}]$
F_k^{wall}	Wall lubrication force in two-fluid model	$[kgm^{-2}s^{-2}]$
F_l	Lift force acting on bubble interface	$[kgms^{-2}]$
F_p	Pressure force acting on bubble	$[kgms^{-2}]$
F_w	Wall lubrication force acting on bubble interface	$[kgms^{-2}]$
F_{HDI}	Repulsive force experienced by bubble	$[kgms^{-2}]$
F_{td}	Turbulent dispersion force acting on bubble interface	$[kgms^{-2}]$
F_{vm}	Virtual mass force acting on bubble interface	$[kgms^{-2}]$
Fr	Froude number	$[-]$
G	Filter kernel	$[-]$
g	Gravitational acceleration	$[ms^{-2}]$
J_f	Superficial velocity of liquid	$[ms^{-1}]$
J_g	Superficial velocity of gas	$[ms^{-1}]$
k	Turbulent kinetic energy	$[m^2s^{-2}]$
k_{sgs}	Sub-grid scale turbulence kinetic energy	$[m^2s^{-2}]$
L	Center-to-Center distance between two bubbles in the vertical direction	$[m]$
L_{eq}	Equilibrium distance between two bubbles	$[m]$
M_k	Averaged inter-phase momentum transfer term	$[kgm^{-1}s^{-2}]$
Mo	Morton number	$[-]$
n_w	Unit normal vector perpendicular to the wall pointing into the fluid	$[ms^{-1}]$
P	Mean pressure	$[kgm^{-1}s^{-2}]$
p	Pressure	$[kgm^{-1}s^{-2}]$
P, D	Shear production and diffusion in LES model	$[m^2s^{-3}]$
R	Equivalent Bubble radius	$[m]$
Re_b	Bubble Reynolds number	$[-]$
S	Vertical distance from bubble center to the sampled surface	$[m]$
s	Vertical distance to bubble center	$[m]$
S_l^{ϵ}	Source term in ϵ_l equation	$[kgm^{-1}s^{-4}]$

S_l^k	Source term in k_l equation	$[kgm^{-1}s^{-3}]$
Sr	Non-dimensional shear rate	[–]
T_k	Laminar viscous shear	$[kgm^{-1}s^{-2}]$
T_k^{Re}	Reynolds stress term	$[kgm^{-1}s^{-2}]$
u, v, w	Velocity in x, y and z directions	$[ms^{-1}]$
U_s	Maximum value of wake velocity for every cross-section	$[ms^{-1}]$
U_w	Velocity of wake surrounding the affected bubble	$[ms^{-1}]$
u_τ	Friction velocity	$[ms^{-1}]$
U_b	Magnitude of instantaneous bubble velocity	$[ms-1]$
$u_{l,x}$	Liquid velocity parallel to the flow direction	$[ms^{-1}]$
u_L	Tangential velocity at the bubble interface	$[ms-1]$
u_{ref}	Reference fluid velocity to account for the wake effect	$[ms^{-1}]$
V	Volume of bubble	$[m^3]$
V_T	Terminal velocity	$[ms^{-1}]$
We	Weber number	[–]
y^+	Dimensionless distance from the wall	[–]
y_w	Distance to the wall	$[m]$
$\mathbf{e}_x$,$\mathbf{e}_y$	Unit vector along in x and y direction	[–]
$\mathbf{e}_z$	Unit vector along the rising direction of bubble	[–]
$\mathbf{F}_{sa}$	Surface tension force per unit interfacial area	$[kgm^{-2}s^{-2}]$
$\mathbf{F}_{va}$	Surface tension force per unit volume	$[kgm^{-2}s^{-2}]$
$\mathbf{n}$	Unit normal vector to bubble interface	[–]
$\mathbf{t}$	Unit tangential vector to bubble interface	[–]
$\mathbf{U}_r$	Relative velocity between two phases	$[ms^{-1}]$
$\mathbf{V}_r$	Velocity field to compress the interface	$[ms-1]$
$\mathbf{F}_{HD}$	Hydrodynamic force acting on the bubble interface	$[kgms^{-2}]$
$\tilde{S}_{ij}$	Large-scale strain rate tensor	$[s^{-1}]$
$\tilde{u}_i$	Filtered velocity	$[ms^{-1}]$
F_{HDI}	Repulsive force due to inviscid inertial effect	$[kgms^{-2}]$

Greek letters

α	Volume fraction	[–]
β	Factor to correct the influence from the wake velocity	[–]
Δ	Filter width	[m]
Δ_i	Grid size in the direction of axis-i	[ms^{-2}]
ϵ	Turbulent dissipation	[m^2s^{-3}]
γ	Indicator function for VOF method	[–]
κ	Curvature or Karman constant	[m^{-1}] or [–]
μ	Kinetic viscosity	[$kgm^{-1}s^{-2}$]
μ_l^{eff}	Effective kinetic viscosity of liquid phase in two-fluid model	[$kgm^{-2}s^{-2}$]
μ_l^{mol}	Laminar kinetic viscosity of liquid phase in two-fluid model	[$kgm^{-2}s^{-2}$]
ν	Dynamic viscosity	[m^2s^{-1}]
ν_t	Turbulent viscosity	[ms^{-2}]
ν_{eff}	Effective dynamic viscosity	[ms^{-2}]
ν_{sgs}	Sub-grid scale eddy-viscosity	[m^2s^{-1}]
ω	Magnitude of liquid velocity gradient	[s^{-1}]
ρ	Density	[kgm^{-3}]
σ	Surface tension coefficient	[kgs^{-2}]
σ_{TD}	Turbulent Schmidt number	[–]
τ	Viscous stress tensor	[m^2s^{-2}]
τ_t	Time scale in BIT model	[s]
τ_w	Wall shear stress	[$kgm^{-1}s^{-2}$]
τ_{ij}	Sub-grid scale stress	[m^2s^{-2}]

Superscripts

$\prime$	Small scales of flow parameter
$\tilde{}$	Large scales of flow parameter

Subscripts

1	Single bubble
2	Bubble affected by the wake
A	Point at the upper interface of bubble
b	Bubble
g	Gas phase
k	Liquid or gas phase
L	Tangential velocity at bubble upper interface
l	Liquid phase
max	Maximum value

Abbreviations

BIT	Bubble induced turbulence
CFD	Computational fluid dynamic
CPD	Cells per bubble diameter
CSF	Continuum surface force
DNS	Direct numerical simulation
LES	Large eddy simulation
MULES	Multidimensional universal limiter with explicitly solution
RANS	Reynolds-averaged Navier-Stokes simulation
SGS	Sub-grid scale
VOF	Volume of Fluid

1. Introduction

1.1 Background

Two-phase bubbly flow, which is often encountered in a broad range of engineering application including boiling water reactor, high effective heat exchanger and steam generator and so on, plays an important role in nuclear industry [93]. The knowledge of bubble behaviors involved in this flow is essential for a better understanding and design of bubbly flow system [101]. Due to the high cost of experimental study, numerical simulation is an important method to investigate flow properties of bubbly flow. The predicted parameters include both the macroscopic and microscopic phenomena which consist of flow regime,volume fraction and bubble rise characteristics, etc [17]. In the simulation, a correct modeling of interfacial forces between bubbles and liquid phase is very necessary to capture bubble behaviors in the flow field [99]. Among these interfacial forces, the drag force is the most important one, since it dominantly controls the bubble rising velocity, determines the gas phase residence time and drives the macroscopic flow patterns [61]. In order to provide a quantitative description of drag force, a dimensionless quantity named drag force coefficient C_d is introduced. It is also employed in the predictions of non-drag forces and bubble induced turbulence. Hence, an inaccurate expression of C_d limits the capabilities of numerical codes designed to predict two-phase dispersed flow, and a perfect expression of it is of importance for capturing the physics and local hydrodynamics occurring in bubbly flow correctly [46].

In the past decades, the mechanisms which govern the drag force acting on a single bubble have been investigated extensively and summarized in the work of Clift et al. [17]. At present, the motion of a single bubble in simple laminar unbounded flow is fairly well understood. It is found that C_d is only dependent on bubble Reynolds number when bubble diameter is small. As bubble diameter increases, a deformed bubble is expcted. In this case, the value of C_d is only dependent on Eötvös number [32]. Based on these findings, a lot of drag force models have been developed to predict the drag force coefficient of a single bubble rising freely in the stagnant water, and most of them provide a good agreement with experimental data [32, 50, 87, 88]. However, industrial processes are normally carried out at higher volume fractions, and it is readily acknowledged that the hydrodynamic behaviors of multi bubbles in a gas-liquid system generally differ from that of a single bubble [101]. When volume fraction and bubble Reynolds number are high, the main challenge is the modeling of the complex hydrodynamic interactions between neighboring bubbles. In this case, it is rather questionable to employ the drag force models, which are proposed for a single bubble, in the simulation of bubbly flow and further validation is required. Based on the experimental data obtained in industrial processes, several empirical correlations are proposed [82]. However, the physical description of bubble interactions is not yet clarified due to the fact that the mechanism of bubble-bubble interactions is extremely complex and a full understanding of it has not yet been reached.

Extensive studies have been undertaken on the fundamental understanding of this topic. It has been recognized that the wake effect is the domination factor responsible for the inter-

actions between bubbles [85]. Experimental studies also reveal that the wake vortices play a critical role in generating hydrodynamic forces on the bubble. Saffman [71] showed that an oscillation of the wake or a periodic discharge of vorticity underneath the bubble is the primary cause of the variation of drag force on the bubble. Moreover, when a bubble is affected by the wake (shortened as affected bubble), it shows an increased rising velocity as soon as the wake reaches it [34]. Hence, to improve the prediction accuracy of drag force coefficient which is modified by the interactions between bubbles, it is quite necessary to understand and model the mechanisms that govern the wake acceleration effect. Usually, the following methods are adopted to study this topic.

- An analytical approximation is introduced to study the modification of vorticity around the affected bubble when bubble Reynolds number is low. The vorticity diffusion between bubbles is included to obtain more reliable results [27, 28].
- With increasing computer power, the employment of the computational fluid dynamic (CFD) approach has gained considerable attentions. Significant numerical advances have been made to capture the interface movements in the simulation of multi bubbles [24, 75, 98]. The detailed information about the wake and its effect on the bubble motion is obtained by solving the mass and momentum equation.
- Experimental study is the most reliable method to investigate the wake acceleration effect. In the experiments conducted by Katz and Meneveau [34], Tsuge and Hibino [92], the increased bubble rising velocity is obtained by varying the vertical distance between neighboring bubbles as well as bubble diameter. Although the information about the wake velocity profile cannot be provided due to the limitation of measurement, the macroscopic properties of system can still be employed to investigate the wake acceleration effect.

Although all of these methods have been successfully employed in the study of the wake acceleration effect, it is still necessary to mention their noticeable drawbacks which are difficult to overcome. For the reason that the estimation of vortex property is still limited to cases at low bubble Reynolds number, the analytical method is only applicative when small bubbles are involved. Biesheuvel and Wijngaarden [7] studied the interactions between two bubbles. Multi-bubble simulations are more recent (Bunner and Tryggvason [12]). Unfortunately, CFD approach is still not capable of predicting bubble behaviors in bubbly flow, because the number of interacting bubbles is much higher in practice. In the experimental study, the strong lateral motion occurring beyond a critical size of bubble results in the problem that the measuring probe cannot focus on a single location relative to the bubble [96]. In addition, the wake structure of bubble is basically three-dimensional and unsteady, which again makes the measurement and interpretation problematic [11]. Detailed velocity measurements have been limited to experiments using small spherical bubbles, under which circumstance the wake is almost steady [23].

Due to the complex mechanisms which govern the wake dynamics, the limitation of the computational power and the difficulty on the measurement, the investigation of the wake acceleration effect is still quite limited [65]. The present study is devoted to the development of a drag force model which considers the wake acceleration effect and its application to Reynolds-averaged Navier-Stokes simulation (RANS) of bubbly flow. Key constitutive relation of the new drag force model is the modeling of the relationship between the increased bubble rising velocity and the wake velocity. In the proposed model, the velocity profile of unstable wake needs to be specified. In order to determinate the required parameter, CFD approach with the open source software package OpenFOAM is used to provide detailed information about the velocity profile of unstable wake. Correlations are also proposed to provide an

estimation of wake velocity profile in terms of bubble terminal velocity and bubble diameter. The proposed drag force model is validated against the experimental and numerical results of interactive bubbles which are aligned in line vertically. Furthermore, it is also implemented into two-fluid model and applied in RANS simulation of bubbly flow for recalculating the selected test cases conducted in pipes with different diameters.

1.2 Objectives of this study

In the present study, the wake acceleration effect will be investigated using both theoretic and CFD approaches. Based on a detailed systematical CFD analysis, the primary purpose of this study aims at the development of a new drag force model to describe the wake acceleration effect. To prove its correctness, it is validated against the experimental and numerical results. Furthermore, it is also employed in RANS simulation of bubbly flow in which high bubble Reynolds number and high volume fraction are involved. The entire study is divided into four subtasks:

(I) **Proposal of a new drag force model for the wake acceleration effect**
Based on the concept of defining a new proper reference velocity, a detailed investigation of velocity field around an oblate bubble will be carried out. A strong dependency of the increased bubble rising velocity on the bubble aspect ratio and the wake velocity can be determined, with which the influence from bubble deformation is considered.

(II) **Analysis of wake velocity profile using CFD approach**
Volume of Fluid (VOF) method will be employed to capture the interface movements between bubble and liquid phase, with LES model to predict the turbulent properties in the flow field. Validation of the employed CFD approach will be performed to demonstrate its capability to predict the wake properties at high bubble Reynolds number. A systematic CFD analysis covering a wide range of bubble diameter will be carried out, with which the velocity profile of unstable wake will be investigated in detail. Based on turbulent boundary layer theory, correlations will be proposed to describe the velocity profile of unstable wake in terms of bubble terminal velocity and bubble diameter.

(III) **Validation of the proposed drag force model for bubbles aligned in line**
The drag force model proposed in subtask I will be validated against the experimental and numerical results of interactive bubbles which are aligned in line vertically. Laminar boundary layer theory will provide us an estimation of wake velocity at low bubble Reynolds number, while the wake velocity at high bubble Reynolds number is determined by the correlations proposed in subtask II.

(IV) **Application of the propose drag force model for RANS simulation of bubbly flow**
The drag force model will be implemented into two-fluid model for recalculating the selected test cases of bubbly flows which were conducted in pipes of different sizes. Bubble induced turbulence (BIT) caused by the relative motions between bubbles and liquid phase is also assessed by the newly proposed drag force model in comparison with different drag force models which are selected from literature.

The main contribution of this study will be the development of a new drag force model for the wake acceleration effect and its application to RANS simulation of bubbly flow. Furthermore, comparing with the existing models, one important feature of the proposed model is the dependency of relative velocity on volume fraction. With the proposed approach, a more physical interpretation of the wake acceleration effect is established without introducing additional quantities.

2. Previous and related work

Due to the crucial importance of drag force, a lot of researches have been made to understand its physical mechanism and a lot of models have been established to predict the drag force coefficient of a single bubble. However, the mechanisms involved in the multi-bubble case are more complicated. Experimental observations demonstrate that the wake effect, which is responsible for the bubble-bubble interactions, leads to a sudden acceleration of the affected bubble. The increased rising velocity is strongly dependent on the bubble Reynolds number and the inter-bubble distance. However, a physical description of this phenomenon is not well clarified. In this chapter, the results of the references frequently mentioned in the study of the wake acceleration effect in the past decades are summarized and put into perspective. The dimensionless numbers which are important to describe the properties of bubble system are discussed in the first section, followed by the modeling approaches of a single bubble. After that, experimental and numerical studies on the wake acceleration effect are summarized. Finally, different modeling approaches of the wake acceleration effect are discussed.

2.1 Dimensionless numbers

In fluid mechanics, the dimensionless number is defined to give a measurement of the ratio of two forces concerned and consequently quantifies the relative importance of these two types of forces for given flow conditions. The motion of bubble in the stagnant water is governing by several forces such as: gravity force, inertial force, surface tension force and viscous force. And all these forces are related to the physical properties of both gas and its surrounding liquid. These properties includes the density ρ, the kinetic viscosity μ and the surface tension coefficient σ. The bubble rises due to the buoyancy force which is related to the gravitational acceleration g and the bubble volume V; with the latter an equivalent diameter is defined to characterize bubble size as.

$$d = \sqrt[3]{\frac{6V}{\pi}} \tag{2.1}$$

The set of dimensionless numbers, which are usually employed in the study of fluid dynamic of two phase flow includes: the bubble Reynolds number Re_b, the Eötvös number Eo, the Weber number We and the Morton number Mo. The bubble Reynolds number Re_b is the ratio of inertial force to viscous force and consequently quantifies the relative importance of the inertial force and the viscous force as:

$$\mathrm{Re_b} = \frac{\rho_l V_T d}{\mu_l} \tag{2.2}$$

where subscript g and l stand for the gas and liquid phases, respectively. V_T denotes the bubble terminal velocity. The Eötvös number Eo is regarded as proportional to buoyancy force divided by surface tension force and used to characterize the shape of bubble.

$$\mathrm{Eo} = \frac{\Delta\rho g d^2}{\sigma} \tag{2.3}$$

where $\Delta\rho$ is the density difference between gas and liquid phase. The Weber number *We* is thought of as a measure of the relative importance of the fluid's inertial compared to its surface tension. This quantity is often useful in analyzing fluid flow where there is an interface between two different fluids.

$$We = \frac{\rho_l V_T^2 d}{\sigma} \tag{2.4}$$

2.2 Drag force modeling of a single bubble

Although the drag force modeling of a single bubble is not the subject of this thesis, investigations of this topic still provide us general information about how to estimate the value of drag force coefficient, especially when bubble diameter varies over a wide range. For a single bubble, its rising velocity only depends on the surrounding flow which is generated by its motion. If considering a bubble composed of incompressible and Newtonian fluid, the hydrodynamic force acting on its interface $\mathbf{F}_{HD}$ can be obtained by employing the momentum conservation equation for a steady state. It follows that (Noca [59]):

$$\mathbf{F}_{HD} = \oint_S \mathbf{n} \cdot (-p\mathbf{I} + \tau) dS \tag{2.5}$$

Here, the momentum rate of change of contained fluid inside the bubble is neglected. $\mathbf{n}$ is the unit vector outward normal to the interface S. p is the pressure. $\mathbf{I}$ and τ are the metric tensor and the viscous stress tensor, respectively. For an incompressible Newtonian fluid, τ is usually evaluated by the following relationship (Batchelor [5]):

$$\tau = \mu_l \left(\nabla u_l + \nabla u_l^T \right) \tag{2.6}$$

where u_l stands for the liquid velocity. Eq. 2.5 provides us an analytic expression to evaluate the hydrodynamic force acting on a bubble. However, the lacking knowledge of flow properties in the industrial process limits its application. Instead, the time-averaged flow properties are predicted in RANS simulation of bubbly flow in which the hydrodynamic force acting on the bubble is decomposed into fives parts. Different effects from the liquid on the dispersed bubbles are considered. It is shown as:

$$\mathbf{F}_{HD} = F_d + F_l + F_{vm} + F_w + F_{td} \tag{2.7}$$

Here, F_d, F_l, F_{vm}, F_w and F_{td} stand for drag force, lift force, virtual mass force, wall lubrication force and turbulent dispersion force, respectively.

To illustrate the dependency of drag force, Eq. 2.5 is rewritten with an assumption that the relative direction of the bubble motion compared to liquid is parallel to the z-axis of the bubble. The lift, wall lubrication and turbulent dispersion forces are perpendicular to the motion of bubble relative to the liquid. In addition, the virtual mass force is proportional to the relative acceleration between bubble and liquid phase. So that, when a bubble reaches its steady state, its rising velocity is only dependent on the drag force which acts in the vertical direction. Thus, the vertical component of the hydrodynamic force evaluated on the bubble surface becomes:

$$F_d = \mathbf{F}_{HD} \cdot \mathbf{e}_z = \oint_S \mathbf{n} \cdot (-p\mathbf{I} + \tau) \cdot \mathbf{e}_z dS = -\oint_S \mathbf{n} \cdot p\mathbf{I} \cdot \mathbf{e}_z dS + \oint_S \mathbf{n} \cdot \tau \cdot \mathbf{e}_z dS \tag{2.8}$$

where $\mathbf{e}_z$ is the unit vector along the z-axis. From Eq. 2.8, it is illustrated that the drag force is composed by two parts. The first term on the right hand side is caused by the uneven distribution of pressure around the moving bubble and dependent on bubble size and shape. It is called form drag. The second term is dependent on the viscous stress acting on the bubble

interface and leads to a viscous drag caused by fluid viscosity. Hence, the drag force models can be classified into two groups due to the fact that magnitudes of the form and viscous drags vary with Re_b and Eo.

As summarized in Tab. 2.1, the first group of drag force models is only dependent on Re_b. When Re_b is in the order of $O(10)$, which is usually called "Stokes flow", the drag force coefficient is inversely proportional to Re_b. Later, it was suggested to introduce a multiplier factor into the Stokes law to consider the inertial and viscous effects on the drag force coefficient as proposed by Schiller and Naumann [77] and Moore [50].

Author	Drag force coefficient expression
Stokes [5]	$C_d = \frac{24}{Re_b}$
Schiller and Naumann [77]	$C_d = \begin{cases} \frac{24}{Re_b}\left(1 + 0.15 Re_b^{0.687}\right) & Re_b < 1000 \\ 0.44 & Re_b \geq 1000 \end{cases}$
Moore [50]	$C_d = \frac{48}{Re_b}\left(1 - 2.21 Re_b^{-0.5}\right)$

Tab. 2.1: Summary of typical drag force models depending on Re_b

As summarized in Tab. 2.2, the second group of drag force models is dependent only on Eo. When Re_b is sufficiently large, the separation of boundary layer and the generation of vortices happens, which results in an increase of the form drag. According to the work done by Ishii and Zuber [32] and Tomiyama et al. [87] when Re_b is sufficiently high, the drag force almost exactly comes from the form drag due to the start of the flow separation and the viscous drag can be neglected.

Author	Drag force coefficient expression
Ishii and Zuber [32]	$C_d = \frac{2}{3}\sqrt{Eo}$
Tomiyama [87]	$C_d = \max\left\{\min\left[\frac{24}{Re_b}\left(1 + 0.15 Re_b^{0.687}\right), \frac{72}{Re_b}\right], \frac{8}{3}\frac{Eo}{Eo+4}\right\}$

Tab. 2.2: Summary of typical drag force models depending on Eo

To sum up, the mechanisms that govern the drag force acting on a single bubble is researched extensively. It is clearly indicated that the existing drag force models can be arranged into two groups, those dependent on Re_b and those dependent on Eo. When bubble diameter varies over a wide range, different drag force models need to be selected to provide a reasonable estimation of drag force coefficient.

2.3 Experimental studies on the wake acceleration effect

The physical mechanism of the wake acceleration effect is quite complicate, especially in the multi-bubble cases. Since the operation condition in the real industrial process has high volume fraction, high Re_b and a higher turbulence level, a full scale experimental investigation of the wake acceleration effect is time- and cost-demanding and faces extremely difficulties of measurement. Instead, two or several bubbles which are aligned in line vertically and rise together in the stagnant water are often studied in the experimental and numerical studies. The advantage of this method lies in the fact that the lateral interactions between bubbles can be neglected in the analysis. And most of all, this method is characterized by its simplified operation and reduced experimental requirements if compared with the investigations of a

cluster of bubbles which rise together. Furthermore, the effect from turbulence in the liquid field is not included in the current study, even if it is found that the interactions between bubbles are much stronger if more bubbles and higher liquid turbulence are involved. It is assumed that some characteristic trends and conclusions obtained in the simplified experiment can still reveal the complex mechanism which governs the wake acceleration effect in the industrial processes. To reveal some fundamental information of the wake effect, the experiments which are conducted to investigate the drag force acting on a sphere immersed in the wake are also included in the summary.

In this section, the references frequently mentioned in the study of the wake effect are classified into four parts. At the very beginning, experiments were conducted to study dynamic behaviors of multi-bubbles and reveal that bubble wake is the main driving force for bubble-bubble interactions, as discussed in Stewart [85]. Consequently, several experiments were carried out to quantitatively study the wake acceleration effect, as described by Katz [34].To identity the physical mechanism of the wake acceleration effect, Brücker [11] proposed a detailed quantitative investigation of the flow filed in the bubble wake. Finally, Chen[15] investigated the wake effect with different distances and various angles. Some important parameters of typical studies are summarized in Tab. 2.3.

Author	Stewart [85]	Katz [34]	Brücker [11]	Chen [15]
Re_b	100∼400	0.5∼35	1181	10∼200
Eo	6∼28	0.006∼0.03	3.66	-
Liquid	Sugar water	Distilled water	Demineralized water	Glycerin/water mixture
No. of bubbles	Up to 16	2	2	2

Tab. 2.3: Summary of typical experimental studies of the wake acceleration effect

2.3.1 Experimental studies: a brief summary

To reveal the mechanism which governs the dynamic behaviors of multi bubbles, experimental studies were conducted to investigate how freely rising bubbles approach each other and make contact. They were motivated to make the details visible in a simplified system while containing enough bubbles to represent a true swarm. Several experiments were conducted for this purpose. Crabtree and Bridgwater [18] measured the bubble positions and bubble coalescence time for the relative motion of two vertical aligned spherical-cap bubbles of different diameters. Nevers and Wu [57] conducted a similar study on the coalescence of spherical-cap bubbles of 1-3 cm diameters rising in glycerin and in water.

More recently, an experiment was conducted in 1995 by Stewart [85] to describe the qualitative behavior of bubbles interacting in pulsed swarms of ellipsoidal bubbles. The test section is composed by a rectangular tank 20×20 cm square and 2 m high. A rotating plate provided up to 16 bubbles in a staggered square array is shown in plan view in Fig. 2.1. The swarm was released by rotating the fill plate in the horizontal plane with a stepper motor to align each fill position with matching exit holes in a cover plate above it. The maximum bubble size ranged from 0.65 to 1.28 cm equivalent diameter with Eo number from 6 to 28. With the help of a 8 mm video camera that traversed to follow the rising swarm, bubble interactions were recorded and studied in detail by viewing each run frame-by-frame.

The experimental observation indicated a clear dependence of bubble interactions upon the wake and suggested that the wake was the driving force and sole mechanism for bubble interactions. No interaction occurred except involving the wake. As shown in Fig. 2.2, when bubbles entered the rising column of liquid in the wake generated by the leading one, the

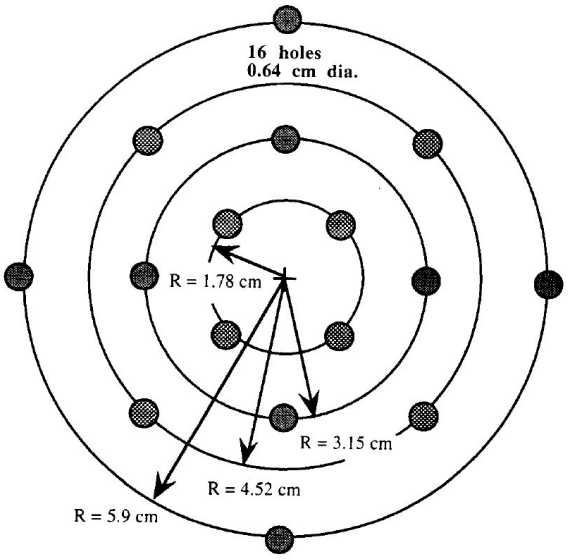

Fig. 2.1: Bubble release plate configuration (Stewart [85])

affected bubble exhibited a sudden acceleration and began overtaking the leading one immediately. At last, the affected one caught up with the leading one to an overtaking collision. One further important observation was also indicated in Fig. 2.2. Bubbles tended to accumulate together and formed a bubble "chimney" in which a cluster's wake was strong enough to sustain itself. Because of the wake capture process, new bubbles were gathered by the cluster and bubbles dispersed outward at the top were replaced during this dynamic procedure. Therefore a steady cluster of bubble was formed in the experiment. However, this study only showed a possible way to improve the modeling of drag force. No quantitative data was provided in the experiment.

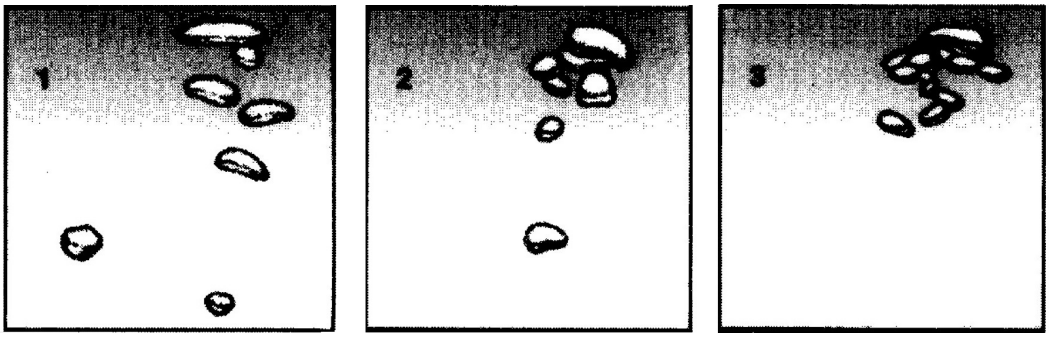

(a) Time T_1 **(b)** Time T_2 **(c)** Time T_3

Fig. 2.2: Typical wake acceleration event for multi bubbles taken from Stewart [85] ($T_1 < T_2 < T_3$)

To quantitatively study the wake acceleration effect, several experiments were conducted to measure the increased rising velocities of bubbles immersed in the wake, in which the vertical distance between neighboring bubbles varied. Marks [48] measured the rising velocities of air bubbles rising in a chain through distilled water, tap water and sugar water. Narayanan et al. [56] measured the rising velocities of air bubble pairs in aqueous glycerin solutions at Re_b of 0.5-80. Omran and Foster [60] measured the terminal velocities of chains of spherical air bubbles rising in aqueous glycerin solutions for the ranges of Re_b<1 and 1<Re_b<9 and bubble diameters from 1.4 to 3 mm.

More recently experimental work was conducted by Katz and Meneveau [34] in 1995 in which the mechanisms that cause bubbles to approach each other were studied. The rising

velocities of nearly spherical air bubble pairs rising in the stagnant water were measured. A schematic description of the experimental setup is presented in Fig. 2.3. In the experiment, bubble pairs were generated and injected into a square, 15 cm wide and 1 m long, vertical, transparent chamber. Silhouette images of bubbles were recorded with a CCD camera connected with a SVHS recorder. The displacements and distance between bubbles were measured by selecting two small sections of the image enclosing the desired bubbles and cross-correlating them. The velocity was determined by dividing the displacement of a bubble by the delay between video frames.

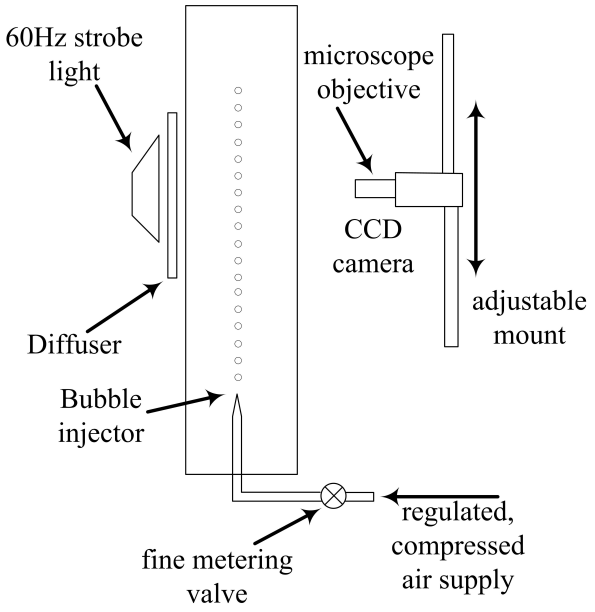

Fig. 2.3: A schematic description of the experimental setup.(Katz and Meneveau [34])

As shown in Fig. 2.4, the rising velocity of the affected bubble obtained in the experiment was dependent on its instantaneous distance from its neighboring bubble. Here, L denotes the center-to-center distance between two bubbles. It was clearly shown that the rising velocity of the affected bubble increased as its relative distance decreased. The wake-induced approach of vertical aligned bubbles was sufficiently powerful to overcome any reaction force caused by pressure gradient, culminating in coalescence for the entire range of Re_b considered. Fig. 2.4 also indicated that the leading bubble was not affected significantly by the presence of the affected bubble until the distances between them was smaller than 3 bubble diameters. This observation confirmed the finding obtained by Kok [36]. However, the entire range of Re_b considered in the experiment was greatly smaller than those of the industrial processes and the influence from bubble deformation, which is widely observed in the studies of bubbly flow, was not considered in this study.

Since the wake effect is recognized as the sole mechanism which governs bubble interactions, the wake property becomes a very important factor to identity the physical mechanism of the wake acceleration effect. Bhaga and Weber [6] measured the wake velocity behind a single spherical-cap air bubble and visualized the in-line motion of two bubbles rising in aqueous sugar solutions provided for $10<Re_b<100$. In the experiment by Komasawa et al. [38], both a single and a pair of spherical-cap air bubbles which were held stationary in downward flow of deionized water and water-jelly solutions were studied to provide a description of laminar wake. The velocity distribution induced by a chain of air bubbles was studied in aqueous glycerin and glycerin-ethanol solutions by Toshiro et al. [89], together with the shape and wake volume of the bubble chain over the range of bubble equivalent spherical diameters of 0.214 to 2.3 cm.

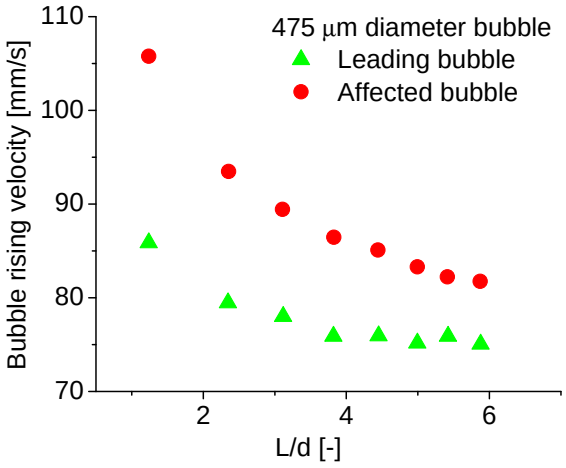

Fig. 2.4: Rise velocities of a pair of 475 μm diameter bubbles.(Katz and Meneveau [34])

The most detailed quantitative analysis of the evolution of the flow field in the bubble wake and its correlation to bubble interactions were undertaken in 1999 by Brücker [11]. The experiments focused on the mechanism of wake-driven interactions between ellipsoidal bubbles of diameter from 0.4 to 0.8 cm. The vertical water channel had a cross section of 10×10 cm^2 and was 1.2 m high. As shown in Fig. 2.5, bubbles were released from the bottom and held stationary in vertical position by an imposed counterflow. The flow field in the bubble wake was recorded with a digital high-speed camera and evaluated frame-by-frame with the method of digital-particle-image velocimetry.

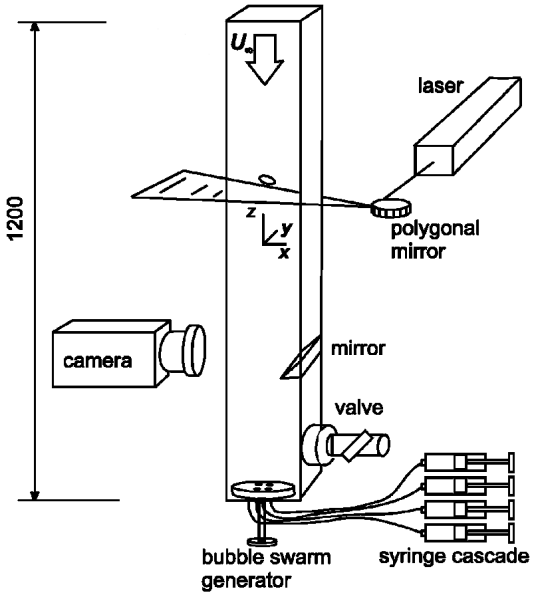

Fig. 2.5: Schematic sketch of the vertical water channel facility and the optical components.(Brücker [11])

In the experiment with two simultaneous released bubbles, it was indicated that bubble interactions were strongly triggered by the wake dynamics. A sketch of the skeleton of the vortex structures was displayed in Fig. 2.6 to indicate the location and orientation of the head loops of the hairpin vortices. Fig. 2.7 showed the vertical coordinates of two interacting bubbles in the counter flow. It was indicated that the motion of the affected bubble was strongly influenced by the wake of the leading bubble while the leading bubble remained nearly unaf-

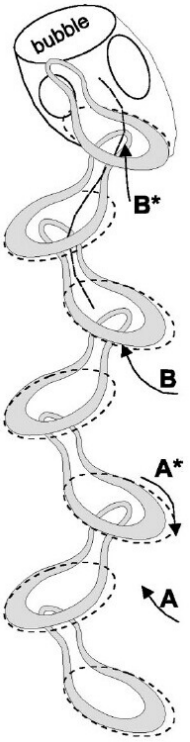

Fig. 2.6: Illustration of skeleton of the vortex chain (Brücker [11])

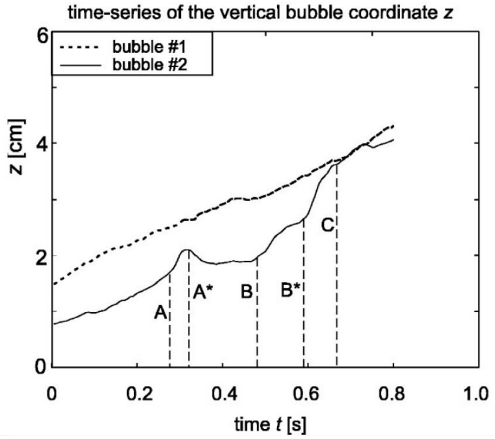

Fig. 2.7: Rise pattern of the two interacting bubbles within the counterflow (Brücker [11])

fected until shortly before collision. When a bubble was captured in the wake, its motion in the vertical direction is not continuous as the bubble was alternately accelerated and decelerated in response to the passing of the head loops of the hairpin vortices until the moment of collision. This phenomenon was explained by the induction effect of the ring-like heads of the hairpin vortices being shed from the leading bubble and was dependent on the time within the shedding cycle and the location at which the affected bubble laterally approached the wake of the leading bubble. This fouding was consistent with the experimental observation of Stewart [85] while Manga and Stone [47] found that the acceleration of the affected bubble was more continuous at low bubble Reynolds number. Overall, the results demonstrated that the wake capturing process was strongly coupled to the periodic shedding which triggered the probability of collision and coalescence. These observations could possibly help to develop a more accurate drag force model for the simulation of multiphase flows.

To summarize the work contributed to the study of influence from the leading sphere with different sizes and distances, especially located at various angles, the experimental study conducted in 1999 by Chen and Lu [15] and in 2000 by Chen and Wu [16] are summarized. The drag force and the flow characteristics of a sphere immersed in the wake were investigated. Measurements were conducted for two spheres separated with the various distance ($1 < L/d < 6$) and angles (from 0° to 180°). The definition of separation angle and distance is schematically shown in Fig. 2.8. The force acting on the affected sphere was measured by a high-precision electronic balance in the experiment.

As shown in Fig. 2.9, the drag force coefficient of the affected sphere C_d is normalized by the drag force coefficient of a single sphere C_{d0}. It was indicated that the value of the drag force coefficient of the affected sphere is greatly reduced under the influence of the leading sphere. It decreases as the inter-particle distance decreases. The influences from the various angles between two spheres are also included in Fig. 2.9. At $\theta = 180°$, total drag force of the affected sphere was decreased due to a reduction in the form drag component caused

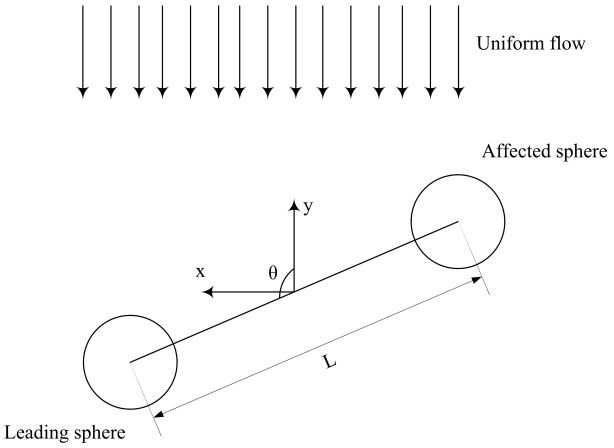

Fig. 2.8: A schematic diagram of Chen's test section (Chen and Lu [15])

by the suppression of the wake by the leading sphere. The drag force recovered quickly and was augmented to reach a maximum value with response to the continuous decrease in the inter-particle angle. This maximum value can be as large as 1.2 times of the drag force of a non-interactive sphere. Thereafter, the drag force was suddenly reduced as the inter-particle angle was continuously decreased. The drag force reached its minimum value at $\theta = 0°$ where the leading sphere locates right upstream to the affected sphere. Furthermore, by extrapolating Fig. 2.9, it was demonstrated that the affected sphere cannot fully eliminate the influence of the leading sphere until $L/d \geq 10$. This founding agreed well with the work by Rowe and Henwood [66].

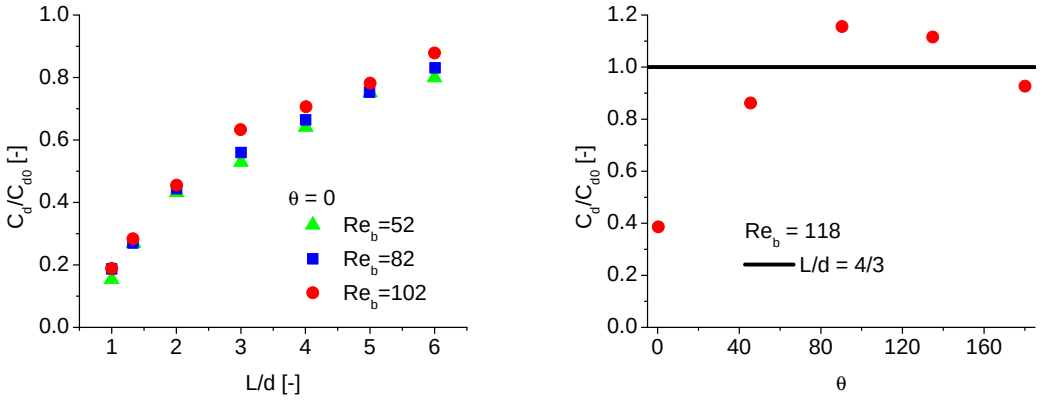

(a) Influences from Re_b and L

(b) Influence from θ

Fig. 2.9: Drag force coefficients of the affected sphere with relations to Re_b, θ and L/d taken from Chen and Lu [15] and Chen and Wu [16]

2.3.2 Conclusion

To sum up, the wake acceleration effect has been widely reported and confirmed in various experimental investigations. Although the information provided by lots of experiments is limited by the measurement, it is still found that wake effect is the sole mechanism leading to the interactions between bubbles. In the experimental studies, this phenomenon is called "wake capture". The affected bubble experiences a sudden acceleration when it is captured by the wake. Otherwise no interaction is observed in the experiment. Furthermore, it is also

found that the increased rising velocity of the affected bubble depends on Re_b and the vertical distance between neighboring bubbles.

2.4 Numerical studies on the wake acceleration effect

Lots of work was conducted to numerically study a spherical or deformed bubble by Brabston and Keller [9] and Ryskin and Leal [69], while numerical studies were also available of the dynamics of one, two, or more non-slip rigid spheres (Lee and Sirignano [40] and Ramachandran et al. [63]). As the first noticeable study on the interactions between two bubbles, the motions of two equal-size spherical bubbles moving along their centerline were obtained numerically by Yuan and Prosperetti [98] in 1994. Recently, Hallez and Legendre [26] performed a numerical study on the three-dimensional flow around two spherical bubbles moving in a viscous fluid with different distances and various angles. The numerical configurations used by Yuan and Hallez are summarized in Tab. 2.4.

Author	Yuan [98]	Hallez [26]
Re_b	20~200	50~500
L/d	1.5~30	1.25~5
Bubble shape	Spherical	
Numerical method	Mixed spectral and finite difference scheme	Finite volume method with a staggered mesh
Boundary condition	Free slip for interface	Fixed value for boundaries far from bubble Shear-free condition for interface
Mesh	Bispherical coordinate with 300 finite-difference points	Three-dimensional gird obtained from the streamlines
Remarks	Gas inertial is neglected	

Tab. 2.4: Summary of typical numerical studies of the wake acceleration effect

2.4.1 Numerical studies: a brief summary

The computational grid employed in the simulation of Yuan and Prosperetti [98] are schematically shown in Fig. 2.10. In order to distinguish the drag force from the inviscid force, the governing equation was first solved with zero-vorticity to obtain the inviscid force. Analogously, the sum of the drag force and the inviscid force were obtained by solving the full Navier-Stokes equations.

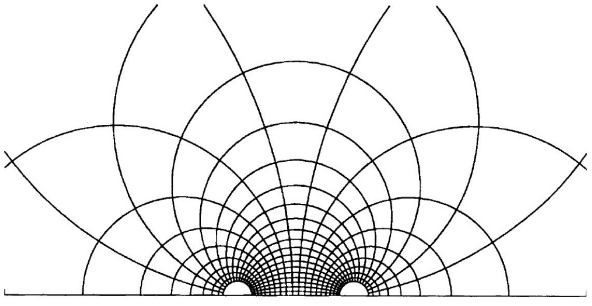

Fig. 2.10: Portion of the computational grid for a bubble separation 4 times the diameter. (Yuan and Prosperetti [98])

The drag force coefficients of the leading and affected bubbles are shown in Fig. 2.11. It was indicated that the drag force acting on the affected bubble is reduced by the wake generated by the leading one in which the affected bubble was immersed. It was found that the reduced drag force acting on the affected bubble was governed by a very complex mechanism due to the transport and diffusion of vorticity shed by the leading one. The dissipation function based on potential flow proposed by Sangani and Didwania [74] is not capable of predicting the reduced drag force coefficient. The results also showed that the drag force on the affected bubble increased monotonically as the separation between two bubbles increased. As the distance between two bubbles increased further, the drag force of the affected bubble evidently tended asymptotically to that of a single bubble. Furthermore, as shown in Fig. 2.11, the equilibrium distance, which stands for the balance between the reduced drag force and the inviscid force caused by the higher pressure in the gap between two bubbles, was found to be a function of Re_b. This observation had a good agreement with the study of Harper [27]. However, this equilibrium distance was in marked contrast to experiments [34] in which bubbles were invariably found to catch up with each other and collide. It was concluded that the most likely explanation of this discrepancy was to be found in the shape deformations induced by the flow which were different for the two bubbles.

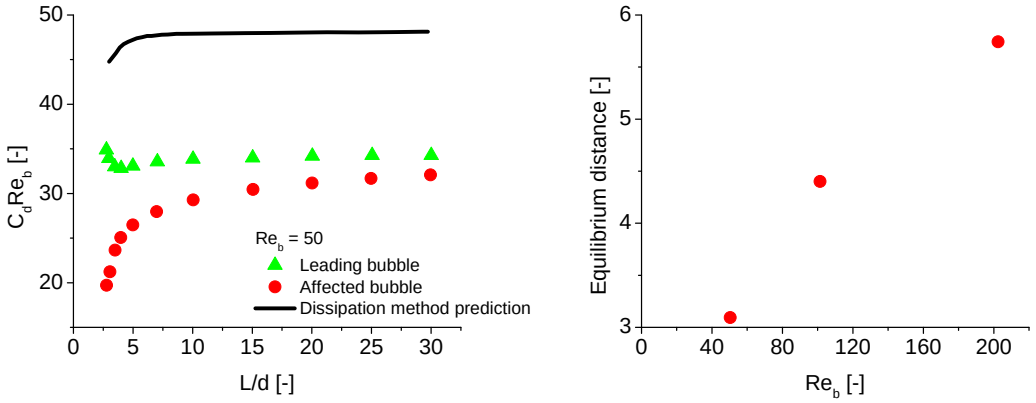

(a) Drag force coefficient

(b) Equilibrium distance

Fig. 2.11: Drag force coefficients of the affected bubble and equilibrium distance with relations to Re_b and L/d taken from Yuan and Prosperetti [98]

In the simulation of Hallez and Legendre [26], the angle θ ($0° \leq \theta \leq 90°$) formed between the centerline and the direction in the direction of the motion is shown in Fig. 2.12. A general description of the interactions for two bubbles moving side by side ($\theta = 90°$) and for two bubbles moving in line ($\theta = 0°$) were obtained.

Based on the simulation results, it was indicated that the interactions between two bubbles are governed by the combination of three effects, a potential effect, a viscous correction and a significant wake effect. Both the drag and the lift forces of the affected bubble are modified. As shown in Fig. 2.13, the variation of the drag force coefficient is quite similar to the experiments of particles [16]. The maximum drag reduction was observed for the in-line configuration. Lift force coefficients are also shown in Fig. 2.13 versus the angle θ. For $\theta \gtrsim 62°$, the lift force coefficient of the leading bubble is larger than that of the affected bubble, corresponding to an attraction along the $x-$direction. Furthermore, the lift and drag forces are decomposed to provide information on the evolution of the relative orientation of the two bubbles. It was indicated that the in-line configuration was unstable according to the negative torque whatever θ, Re_b and L. It agreed with the theories of Harper [27] and Auton [4] for the vorticity-induced effect on spherical bubbles with clean surface. Nevertheless, stable lines of bubbles were

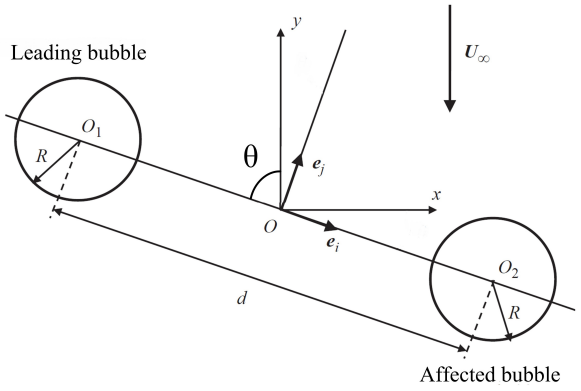

Fig. 2.12: Sketch of the flow configuration and coordinate system (Hallez and Legendre [26])

still observed in controlled experiments of Katz and Meneveau [34] and Sanada et al. [73]. They concluded that this stability may be an effect of deformation from a spherical shape or of surface contamination.

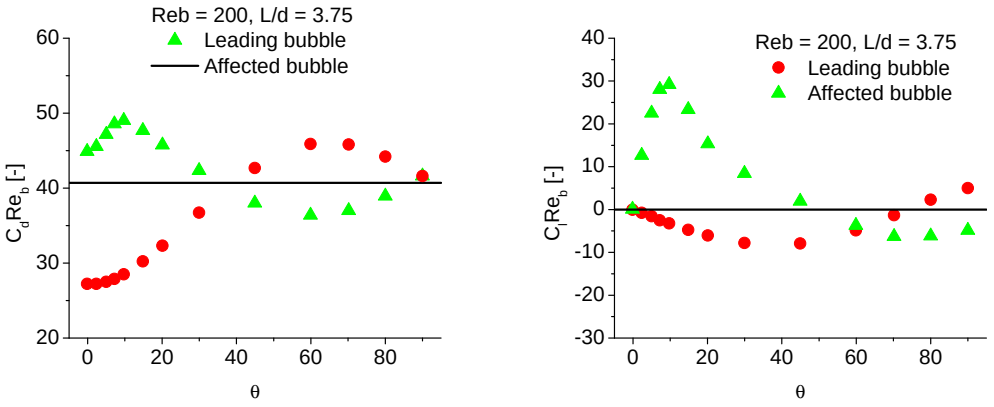

(a) Drag force coefficient

(b) Lift force coefficient

Fig. 2.13: Drag and lift force coefficients at Re_b=200 and L/d=3.75 versus θ taken from Hallez and Legendre [26]

2.4.2 Conclusion

Despite the large differences in the experimental and numerical investigations conducted to study the wake acceleration effect as summarized above, some common conclusions can be summarized here:

- A similar phenomenon is found in the numerical simulation. The drag force of the affected bubble is reduced as soon as it is immersed in the wake generated by the leading one.
- An equilibrium distance at which the total hydrodynamic force acting on each bubble is equal is found in the numerical simulation. The drag force reduced by the wake effect is balanced with the repel force caused by the higher pressure in the gap between two bubbles. This equilibrium distance greatly depends on Re_b and increases as Re_b increases.
- The discovery of equilibrium distance is in marked contrast to the experimental study in which bubbles have invariably been found to catch up with each other and collide.

Several authors discussed this discrepancy and concluded it as the effect from bubble deformation and interface contamination in the experiment.

2.5 Modeling approaches of the wake acceleration effect

In contrast to a single bubble, the existing modeling approaches of the wake acceleration effect are still limited to cases at low Re_b. Most of them are devoted to examine the hydrodynamic interactions of a pair of aligned spherical identical bubbles rising in line. This is mainly due to the fact that the clear physical mechanism of the wake acceleration effect is still not well understood. Attempts are also needed to investigate the velocity profile of unstable wake at high Re_b. As discussed by Fan and Tsuchiya [23], if Re_b is larger than the second critical Reynolds number (about 100-300), wakes show unsteady motions with a large-scale vorticity structure.

Disregarding the effect from bubble deformation, several correlations incorporating strong simplifications and assumptions are proposed to describe the wake acceleration effect under low Re_b condition. In general, all these models found in the open literature can be divided into two groups: analytic method and semi-analytic method. Here, the empirical correlations without considering the physical mechanism of the wake acceleration effect are not included in the following discussion.

1. **Analytic method: Modeling based on the vorticity distribution between bubbles**
   Based on the boundary layer approximation, Moore [50] proposed a drag force model by accounting for the viscous effect from the boundary layer around a single particle. Following this line of thought, the drag modification on both leading and affected bubbles are considered. Harper [27, 28] introduced several analytical approximations which incorporate the vorticity diffusion between bubbles and provided a correction to Moore's model.

2. **Semi-analytic method: Modeling based on defining a new proper reference velocity**
   The basic idea was firstly suggested by Yuan and Prosperetti [98] to define a new relative velocity reduced by the wake velocity. Later on, Ramírez-Muñoz et al. [64] proposed a method for evaluating the increased rising velocity of the affected bubble in the far wake region of the leading one at $Re_b \gg 1$. The additional upward velocity of the affected bubble was predicted by laminar boundary layer theory and averaged over the bubble-projected area.

Both approaches treat the wake as the origin of the drag modification, however different simplifications regarding the wake acceleration effect have been made.

2.5.1 Analytic methods

Considering the range of Re_b in which viscous drag is more prominent, the motion of a single bubble has been extensively studied. Using a global energy balance, Levich and Spalding [42] deduced the drag force of a single stress-free bubble from the dissipation induced by the potential flow. The corresponding drag coefficient is:

$$C_d = \frac{48}{\mathrm{Re_b}} \tag{2.9}$$

The study of Levich was extended by Moore [51] who considered the viscous effect from the boundary layer around a single sphere. Improved estimates for the drag coefficient were obtained by solving appropriate equations in the rotational flow regions. The correlation is written as:

$$C_d = \frac{48}{\mathrm{Re_b}}\left(1 - F\mathrm{Re_b}^{-0.5}\right) \tag{2.10}$$

where F is a constant 2.211 for a single sphere.

Moore's analysis shows that the flow in the boundary layer is described by a balance between convection along the streamlines of the primary potential flow and viscous diffusion across these streamlines of circulation density [20]. If considering an affected bubble, its surrounding vortex structure is modified by the wake generated by the leading one. Hence, it is straightforward to extend Moore's theory to study the modified vortex structure and propose an analytic expression to account for the wake acceleration effect.

The first noticeable work based on an extension of Moore's model was carried out by Harper [27] in which the wake vorticity diffusion between bubbles is neglected. However, a significant discrepancy was observed between Harper's model and the numerical results by Yuan and Prosperetti [98]. Later on, Harper [28] obtained a second analytic approximation which focused on the wake's vorticity diffusion and its effects on both bubbles. His second model obtained the major effect of viscosity in the wake between bubbles and removed the discrepancy with the results by Yuan. It also proved that the viscous diffusion in the wake between bubbles can only be ignored if Re_b was impossibly high. In this method, the vorticity distribution around both leading and affected bubbles was evaluated by the diffusion equation. And the boundary layer equation obtained by the dimensionless circulation density in the wake was readily deduced from the vorticity equation. Based on these ideas, a formation was derived to propose a viscous drag correction to the value of F. It is written as:

$$F = \int_{-1}^{1} f_2(x,0)\,\frac{9\mu_2^2 - 1}{8}\,d\mu_2 + \int_0^{\infty}\int_{-1}^{1}\left(\frac{\partial f_2}{\partial z}\right)^2 \frac{9\mu_2^2 - 5}{64}\,d\mu_2 dz \tag{2.11}$$

in which:

$$\begin{aligned} x_2 &= \frac{1}{4}(2+\mu_2)(1-\mu_2)^2; \quad \mu_2 = \cos\theta_2; \\ z &= \frac{3\mathrm{Re_b}^{-1/2}(r_1 - R)\sin\theta_1}{8R}; f_2 = -\left(\frac{8}{3}\right)\int_z^{\infty}\Omega_2(x_2, z)dz \end{aligned} \tag{2.12}$$

where subscripts 1 and 2 stand for the leading and affected bubble, respectively. r, θ are spherical polar coordinates centred on the bubble, respectively. R is the bubble radius and Ω_2 is the dimensionless circulation density around the affected bubble. In Eq. 2.11, all the integrations were done numerically with NAG Gaussian routines [55], with 32, 64 and 128 grid points in each direction to check the convergence. The idea of modeling is clear and it shows a good agreement with the numerical results provided by Yuan. But the calculations are not quite simple and its implementation to CFD codes can not be achieved easily.

As we can see from the above brief descriptions, the analytic approaches are mainly based on the Moore's correlation, with which several correlations are proposed to correct the drag factor F with consideration of viscous wake between bubbles. However, assumptions taken for the approximation are quite different. The second model of Harper provides a best prediction of drag force coefficient compared with DNS results and indicates that the viscous wake is responsible for the wake acceleration effect. Nevertheless, its application to simulation of bubbly flow is still doubtful due to the fact that Moore's model ceases to be valid under high Re_b condition.

2.5.2 Semi-analytic methods

To obtain a general theoretic expression for the wake acceleration effect, especially when the affected bubble is immersed in the wake with a highly non-uniform velocity profile, the first attempts was made by Marks [48] in which the rising velocity of a bubble in a chain was assumed to be equal to the wake velocity of bubble ahead of it plus its velocity relative to the wake. In the work of Toshiro et al. [89], the velocity of the liquid near the centerline of the wake was adopted as the wake velocity. Later on, Yuan and Prosperetti [98] extended this model and suggested a scheme to estimate the drag on the affected bubble by considering the same leading bubble drag coefficient but defining a new reference velocity reduced by the wake velocity. Following this line of thought, based on the known flow field and wake structure around a single bubble, Katz and Meneveau [34] proposed a model to predict the rising velocities of bubble pairs. This model further accounted for the effect from the repelling pressure gradient caused by the velocity gradient of liquid phase.

Among these models, it is of importance to determinate the value of wake velocity. If assuming that the wake is a laminar flow and neglecting the bubble deformation, laminar boundary layer theory can be employed to predict the vertical component of wake velocity which is greatly larger than the radial component. If considering a bubble rising freely in the stagnant water with terminal velocity V_T, a reference frame (r, s) whose origin is attached to the bubble center is introduced to provide an analytic expression of wake velocity. Following the work by Schlichting and Gersten [78], the wake velocity profile is evaluated as:

$$\frac{U_w}{V_T} = \frac{C_d d}{32 s} Re_b \exp\left(-\frac{r^2 Re_b}{4sd}\right) \tag{2.13}$$

where C_d denotes the drag force coefficient, r stands for the vertical distance to bubble centerline and s denotes the vertical distance to bubble center. Re_b is the bubble Reynolds number evaluated by bubble diameter d, V_T and the dynamic viscosity of liquid. The detailed derivation can be found in Appendix A.

As described by Katz and Meneveau [34], the potential flow solution evaluated at the centerline should also be included in the expression of wake velocity. Therefore, the total wake velocity can be approximately estimated by the sum of the potential flow solution evaluated around the bubble and the wake velocity profile caused by the boundary layer around the bubble, so that:

$$\frac{U_w}{V_T} = \frac{1}{8}\left(\frac{d}{s}\right)^3 + \frac{C_d d}{32 s} Re_b \exp\left(-\frac{r^2 Re_b}{4sd}\right) \tag{2.14}$$

The velocity profile of wake is not uniform and varies in the radial direction. In the literature, an radially averaged wake velocity experienced by the affected bubble $\overline{U_w}$ is introduced. It is calculated by integrating the wake velocity over the bubble-projected area. If neglecting the bubble deformation under low Re_b condition, the bubble cross-section is calculated by its bubble diameter. Therefore, $\overline{U_w}$ is calculated as:

$$\begin{aligned} \overline{U_w} &= \frac{4}{\pi d^2} \int_0^{d/2} U_w 2\pi r dr \\ &= \frac{1}{8}\left(\frac{d}{s}\right)^3 V_T + \frac{C_d V_T}{2}\left(1 - \exp\left(-\frac{\mathrm{Re}_b d}{16 s}\right)\right) \end{aligned} \tag{2.15}$$

With Eq. 2.15, Katz and Meneveau [34] assumed that the affected bubble has an additional upward velocity given by the radially averaged wake velocity over its cross-section $\overline{U_w}$. Hence,

the increased rising velocity of the affected bubble is written as follows:

$$V_{T,2}^{*} = \frac{1}{\Gamma\left(\mathrm{Re}_{b,2}\right)} + \frac{4\Gamma\left(\mathrm{Re}_{b,1}\right)}{\mathrm{Re}_t}\left[1 - \exp\left(-\frac{\mathrm{Re}_{b,1}}{4L^{*}}\right)\right] + V_{T,1}^{*}L^{*-3} - \frac{\mathrm{Re}_t}{\Gamma\left(\mathrm{Re}_{b,2}\right)}V_{T,1}^{*2}L^{*-4} + V_{T,1}^{*}\left(2L_0^{*} - L^{*}\right)^{-3} + \frac{\mathrm{Re}_t}{\Gamma\left(\mathrm{Re}_{b,2}\right)}V_{T,1}^{*2}\left(2L_0^{*} - L^{*}\right)^{-4} \tag{2.16}$$

Here:

$$V_T^{*} = \frac{V_T}{\left(R^2 g/3\nu\right)}, \quad L^{*} = \frac{L}{R}, \quad \mathrm{Re}_t = \frac{R^3 g}{3\nu^2} \tag{2.17}$$

where L_0^{*} is the initial vertical distance between bubbles normalized by R, ν is the dynamic viscosity of liquid and $\Gamma(Re_b)$ is a interpolation function to estimate the drag force coefficient of an isolated bubble. The terms decaying like L^{*-4} are due to the repelling pressure gradient. The second term in Eq. 2.16 is due to the upward wake velocity in the wake of the leading bubble and the terms involving $\left(2L_0^{*} - L^{*}\right)$ arise from the bubbles in the neighboring cells. By comparing the second and fourth terms in the rhs of Eq. 2.16, it is evident that the repulsion induced by pressure gradients exceeds the contribution of the wake velocity when $L^{*} < \sqrt{Re_b}$. However, repulsion by pressure is possible only at distances which are shorter than the validity limit of this model, for the reason that the assumed wake structure becomes valid only above a distance of the order $\sqrt{Re_b}$. This model has a qualitative agreement with Harper [27].

The balance equations of the forces acting on a spherical bubble rising in a chain were also considered by Zhang and Fan [101]. Mathematical models for the rising velocity of the affected bubble were derived. Zhang and Fan [100] firstly developed a semi-analytical expression for the drag force ratio of an interactive sphere. Later on, this model was extended to the bubble case and utilized in the model formulation. The virtual mass and basset forces acting on a bubble are also taken into account in the modeling. The total force acting on the bubble consists of five parts as shown in Eq. 2.18:

$$\frac{1}{6}\pi d^3 \rho_l \frac{dU_b}{dt} = F_g + F_d + F_p + F_{vm} + F_B \tag{2.18}$$

where U_b is the simultaneous velocity of the concerned bubble. The terms on the right-hand side denote the buoyancy, drag, pressure gradient, virtual mass and Basset forces in sequence. To model the reduced drag force, a new relative velocity between the bubble and stagnant fluid is defined as the subtraction of the radially averaged wake velocity over its exposed frontal area $\overline{U_w}$ from the rising velocity of the affected bubble. The reduced drag force acting on the affected bubble $F_{d,2}$ was evaluated by the new relative velocity as shown in Eq. 2.20:

$$F_{d,2} = C_{d,2}\frac{\pi}{8}\rho_l d^2\left(\overline{U_w} - V_{T,2}\right)^2 \tag{2.19}$$

In Eq. 2.20, the drag force coefficient $C_{d,2}$ was still undetermined. The ratio of the drag coefficients, $C_{d,2}/C_{d,1}$, was further assumed to be equal to the ratio of the bubble Reynolds number of a single bubble to the bubble Reynolds number based on $\overline{U_w} - V_{T,2}$. At last, a simple model of the reduced drag force is given as:

$$\frac{F_{d,2}}{F_{d,1}} = \frac{\overline{U_w} - V_{T,2}}{-V_{T,1}} \tag{2.20}$$

With definitions of forces existed in Eq. 2.18, the finite difference method was utilized to numerically solve the balance equation of bubble motion. The first order difference scheme was adopted to discretized the time term in the governing equation. The method was validated

when Re_b ranged from 3 to 35 and showed that the general trend of the rising velocity of the affected bubble can be predicted.

In the work discussed above, the relative velocity of the affected bubble is directly reduced by the averaged wake velocity over the bubble-projected area, named $\overline{U_w}$. This area is usually assumed to be equal to the bubble cross-section. Ramírez-Muñoz et al. [65] presented a question that whether one can always assume $\overline{U_w}$ as the reference fluid velocity, irrespective of the vertical distance between bubbles and Re_b values. They proposed a more appropriate reference fluid velocity when the flow structure was highly non-uniform in the radial direction and larger than the affected bubble's radius. It is written as:

$$F_{d,2} = C_{d,2}\frac{\pi}{8}\rho_l d^2\left(\gamma\overline{U_w} - V_{T,2}\right)^2 \tag{2.21}$$

where unknow parameter γ depends on L/d, Re_b and the bubbles dimensionless radius R_γ/R. R_γ is the maximum radius where the wake velocity is significant in the whole breadth wake. Nevertheless, in order to obtain a simple explicit expression for the drag force of an affected bubble, they proposed an algebraic equation for $\gamma(Re_b)$ as Eq. 2.22 in which the dependence on L/d and R_γ/R was omitted.

$$\gamma\,(\mathrm{Re}) = 1 - 0.7398\exp\left(-0.0123\mathrm{Re_b}\right) \tag{2.22}$$

Later on, Ramírez-Muñoz et al. [64] introduced a simple expression for the drag force of an affected bubble by following this methodology. However, in this approach it was unnecessary to introduce the additional parameter γ to obtain the proper reference fluid velocity, shown as follows:

$$\frac{\overline{U_w}}{V_T} = \frac{1}{8}\left(\frac{d}{l}\right)^3 + \frac{C_d}{2}\left(\frac{1}{R_\gamma/R}\right)^2\left[1 - \exp\left(-\frac{\mathrm{Re}_1}{16}\frac{d}{l}\left(\frac{R_\gamma}{R}\right)^2\right)\right] \tag{2.23}$$

By incorporating a normalized form of the wake velocity predicted by laminar boundary layer theory together with Moore [50], an analytic equation for R_γ/R is obtained as follows:

$$\frac{R_\gamma}{R} = \sqrt{u\left(\frac{16}{\mathrm{Re}_1}\frac{L}{d} + \frac{8}{\mathrm{Re}_1^{1/2}}\right)} \tag{2.24}$$

In Eq. 2.24, u is dependent on the ratio of the normalized form of the wake velocity from the centerline up to R_γ to the total wake velocity. Theoretically, its value could take any value from zero to infinity. However, a standard least-square minimization procedure is used to optimize its value. It is found that $u = 1.11$ is the optimal value.

To sum up, semi-analytic models are widely used to analysis the wake acceleration effect when Re_b covers a wide range of prospective. Their implements into CFD codes are quite simple. However, several noticeable drawbacks should be mentioned.

1. Despite of the definition of the averaged wake velocity experienced by the affected bubble, a coefficient is introduced to adjust the contribution from the averaged wake velocity $\overline{U_w}$. It is found that an overestimation of the wake acceleration effect is widely reported if its value is taken as unity. Until now, no agreement is reached to determine its value. Generally, its value is taken based on an optimized analysis of experimental data. It is rather questionable to use these optimal values for cases which are beyond the scope of experiments.

2. In the existing models, the influence from bubble deformation is not taken into account. However, deformed bubbles are usually encountered in the industrial processes. In

order to improve the prediction accuracy of the wake acceleration effect, it should be included in the further modeling.

3. Modeling of the wake acceleration effect

In this chapter, a drag force model which considers the wake acceleration effect is proposed. Key constitutive relation of the proposed drag force model is to model the relationship between the increased bubble rising velocity and the wake velocity. To clarify the target of this study, phenomenological description and basic assumptions employed in the current study are briefly discussed in the first section. Secondly, the wake velocity profile is estimated under both low and high Re_b conditions. The velocity distribution around a single bubble is also obtained based on the potential flow theory. The results are then combined to compute the increased rising velocity of the affected bubble. Finally, in order to close the modeling for the cases under high Re_b condition, correlations are proposed to estimate the wake velocity profile of unstable wake based on a systematic simulation covering a wide range of bubble diameter.

3.1 Phenomenological description and basic assumptions

Phenomenological description

In the current study, the primary purpose is to propose a drag force model which considers the wake acceleration effect and its application to RANS simulation of bubbly flow. For a good correlation of drag force coefficient, several requirements should be satisfied: firstly, it should comply with actual physics and can really describe physical phenomena under different operating environments; secondly, the drag coefficient expression should be a formula as simple and general as possible; thirdly, factors influencing the drag coefficient should be taken into account as comprehensively as possible. To identity promising directions for improvements, it is necessary to take a look at the exising models. As discussed before, the existing model can be divided into two groups: analytic approach and semi-analytic approach. The analytic approach is derived based on a correction to Moore's model and limited to low Re_b cases. For the semi-analytic approach, based on the concept of defining a proper reference velocity, the relationship among the increased bubble rising velocity, the wake velocity and the terminal velocity of a single bubble is modeled. Since the terminal velocity of a single bubble can be predicted by a vast of drag force models, the semi-analytic method has potential to provide a general drag force model when Re_b and Eo numbers vary over a wide range. For this reason, the main target of the current study will focus on modeling the key constitutive relation between the increased bubble rising velocity and the wake velocity. And the influence from bubble deformation and unstable wake which are quite common in the industrial processes will be also considered in the analysis. With the obtained rising velocity of the affected bubble, the corresponding drag force coefficient is estimated based on the balance between the drag force and the buoyancy force , as shown in:

$$C_d = \frac{4\left(\rho_l - \rho_g\right) gd}{3\rho_l V_T^2} \tag{3.1}$$

In the preliminary work of Yuan, a new relative velocity reduced by the wake effect was suggested, while the drag force of the affected bubble was evaluated by considering the same leading bubble drag coefficient. This yields a new reference fluid velocity u_{ref} which depends on bubble terminal velocity V_T as:

$$u_{ref} = V_T - u_w \tag{3.2}$$

where u_w is a velocity related to the wake velocity. Following this line of thought, Katz and Meneveau [34] proposed a method for evaluating the increased rising velocity of the affected bubble in the far wake region. u_w is predicted by laminar boundary layer theory and radially averaged over the bubble-projected area $\overline{U_w}$. Later on, a factor γ which is smaller than unity is introduced by Ramírez-Muñoz et al. [65] to adjust the contribution from $\overline{U_w}$ as:

$$u_{ref} = V_T - \gamma U_w \tag{3.3}$$

From Eq. 3.3, it is seen that factor γ adjusts the contribution from the averaged wake velocity $\overline{U_w}$. However, a physical description of γ is not yet well clarified. Its value is usually taken based on an optimized analysis of experimental data obtained at low Re_b, and it is still doubtable to use the optimal value in the prediction of cases which are beyond the scope of the employed experiments. Hence, it is quite necessary to determinate its value in a more general way. On the other hand, the separation of boundary layer is observed under high Re_b condition as well as an unstable wake. This phenomenon leads to a greater complexity of vortex structure in the wake. Consequently, the achievement of predicting the velocity profile of unstable wake is still quite limited. In addition, the influence from bubble deformation is also not considered.

All these mentioned drawbacks reveal that, to improve the prediction accuracy of the wake acceleration effect, especially when deformed bubbles and unstable wakes are encountered, the existing drag force models need further improvements. Improvement of drag force model should be performed in two aspects. Firstly, influence from bubble deformation and unstable wake should be considered. Secondly, physical meanings of the factors employed in the proposed model should be clear. This, of course, requires us to have intimate knowledge about the physical mechanism which describes the relationship between the bubble rising velocity and the liquid field around the affected bubble.

To sum up, our study focuses on modeling the relationship between the increased bubble rising velocity and the wake velocity. In the proposed model, the factor γ will be introduced in a more general way to account for the influence from bubble deformation. In addition, the velocity profile of unstable wake needs to be specified under high Re_b condition. With description of the relevant physical mechanism which captures the modification of velocity field around the affected bubble, the proposed model is capable to predict the wake acceleration effect in a wide range of Re_b and Eo.

Basic assumptions

In this context, two bubbles with the same equivalent diameter and shape are considered. The shapes of them are expressed as an oblate spheroid which is a rotationally symmetric ellipsoid and can be formed by rotating an ellipse about its minor axis. As illustrated in Fig. 3.1, a single bubble rising freely in the stagnant water is schematically shown in the left figure. Its terminal velocity $V_{T,1}$ can be predicted by a vast of drag force models and most of them have a good performance. The right one is continuously affected by the wake. For convenience, it is shortened as the affected bubble in the follows. The non-uniform wake velocity around this bubble is denoted by U_w and CFD codes will be employed to examine its profile later. When the affected bubble reaches its steady state, its terminal velocity is assumed to be $V_{T,2}$.

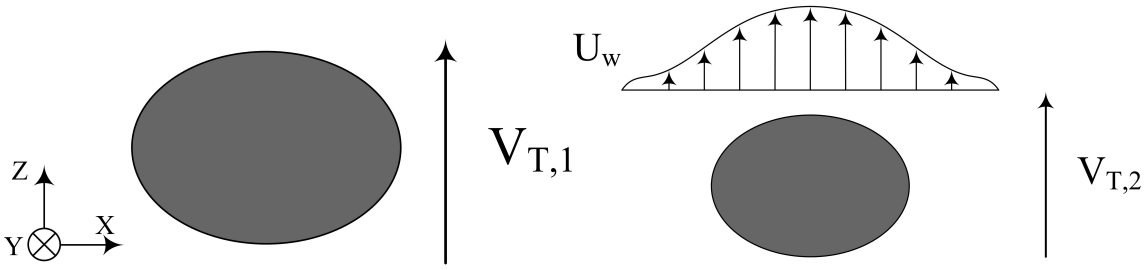

(a) Single bubble **(b)** Bubble affected by the wake

Fig. 3.1: Two equal-sized bubbles considered in the analysis. Z direction stands for the rising direction.

Following the line of thought proposed by Katz, the known structure of wake around the affected bubble is used to consider how the affected bubble moves within this flow field. In order to incorporate the influence from bubble deformation, the velocity field around the affected bubble is investigated in a more general way. In the current study, the following assumptions are taken.

1. **The acceleration effect on the bubble motion is only governed by the non-uniform wake flow.**
   A justification for this assumption is provided by a vast of experimental and numerical studies, such as Yuan and Prosperetti [98] and Stewart [85]. It is shown that the affected bubble shows a sudden acceleration as soon as the wake reaches it. Hence, the wake effect is treated as the driving mechanism which accelerates the motion of the affected bubble.

2. **The wake effect on the bubble motion is one-way.**
   This approximation is made thorough so that the existence of the affected bubble has no influence on the wake velocity profile around it. The difference between $V_{T,2}$ and $V_{T,1}$ is then modeled based on the wake velocity profile obtained from a single bubble. This simplification can be extended to the wake much closer to the leading bubble, i.e. for dimensionless distance $L/d > O(3/2)$ when Re_b is in the order of 100 or more [28] and is widely employed in the previous studies of the wake acceleration effect such as: Zhang and Fan [101] and Ramírez-Muñoz et al. [64].

3. **The time-dependent effect is neglected in the analysis.**
   As mentioned above, the steady state of the affected bubble is considered, and it is reasonable to neglect the time-dependent effect. Consequently, the increased rising velocity $V_{T,2}$ depends only on the wake velocity, and not on its time history. This assumption is consistent with the experimental observation conducted by Katz and Meneveau [34].

4. **The shape of the affected bubble is the same as the isolated one.**
   Although in the experimental of Serizawa and Kataoka [79], the distortion of the bubble surface was observed. Especially when liquid velocity is high, the bubble is very distorted due to the collisions of turbulent eddies in the liquid. For this neglecting, following reasons are considered: firstly, the consideration of bubble distortion may produce unexpected difficulties into the modeling of the wake effect; secondly until now no experimental study is conducted to describe the bubble distortion caused by the turbulence quantitatively; thirdly the proposed model aims at predicting the increased bubble rising velocity under steady state and the instant effect from the turbulent eddies may be neglected.

Following these four assumptions, key constitutive relation between the increased rising velocity and the wake velocity will be proposed in a more general way and the influence from bubble deformation will be also included in the new drag force model. In the following work, the wake will be assumed to be laminar for small bubbles, and turbulent for the larger bubbles. In chapter 3.2, we estimate the wake velocity profile under both low and high Re_b conditions. In chapter 3.3, the velocity distribution around a single bubble is obtained based on the potential flow theory. The results are then combined to compute the increased rising velocity of the affected bubble in chapter 3.4. Finally, in chapter 3.5 attempts are made to estimate the wake velocity profile under high Re_b condition based on the CFD simulation which covers a wide range of bubble diameter.

3.2 Velocity profile in the wake

3.2.1 Low bubble Reynolds number case

When Re_b is low, the wake generated by the relative motions between bubble and liquid phase is assumed to be a laminar flow. To simplify the problem, two-dimension analysis is carried out to investigate the flow structure of wake around the considered bubble. As discussed in the boundary layer calculations by Schlichting and Gersten [78], the radial component of wake velocity is greatly smaller than its vertical component and the wake flow is nearly parallel. If a spherical bubble is immersed in the wake, wake velocity U_w around the this bubble can be decomposed into the tangential part and the normal part. With definitions of the unit vector along the gravity direction $\mathbf{e}_z$ and unit tangential vector to the bubble interface $\mathbf{t}$, the tangential component of wake velocity at bubble interface is computed as follows:

$$U_w \mathbf{e}_z \cdot \mathbf{t} \tag{3.4}$$

This correlation will be used to correct the velocity distribution around the affected bubble. It should be noted that Eq. 3.4 is a general expression of calculating the tangential contribution of wake velocity. It is also valid for a deformed bubble if the value of $\mathbf{e}_z \cdot \mathbf{t}$ is known.

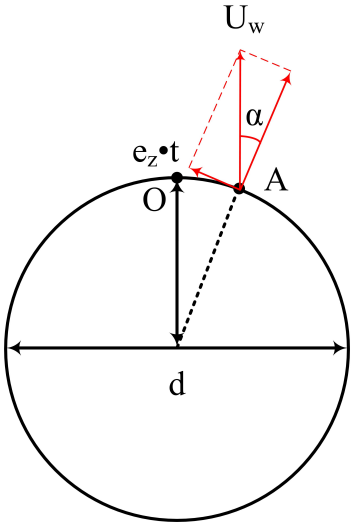

Fig. 3.2: Decomposition of the wake velocity

As discussed in chapter 2.5.2, the radially averaged wake velocity $\overline{U_w}$ is calculated as:

$$\begin{aligned}\overline{U_w} &= \frac{4}{\pi d^2}\int_0^{d/2} U_w 2\pi r dr \\ &= \frac{1}{8}\left(\frac{d}{s}\right)^3 V_T + \frac{C_d V_T}{2}\left(1-\exp\left(-\frac{\mathrm{Re}_b d}{16s}\right)\right)\end{aligned} \tag{3.5}$$

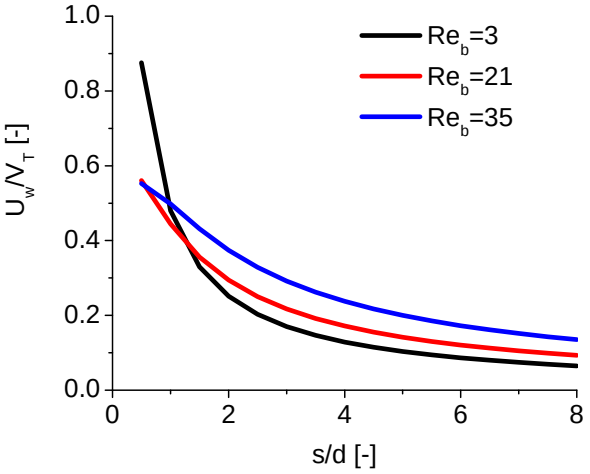

Fig. 3.3: Dependency of the averaged wake velocity $\overline{U_w}$ on the vertical distance to the bubble center when Re_b varies from 3 to 35

For simplicity, Eq. 3.5 is reduced to:

$$\overline{U_w} = V_T F(s, d, \mathrm{Re}_b, C_d) \tag{3.6}$$

where:

$$F(s, d, \mathrm{Re}_b, C_d) = \frac{1}{8}\left(\frac{d}{s}\right)^3 + \frac{C_d}{2}\left(1-\exp\left(-\frac{\mathrm{Re}_b d}{16s}\right)\right) \tag{3.7}$$

The dependency of averaged wake velocity $\overline{U_w}$ on the vertical distance to the bubble center s is schematically shown in Fig. 3.3 at Re_b of 3, 21 and 35. $x-$ and $y-$ axes are normalized by bubble diameter d and bubble terminal velocity V_T, respectively. It is seen that $\overline{U_w}$ is dependent on both s and Re_b. The effect from Re_b on $\overline{U_w}$ is very clear. When s/d is larger than 2, $\overline{U_w}$ increases as Re_b increases.

3.2.2 High bubble Reynolds number case

As bubble diameter increases, an oblate bubble is expected while wake structures become unstable. Difficulties arise at the unstable boundary layer around the bubble where the separation of boundary layer happens. A periodic vortex shedding, which leads to a greater complexity of the vortex structure, is also observed underneath the bubble. All these features make laminar boundary layer theory to be invalid at high Re_b. Hence, it is almost infeasible to propose an accurate description of unstable wake with the analytic method. Until now, the achievement of predicting the velocity profile of unstable wake is still limited.

In the current study, turbulent boundary layer theory is employed to provide an expression of wake velocity profile at high Re_b. In this expression, an unknown parameter named turbulent viscosity ν_t is introduced to describe the turbulent structure in the wake. Given the

complexity of the phenomena, a simplified model which contains most of the relevant physical description of the wake structure is still adopted as long as it captures the global physics in the wake. Later on, CFD simulation will be carried out to propose a correlation of the unknown turbulent viscosity.

As shown in Fig. 3.4, the aspect ratio of a deformed bubble E is equal to b/a. Here, b and a are the minor and major axes, respectively. Usually, the size of a deformed bubble is denoted by the equivalent diameter d. The dependency of equivalent bubble diameter on aspect ratio and major axis is written as follows:

$$d = 2aE^{1/3} \tag{3.8}$$

Following the calculations by Schlichting and Gersten [78] and Tennekes and Lumley [86], the velocity profile of unstable wake, which is generated by a deformed bubble, is calculated as follows:

$$U_w = V_T \frac{C_d a}{16 s} \frac{V_T 2a}{\nu_{eff}} \exp\left(-\frac{r^2 V_T}{4 s \nu_{eff}}\right) \tag{3.9}$$

where ν_{eff} is the effective viscosity which can be decomposed into two parts: the laminar viscosity ν and the turbulent viscosity ν_t.

For an oblate bubble, the value of its cross-section is equal to πa^2. Hence, the averaged wake velocity experienced by an oblate bubble is calculated as:

$$\begin{aligned} \overline{U_w} &= \frac{1}{\pi a^2} \int_0^a U_w 2\pi r dr \\ &= \frac{C_d V_T}{2} \left(1 - \exp\left(-\frac{a^2 V_T}{4 s \nu_{eff}}\right)\right) \end{aligned} \tag{3.10}$$

For simplicity, Eq. 3.10 is reduced to:

$$\overline{U_w} = V_T H(V_T, C_d, a, s, \nu_{eff}) \tag{3.11}$$

where:

$$H(V_T, C_d, a, s, \nu_{eff}) = \frac{C_d}{2} \left(1 - \exp\left(-\frac{a^2 V_T}{4 s \nu_{eff}}\right)\right) \tag{3.12}$$

In Eq. 3.9, the determination of ν_{eff} is still an open question. In chapter 3.5, this problem will be solved using CFD approach .

3.3 Velocity distribution around bubble

In this section, the velocity distribution around a single bubble will be investigated theoretically. The tangential component of liquid velocity $u_{L,A}$ will be estimated at bubble upper interface. Its expression will be provided based on the velocity potential Φ for an axis-symmetric potential flow about an oblate bubble moving with terminal velocity V_T in the stagnant liquid. This method was developed by Lamb [39] and used by Tomiyama et al. [88]. For the sake of discussion and completeness, the detailed derivation of the analytical solution for a potential flow aoubt a moving oblate spheroid with aspect ratio E and terminal velocity V_T is briefly reviewed in Appendix C

As shown in Fig. 3.4, the oblate spheroidal coordinates (θ, ϕ, ξ) which are a three dimensional orthogonal coordinate system are adopted to express the surface coordinates of an oblate spheroid. For a certain point A at the interface of an oblate bubble, an expression will

be given to calculate its tangential velocity $u_{L,A}$. This expression can be also employed to provide the solution of a spherical bubble if taking the limit $E \to 1$. The coordinates of a certain point at the bubble surface is written as follows:

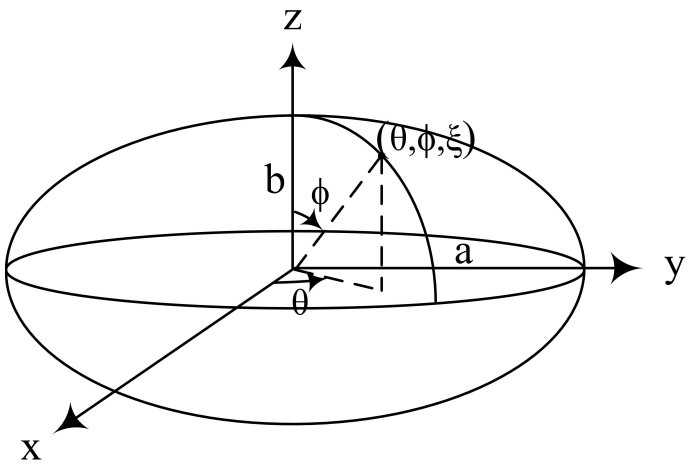

Fig. 3.4: Surface coordinates of an oblate bubble

$$\begin{aligned} x &= k\sqrt{1+\xi^2}\sin\phi\cos\theta = k\sqrt{1+\xi^2}\sqrt{1-m^2}\cos\theta \\ y &= k\sqrt{1+\xi^2}\sin\phi\sin\theta = k\sqrt{1+\xi^2}\sqrt{1-m^2}\sin\theta \\ z &= k\xi\cos\phi = k\xi m \end{aligned} \tag{3.13}$$

where (x,y,z) are Cartesian coordinates and m is short for $\cos\phi$.

It should be noted that k and ξ constitute a surface of spheroid. For an oblate bubble of concern whose minor axis and major axis are b and a, the value of them can be estimated as follows:

$$\begin{aligned} \xi_0 &= \frac{b}{\sqrt{a^2-b^2}} \\ k_0 &= \sqrt{a^2-b^2} \end{aligned} \tag{3.14}$$

Hence, the aspect ratio of this bubble is $E = \xi_0/\sqrt{1+\xi_0^2}$.

Following Lamb's work, the coordinates of a certain point at the bubble interface can be expressed by an oblate spheroidal coordinates. Consequently, the dot product of $\mathbf{t}$ and $\mathbf{e}_z$ at point A can be calculated by its coordinates. As shown in Fig. 3.2, if α is introduced to denote the angle between the unit normal vector of bubble interface $\mathbf{n}$ and $\mathbf{e}_z$, the value of $\mathbf{e}_z \cdot \mathbf{t}$ is calculated as follows:

$$\mathbf{e}_z \cdot \mathbf{t} = \sin\alpha = \xi_0\sqrt{\frac{1-m^2}{\xi_0^2+m^2}} \tag{3.15}$$

where ξ_0 and m are calculated as follows:

$$m = \cos\phi_A; \quad \xi_0 = \frac{E}{\sqrt{1-E^2}} \tag{3.16}$$

Following the work done by Tomiyama et al. [88], the distribution of $u_{L,A}$ is calculated as follows:

$$u_{L,A} = V_T\sqrt{\frac{\left(1-E^2\right)\sin^2\phi_A}{\cos^2\phi_A + E^2\sin^2\phi_A}}\,\frac{1-E^2}{\sin^{-1}\sqrt{1-E^2} - E\sqrt{1-E^2}} \tag{3.17}$$

$u_{L,A}$ is schematically shown in Fig. 3.5. It is illustrated that the tangential velocity points downwards due to the moving reference. At the point O which is called the stagnant point, the tangential velocity vanishes.

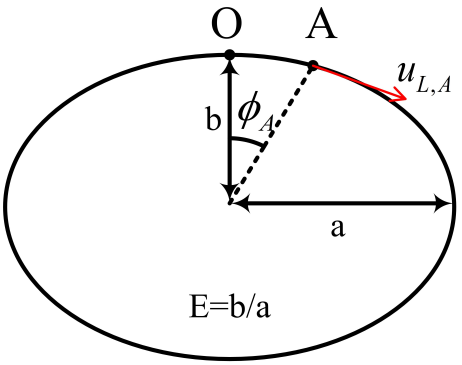

Fig. 3.5: Tangential velocity at interface of a single bubble

3.4 Model equations for rising velocity

With the expressions provided in chapter 3.2 and chapter 3.3, attempts will be made to describe the relationship between the increased rising velocity $V_{T,2}$ and the wake velocity U_w. Recalling the additive correction provided by Katz and Meneveau [34], the affected bubble is assumed to have an additional upward velocity given by the radially averaged wake velocity over its cross-section $\overline{U_w}$. However, this method is equivalent to assume that the affected bubble is rising freely in the moving water with an uniform velocity $\overline{U_w}$. It conflicts with the fact that the wake velocity exhibits a non-uniform profile in the radial direction and only exists in a small region underneath the rising bubble. Therefore, an overestimation of the increased rising velocity is widely reported in the literature when using this approach. In the current study, the tangential component of wake velocity is employed to correct the velocity distribution around the upper interface of an affected bubble. Hence, the influence from bubble deformation is naturally included in the modeling.

To advance the work by Katz and Meneveau [34], the absolute tangential velocity around an affected bubble is assumed to be the sum of the tangential velocity caused by its relative motion and the contribution from the wake velocity. Consequently, the same tangential velocity distribution as that of a single bubble is obtained as follows:

$$u_{L,A,2} - U_w \mathbf{e}_z \cdot \mathbf{t} = u_{L,A,1} \tag{3.18}$$

The tangential velocities $u_{L,A,1}$ and $u_{L,A,2}$ are evaluated by Eq. 3.17 and the tangential component of wake velocity is calculated by Eq. 3.4 and Eq. 3.15. Substituting these expressions into Eq. 3.18 yields the following equation:

$$f(E)\,\sqrt{1-E^2}\,V_{T,2} - E\,U_w = f(E)\,\sqrt{1-E^2}\,V_{T,1} \tag{3.19}$$

where:

$$f(E) = \frac{1-E^2}{\sin^{-1}\sqrt{1-E^2} - E\,\sqrt{1-E^2}} \tag{3.20}$$

The terms depending on ϕ_A are eliminated from both sides of Eq. 3.18. To account for the non-uniform profile of wake velocity in the radial direction, it is more appropriate to employ

the radially averaged wake velocity $\overline{U_w}$ to consider the influence of wake, instead of the wake velocity U_w. Hence, Eq. 3.19 is rewritten as:

$$f(E)\sqrt{1-E^2}V_{T,2} - E\overline{U_w} = f(E)\sqrt{1-E^2}V_{T,1} \tag{3.21}$$

As discussed before, the expression of $\overline{U_w}$ can be divided into two groups: low Re_b case and high Re_b case. Bubble deformation is usually neglected under low Re_b condition. And it is easy to prove that the value of $\frac{E}{f(E)\sqrt{1-E^2}}$ approaches 0.67 by taking the limit $E \to 1$. Substituting the expression of wake velocity profile at low Re_b and assuming that the wake is generated by a bubble with terminal velocity $V_{T,2}$, the following equation is obtained:

$$V_{T,2} = \frac{1.5}{1.5 - F\left(s, d, \mathrm{Re}_{b,2}, C_{d,2}\right)} V_{T,1} = \chi_1\left(s, d, \mathrm{Re}_{b,2}, C_{d,2}\right) V_{T,1} \tag{3.22}$$

Eq. 3.22 indicates the dependency of the increased rising velocity $V_{T,2}$ on the averaged wake velocity $\overline{U_w}$ and the terminal velocity of a single bubble $V_{T,1}$. As the vertical distance to the bubble center s increases further, the multiplicative factor χ_1 approaches 1 and the rising velocity of the affected bubble must evidently tend asymptotically to the single bubble value $V_{T,1}$.

Analogously, the following equation is obtained for cases at high Re_b:

$$V_{T,2} = \frac{f(E)\sqrt{1-E^2}}{f(E)\sqrt{1-E^2} - EH\left(V_{T,2}, C_{d,2}, a, s, \nu_{eff}\right)} V_{T,1} = \chi_2\left(V_{T,2}, C_{d,2}, a, x, \nu_{eff}, E\right) V_{T,1} \tag{3.23}$$

Eq. 3.23 clearly indicates that, at high Re_b, the increased bubble rising velocity $V_{T,2}$ is also dependent on the bubble aspect ratio E. As shown in Fig. 3.6, the effect from E on the velocity ratio is very clear. The velocity ratio $V_{T,2}/V_{T,1}$ decreases as E decreases.

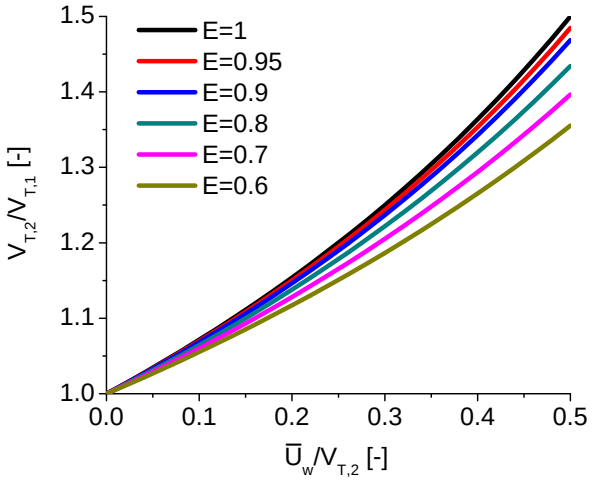

Fig. 3.6: Dependence of the velocity ratio $V_{T,2}/V_{T,1}$ on the averaged wake velocity $\overline{U_w}$ and the bubble aspect ratio E

With Eq. 3.22 and Eq. 3.23, the increased rising velocity of the affected bubble are predicted under both low and high Re_b conditions. The influence from bubble deformation is included in the modeling. The relations presented herein contain most of the relevant physical description of the velocity distribution around the affected bubble which is modified by its surrounding wake. Given the complexity of the phenomena, a simple model is proposed as long

as it captures the global physics. There is no necessary to optimize the employed constants in the proposed model, since the uses of the constants for an oblate or spherical bubble are obtained with the derivations proposed by Lamb [39]. However, it can be found that $\overline{U_w}$ is the only known parameter in Eq. 3.21. This parameter will be carefully examined in the next section using CFD approach.

3.5 Simulation and analysis of the wake velocity profile under high bubble Reynolds number condition

In order to determinate the required wake velocity in the proposed drag force model, CFD approach is used to provide detailed information about the velocity profile of unstable wake which is generated by a single bubble rising in the stagnant water. The methodology of the interface-capturing with LES model will be briefly summarized at first. Secondly, the employed CFD approach will be validated against the experimental and numerical results found in the literature. It demonstrates the capability of the employed approach to predict the wake properties at high Re_b. Subsequently, based on a close examination of the wake velocity profile, correlations will be proposed to provide an estimation of the velocity profile of unstable wake in terms of bubble diameter and bubble terminal velocity. Finally, the proposed drag force model which includes correlations for the increased bubble rising velocity and the wake velocity profile are summarized and compared with the existing models.

3.5.1 Description of interface-capture methodology and turbulence modeling

The following section presents a brief description of interface-capturing methodology, here VOF method is employed, with the large eddy simulation (LES) to predict the turbulent properties in the flow field. VOF method is applicable to simulate the movements of interface between different fluids. To achieve good prediction accuracy, a desired mesh resolution is needed to predict the small-scale interactions between two phases. Besides, LES model which resolves large scales of the flow field solution allowing a better accuracy than RANS method also requires a high computational cost for simulation. With these two methods, a large diameter bubble rising freely in the stagnant water is simulated, with which the velocity profile of unstable wake is closely examined.

Interface-capturing methodology

To capture the interface movements between two immiscible, incompressible fluids, VOF method is developed to simulate the simultaneous flow with consideration of the surface tension force. In this section, the mathematical representation of VOF method is presented, but the heat and mass transfer is neglected in the modeling. Due to the existence of the interface, the material properties and the flow field are discontinuous across the interface between two fluids in the whole flow field. Nevertheless, beside the difference of the material properties between the two sides of interface, the surface tension force acting at the interface is also taken into consideration in a single-field formulation.

To mark the different fluids, the indicator function γ is defined to indicate the volume fraction of a fluid in a certain cell and shown in Eq. 3.24, from Rusche [67]. This parameter is employed by VOF method to capture the interface movements. In the transition region where the value of γ is between 0 and 1, the fluid is treated as a mixture of the two fluids on each side of the interface. In reality, this transition region is a discontinuous step, but here the interface is not

defined as a sharp boundary any more.

$$\gamma = \begin{cases} 1 & \textit{for a point inside fluid a} \\ 0 < \gamma < 1 & \textit{for a point in the transitional region} \\ 0 & \textit{for a point inside fluid b} \end{cases} \tag{3.24}$$

The indicator function γ is associated with each fluid and hence propagated with them as a Lagrangian invariant [29]. Therefore, it obeys a transport equation of the following form:

$$\frac{\partial \gamma}{\partial t} + (\mathbf{V} \cdot \nabla)\, \gamma = 0 \tag{3.25}$$

where $\mathbf{V}$ denotes the velocity field.

It should be noted that, Eq. 3.25 is only valid when γ is kept up as a step function throughout the whole simulation domain. For example, numerical diffusion in the interface region is not allowed as discussed in Rusche [67]. In reality, this constraint cannot be obeyed in VOF method in which the surface is not defined as a sharp boundary. The strict, simultaneous assertion of both, conservation of volume and surface constraints, can only be achieved in some moving mesh methods. Furthermore, the upper boundedness $\gamma \leq 1$ for Eq. 3.25 is not guaranteed because this formulation is not conservative.

To introduce a necessary compression of the interface, Weller [67] proposed an extra, artificial compression term in the indicator function equation, as shown below:

$$\frac{\partial \gamma}{\partial t} + \nabla \cdot (\mathbf{V}\gamma) + \nabla \cdot (\mathbf{V}_r \gamma\, (1 - \gamma)) = 0 \tag{3.26}$$

where $\mathbf{V}_r$ is a velocity filed suitable to compress the interface, and usually the velocity difference between two fluids is chosen. The artificial term is only active in the thin interface region because of the multiplication term $\gamma(1 - \gamma)$. Therefore, it does not affect the solution significantly outside the transition region and limits the smearing of the interface because of the compensation of the diffusive fluxes.

By default, a relative velocity $\mathbf{V}_r$ cannot be determined in VOF method because only a single velocity $\mathbf{V}$ for both fluids is considered in the whole domain. Thus, $\mathbf{V}_r$ has to be approximated as given in Eq. 3.26. The face flux velocity in the transition region $(\mathbf{V}_r)_f$ is then evaluated by:

$$(\mathbf{V}_r)_f = \min \left(c_\gamma \cdot \left| \frac{\phi_r}{|\vec{S}|} \right|, \left| \frac{\phi_r}{|\vec{S}|} \right|_{\max} \right) \tag{3.27}$$

which is bounded to the maximum face flux velocity $\left| \frac{\phi_r}{|\vec{S}|} \right|_{\max}$ in the flow field. Here, $\phi_r = \mathbf{V}_r \cdot \vec{S}$ represents the volumetric flux through the cell face $\vec{S}$ of $\mathbf{V}_r$, The subscript f denotes face value. The coefficient c_γ controls the weight of the compression velocity $(\mathbf{V}_r)_f$ and should be in the range of unity. By choosing $c_\gamma = 0$, the compression velocity can be forced to $(\mathbf{V}_r)_f = 0$.

Using the indicator function, the local density ρ and the local viscosity μ of the fluid are given by:

$$\rho = \gamma \rho_a + (1 - \gamma)\, \rho_b \tag{3.28}$$

$$\mu = \gamma \mu_a + (1 - \gamma)\, \mu_b \tag{3.29}$$

where the subscripts *a* and *b* denote the different fluids.

The Navier-Stokes equations are adopted to describe the fluid motion for an incompressible fluid. Due the existence of interface, an additional term which is related to the surface tension force appears in the momentum equation and its determination is also necessary to capture the interface movements. The mass continuity and momentum equations read:

$$\nabla \cdot \mathbf{V} = \mathbf{0} \tag{3.30}$$

$$\frac{\partial \rho \mathbf{V}}{\partial t} + \nabla \cdot (\rho \mathbf{V}\mathbf{V}) = -\nabla p + \nabla \cdot \tau + \rho \mathbf{g} + \mathbf{F}_{sa} \tag{3.31}$$

where t is the time, τ is the stress tensor, $\mathbf{g}$ stands for the gravity and p denotes the pressure. The last term which appears in the right hand side of Eq. 3.31 $\mathbf{F}_{sa}$ represents the source of momentum due to the surface tension force acting at the interface. The phenomenon of surface tension is attributed to the cohesive forces among water molecules. In the bulk of the liquid, each molecule is pulled equally in every direction by neighboring liquid molecules, resulting in a net force of zero. The molecules at the surface do not have other molecules on all sides of them and therefore are pulled inwards. This creates some internal pressure and forces liquid surface to contract to the minimal area. Therefore, surface tension is defined as the force along a line of unit length, where the force is parallel to the surface but perpendicular to the line.

In VOF method, the exact position of interface is unknown and the interface movements are tracked implicitly by evaluating the variation of the indicator function γ and, consequently, its exact shape and location are smeared in the simulation. Here, the Continuum Surface Force (CSF) formulation by Brackbill et al. [10] is used to calculated the surface tension force from the distribution of the indicator function. Although the interface cannot be directly obtained from the simulation, the surface tension force is calculated as a continuous volumetric force acting within the transition region instead of a surface force acting on the sharp interface. The surface force per unit interfacial area can be written as:

$$\mathbf{F}_{sa}(\mathbf{x}_s) = \sigma \kappa(\mathbf{x}_s)\, \mathbf{n}(\mathbf{x}_s) \tag{3.32}$$

where σ denotes the surface tension coefficient, κ is the curvature of interface, $\mathbf{x}_s$ is a vector which represents the position of a certain point in space and $\mathbf{n}$ denotes the normal vector of interface. In order to obtain the volumetric force acting within the transition region, the sharp interface is replaced by a transition region that is not aligned with the grid. Within the transition region, the unit normal vector of the transition region is gradient of the indictor function γ and the curvature of interface is calculated as gradient of the unit normal vector. Contours of the indicator function shown in Fig. 3.7 illustrate the position of variables employed in the simulation.

The volumetric force $\mathbf{F}_{sv}$ should give the correct surface tension force per unit interfacial area $\mathbf{F}_{sa}$ when the width of transition region approaches zero:

$$\lim_{h \to 0} \int_{\Delta V} \mathbf{F}_{va}(x) d^3x = \int_{\Delta A} \mathbf{F}_{sa}(x) dA \tag{3.33}$$

where the area integral is over the portion ΔA of the interface lying within the small volume of integration ΔV. The volume ΔV is constructed so that its edges are normal to the surface and its thickness h is small compared with the radius of curvature of the interface A. Hence, the surface tension force $\mathbf{F}_{sa}(\mathbf{x}_s)$ in Eq. 3.31 is replaced with the volumetric force acting within the transition region $\mathbf{F}_{va}(\mathbf{x}_s)$ to formulate the momentum equation for a Newton fluid in the presence of surface tension force.

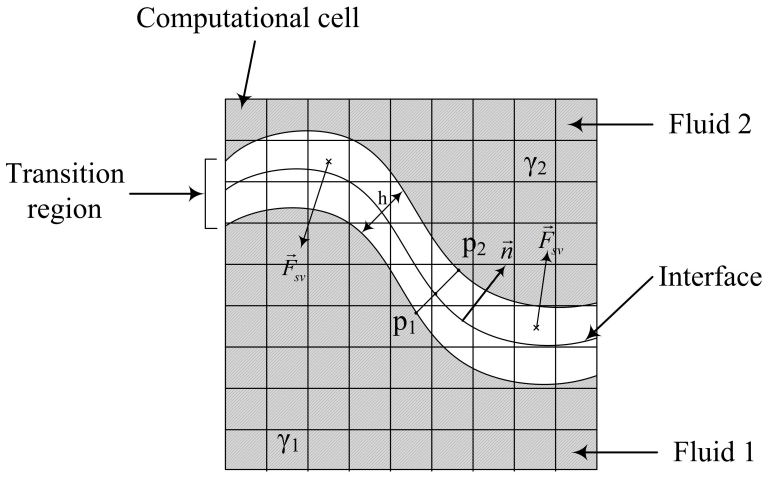

Fig. 3.7: Sketch of the surface tension force and related parameters within the transition region

To evaluate $\mathbf{F}_{va}(\mathbf{x}_s)$, $\mathbf{F}_{sa}(\mathbf{x}_s)$ is rewritten as a volume integral for $h = 0$ and an integral of $\mathbf{F}_{sa}(\mathbf{x}_s)$ over a volume V containing the interface A is converted to an integral over A of $\mathbf{F}_{sa}(\mathbf{x}_s)$ evaluated at that surface. Consequently, it is found that the volume force $\mathbf{F}_{va}(\mathbf{x}_s)$ for finite h can be expressed as:

$$F_{va}(\mathbf{x}_s) = \sigma\kappa(\mathbf{x}_s)\nabla\gamma \tag{3.34}$$

The curvature of a surface A at $\mathbf{x}_s$, κ, is calculated from:

$$\kappa = -(\nabla \cdot \mathbf{n}) \tag{3.35}$$

In CSF model, the interface is replaced by a transition region whose normal gradient of the indicator function is:

$$\mathbf{n}(x) = \nabla\gamma \tag{3.36}$$

The curvature within the transition region is thus:

$$\kappa = \nabla \cdot \left(\frac{\nabla\gamma}{|\nabla\gamma|}\right) \tag{3.37}$$

Therefore, the volumetric force $\mathbf{F}_{va}$ is given by:

$$\mathbf{F}_{va} = \sigma\nabla \cdot \left(\frac{\nabla\gamma}{|\nabla\gamma|}\right)\nabla\gamma \tag{3.38}$$

Since $\nabla\gamma$ is non-zero only in the transition region, the surface volume force is also non-zero only in the transition region.

It should be noted that Eq. 3.30 and Eq. 3.31 are valid for the whole flow field including the interface. Based on the Newtonian law of viscosity, the stress tensor is given by:

$$\tau = \mu\left(\nabla\mathbf{V} + \nabla\mathbf{V}^T\right) \tag{3.39}$$

here μ is the local kinetic viscosity calculated by Eq. 3.29.

Eq. 3.30 and Eq. 3.31 are solved by the segregated pressure correction method. First, only the terms containing the velocities $\mathbf{V}$ are taken from the momentum equation, and a system of

linear algebraic equations can be defined. This preliminary equation is solved and provides a guessed velocity. With substitution of the discretized momentum equation into the continuity equation, a pressure equation is obtained. After solving the pressure equation, the velocity field is then updated with the corrected pressure. This so-called pressure-velocity coupling will be repeated till both momentum and continuity equations are converged. This method gives an oscillation-free velocity filed in line with the Rhie-Chow correction, even though there is no explicit Rhie-Chow correction. More detained description of this method can be found in Klostermann et al. [35] and Rusche [67].

Turbulence modeling

LES model is a very popular model to investigate the turbulent properties in the flow field. The basic equations of LES model were first formulated by Smagorinsky [83]. Based on the theory of Kolmogorov [37] in which the smallest scales of motion are uniform and these small scales serve mainly to drain energy from the larger scales through the cascade process, it is assumed that the small scales can be successfully approximated. The large scales of motion, which contain most of the energy and do most of the transporting, are strongly influenced by the boundary condition and need to be calculated directly, while the small scales are represented by a model.

In this model, low-passing filtering is applied to the Navier-Stokes equations to separate small scales from the large scales of motion. The filter width Δ which denotes a characteristic length-scale is a very important property related to the filtering process. The scales of motion larger than Δ of the flow field are retained in the filtered flow field and directly solved as direct numerical simulation (DNS) does, while the scales smaller than Δ (Sub-Grid Scale (SGS)) need to be modeled artificially. Therefore, any flow parameter f is decomposed into a large scale and a small scale contribution as:

$$f = \tilde{f} + f' \tag{3.40}$$

where the prime denotes the small scale and the tilde stands for the large scale. To extract the large scale components from the real flow field, the resolved part $\tilde{f}(\mathbf{x}, t)$ of a space-time variable $f(\mathbf{x}, t)$ is defined formally by the relation (Sagaut [72]):

$$\tilde{f}(\mathbf{x}, t) = \int_{-\infty}^{+\infty} \int_{-\infty}^{+\infty} f(\xi, t')\, G(\mathbf{x} - \xi, t - t') dt d^3\xi \tag{3.41}$$

where $G(\mathbf{x} - \xi, t - t')$ is the filter kernel. Several filter kernels have been applied to the modeling of LES model and include: the Gaussian filter, the top-hat filter and the sharp Fourier cutoff filter and so on. The detailed discussion about the difference between the various filters can be found in de Villiers [19].

If this filtering process is applied to the incompressible Navier-Stokes equations, the filtered equations of motion are obtained as:

$$\nabla \cdot \tilde{\mathbf{V}} = 0 \tag{3.42}$$

$$\frac{\partial \tilde{\mathbf{V}}}{\partial t} + \nabla \cdot \left(\tilde{\mathbf{V}}\tilde{\mathbf{V}}\right) = -\frac{1}{\rho}\nabla \tilde{p} + \nu \nabla \cdot \left(\nabla \tilde{\mathbf{V}} + \nabla \tilde{\mathbf{V}}^T\right) - \nabla \cdot \tau_{sgs} \tag{3.43}$$

where $\tilde{\mathbf{V}} = (\tilde{u}_x, \tilde{u}_y, \tilde{u}_z)$ is the filtered velocity field. $\tilde{p}$ is the filtered pressure. The term τ_{sgs} is known as the sub-grid scale stress (SGS) which reflects the effect from the subgrid part of the velocity field on the resolved field through the subgrid-scale model. Its component τ_{ij} is calculated as:

$$\tau_{ij} = \tilde{u}_i \tilde{u}_j - \widetilde{u_i u_j} \tag{3.44}$$

τ_{ij} has the property that $\left|\tau_{ij}\right| \rightarrow 0$ as $\Delta \rightarrow 0$, so that in the limit of small mesh spacing a DNS solution is returned. The filtered Navier-Stokes equations look very similar to RANS model. However, the predicted physics of the problem is somewhat different in LES. In LES model, the dissipative scales are generally not resolved. The main role of the SGS model is therefore to extract energy from the resolved scales, mimicking the drain associated with the energy cascade [19]. This is accomplished with a linear eddy-viscosity model which is based on the hypothesis that the non-uniform component of the SGS stress tensor is locally aligned with the resolved non-uniform part of the rate of strain tensor. The normal stresses are taken as isotropic and can therefore be expressed in terms of the SGS kinetic energy:

$$\tau_{ij} - \frac{1}{3}\tau_{kk}\delta_{ij} = -2\nu_{sgs}\tilde{S}_{ij} \tag{3.45}$$

It relates the subgrid-scale stress τ_{ij} to the large-scale strain rate tensor $\tilde{S}_{ij}$. The coefficient ν_{sgs} is the sub-grid scale eddy-viscosity.

This first relation for the sub-grid scale eddy-viscosity was firstly developed by Smagorinsky [83] and used in the first LES simulation by Deardorff [21] in which the energy production and dissipation of the small scales are assumed to be in equilibrium and all the energy received from the resolved scales is dissipate entirely and instantaneously. And it is by analogy to the mixing-length hypothesis and modeled as:

$$\nu_{sgs} = (C_S\Delta)^2 \left|\tilde{S}\right| \tag{3.46}$$

where $\tilde{S}$ is the characteristic filter rate of strain, Δ is the filter width and C_S is the Smagorinsky coefficient whose value is between 0.1 to 0.2. The value of Δ is taken by averaging the grid size in three directions as:

$$\Delta = \left(\Delta_x\Delta_y\Delta_z\right)^{1/3} \tag{3.47}$$

where Δ_i stands for the grid size in the direction of axis-i.

To evaluate the filtered rate of strain, an expression is formed by employing the filtered velocity gradient $\nabla\tilde{\mathbf{V}}$:

$$\tilde{S}_{ij} = \frac{1}{2}\left(\nabla\tilde{\mathbf{V}} + \nabla\tilde{\mathbf{V}}^T\right) \tag{3.48}$$

and on this basis, the characteristic filtered rate of strain is defined by:

$$\tilde{S} = \sqrt{2\tilde{S}_{ij}\ \tilde{S}_{ij}} \tag{3.49}$$

The Smagorinsky model suffers from its excessive dissipation in high shear region, so that the parameter C_S must be decreased in these situations. Van Priest damping function has been proposed to adjust the value of C_S in the near-wall region. It reduces the sub-grid eddy-viscosity as a function of wall-normal distance as:

$$C_S = C_{S0}\left(1 - e^{y^+/A^+}\right) \tag{3.50}$$

where y^+ denotes the dimensionless distance from the wall, A^+ is a semi-empirical constant and a typical value of 25.0 is used. C_{S0} is the Van Driest constant which is equal to 0.1. Although this treatment is still not desirable since the SGS model should preferably depend exclusively on the local flow properties, the Smagorinsky model has been successfully applied to the simulations of different flow field. So far, the simplest LES model named as Smagorinsky model is closed.

The assumption of equilibrium means that the Smagorinsky model will become correspondingly less accurate while the flow strays further from this condition. To overcome this

drawback, an alternative SGS model named as one equation model which was developed by Deardorff [22] and used by Moeng [49] was proposed by adding a transport equation to solve the sub-grid scale turbulent kinetic energy k_{sgs} equation explicitly. Advantages of this model are that no equilibrium assumption is required, and the prognostic equation provides a direct mean of calculating the SGS kinetic energy. In this model, the sub-grid kinetic energy is defined as:

$$k_{sgs} = \frac{1}{2}\sum_{i}(\tau_{ii}) \tag{3.51}$$

which provides a SGS velocity scale.

The transport equation of k_{sgs} can be derived by a transformation of the filtered equations of motion which is similar to RANS model. Based on the assumption of SGS isotropy, the equation of SGS kinetic energy is given by Yoshizawa and Horiuti [97]:

$$\frac{\partial k_{sgs}}{\partial t} + \tilde{\mathbf{V}} \cdot \nabla k_{sgs} = P - \varepsilon + D \tag{3.52}$$

where the various terms on the right-hand side are shear production P, dissipation ε and diffusion D.

Terms in the above expression can be directly computed or modeled as:

$$\begin{aligned} P &= -\tau_{ij} : \tilde{S}_{ij} \\ \varepsilon &= C_{\varepsilon}\frac{k_{sgs}^{3/2}}{\Delta} \\ D &= \nabla \cdot \left(\left(\nu + \nu_{sgs}\right)\nabla k_{sgs}\right) \end{aligned} \tag{3.53}$$

where C_{ε} is a constant whose value is equal to 1.048.

Hence, the expression of SGS eddy-viscosity is modified to:

$$\mu_{sgs} = \rho C_k \Delta \; k_{sgs}^{1/2} \tag{3.54}$$

where C_k is a constant whose value is equal to 0.094.

All the governing equations are integrated into the three-dimensional finite-volume CFD platform *OpenFOAM* which is constituted by a large base library and offers the core capabilities of dynamic mesh, automatic parallelization, several general physical model, and so on.

3.5.2 Validation calculation of the employed CFD approach with experimental and numerical data

As discussed before, the wake velocity is required to estimate the increased rising velocity of the affected bubble. Under low Re_b condition, an accurate description of wake velocity profile is achieved based on laminar boundary layer theory. As bubble diameter increases, a deformed bubble is expected as well as an unstable wake structure. In this case, difficulties arise at the unstable boundary layer around bubble interface where the separation of boundary layer happens. A periodic vortex shedding, which leads to a greater complexity of the vortex structure, is also observed. Furthermore, it is found that wake instability is the primary cause of path instability of bubble which may have negative impacts on the prediction accuracy of wake velocity. Due to these features, laminar boundary layer theory ceases to be valid at high Re_b, and it is almost infeasible to propose an analytic expression to estimate the velocity profile of unstable wake accurately. Until now, the knowledge of how to estimate the wake velocity

profile at high Re_b is still quite limited. In the following study, this problem is circumvented by using CFD approach, which has potential to provide a detailed description of the flow field in an unstable wake. In this section, in order to show that CFD approach is capable to capture the interface movements and predict the wake properties at high Re_b, we advance our studies by validating the simulation results against the experimental data and DNS results. Therefore, appropriate experimental and numerical studies need to be selected.

To validate the employed CFD approach, an essential point of validation is an appropriate definition of target parameters to show how the performance of simulation is. The requirements of these parameters should include two aspects: firstly, it should be easily obtained from literature; secondly, it is representative to the subject of interest. In the current study, we mostly focus on the prediction accuracy of wake velocity profile. However, the velocity profile of unstable wake is barely reported in the literature. So that, other parameters which are deemed to depend on the wake properties are chosen. These parameters include: bubble terminal velocity, path instability and vortex structure. Furthermore, in order to ensure that the wake structure is unstable, the bubble diameter should be sufficiently large. With respect to these two criteria, experimental study of a single bubble rising freely in the water conducted by Brücker [11] and DNS simulation carried out by Gaudlitz and Adams [25] are chosen in the current study for validation purposes. In their studies, most of the provided parameters are quite suitable for assessing the prediction accuracy. The simulation results will be directly compared with them and a good agreement between them will demonstrate the capability of the employed approach to capture the interface movements and predict the wake properties under high Re_b condition.

In this section, an overview of the numerical configuration used in the simulation is firstly provided, followed by a series of sensitive analysis which focuses on the influences from mesh resolution, geometry size and turbulence model. The validation process with the above mentioned experimental and numerical studies is provided in the third section. Finally, important conclusions obtained from the validation process will be summarized and discussed.

Overview of numerical configuration

In the simulation, a large diameter bubble is placed in a rectangle channel in which the stagnant water is filled. Both air and water are at room temperature and treated as incompressible, immiscible fluid. The heat flux and mass exchange are excluded. All the physical properties including density, viscosity and surface tension coefficient are summarized in Tab. 3.1.

$\rho_l[kg/m^3]$	$\rho_g[kg/m^3]$	$\nu_l[m^2/s]$	$\nu_g[m^2/s]$	$g[m/s^2]$	$\sigma[kg/s^2]$
1000	1.25	1e-6	1.44e-05	9.8	0.073

Tab. 3.1: Physical properties of the investigated air-water system under room temperature

Regarding turbulence model, both Smagorinsky model and one equation model summarized in section 3.5.1 are utilized and compared in the simulation. The size of simulation domain is dependent on the bubble equivalent diameter d. It is composed by a cuboid $5d \times 5d$ square and $14d$ high. A spherical bubble is initially positioned $4d$ below the top of the domain. The simulation domain with the simulated bubble is schematically shown in Fig. 3.8. To prove that this configuration provides a best compromise between the requirement of prediction accuracy and computational efforts, sensitive analysis will be provided to show that the influence from the size of simulation domain can be neglected.

The simulated bubble keeps rising in the simulation and its motion through the rising process is comparable to the height of simulation domain. To avoid extending the domain in the

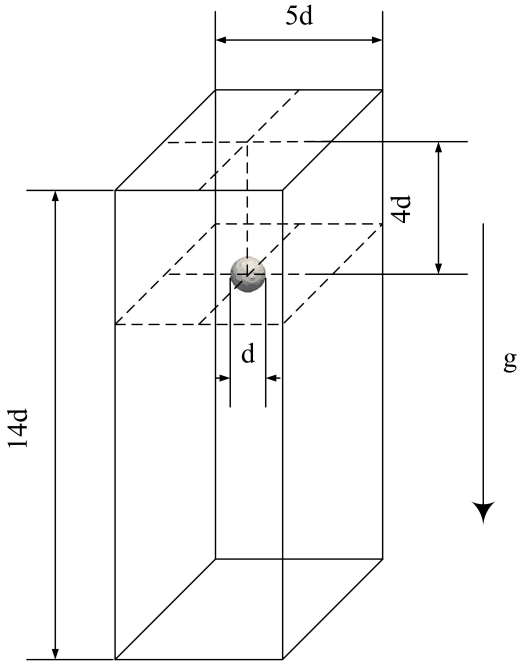

Fig. 3.8: Sketch of the simulation domain for simulating a single bubble rising in the stagnant water

gravity direction, the position of bubble center is always kept in its initial position by translating the mesh via tracking the bubble center. The uniform mesh displacement is calculated based on the movement of bubble at every time step along the bubble rising direction. This simple methodology minimizes the demand against the geometrical size of simulation domain and speeds the simulation up.

In the following sensitive analysis, the equivalent diameter of the simulated bubble is set to 5 mm. The corresponding dimensionless numbers are summarized in Tab. 3.2 with characteristic scales for the length d and for the rising velocity $u = \sqrt{gd}$. From this table, it is seen that the inertial force is more prominent compared with the viscous force due to a large Re_b.

Name	Re_b	Eo	Mo
case1	1107	3.35	2.52e-11

Tab. 3.2: Summary of dimensionless numbers for the sensitive analysis of the numerical configuration

In order to ensure a proper convergence of the solutions, the final residuals of pressure, velocity and turbulence properties are 10^{-8} for every time step. In addition, in order to guarantee a sharp and bounded solution, the multidimensional universal limiter with explicitly solution (MULES) implemented in OpenFOAM is used to integrate the γ-equation explicitly. The transient term in the momentum equation is discretised by the backward scheme which is second order scheme, and generally the cell face values in the convective terms are determined by the second order schemes.

Sensitivity analysis of mesh resolution

The performance of LES model depends on the mesh resolution and the interactions of small scales at bubble interface can be well captured by a good mesh structure. However, the requirement of memory space and computational time increases much faster compared to the increment of mesh number. The limitation of computational power comes to a compromise

between the desired performance of numerical simulation and the number of cells in practical engineering application.

Due to its simplicity, good numerical accuracy and stability, uniform structured grid is adopted to generate the mesh. Following the work conducted by Bothe et al. [8], a criterion named cells per bubble diameter (CPD) is introduced to study the influence from grid resolution on the predicted results. A sensitive analysis of grid resolution is made with CPDs of 12, 15, 18 and 20. Four mesh structures with their total numbers of finite control volume are summarized in Tab. 3.3. Due to limitation on computational resource, the computation with a higher CPD larger than 22 is not performed. The mesh resolution in the near wall region is increased while approaching the wall. With a finer mesh in the near wall region, the turbulent structures in the whole flow field are resolved directly without introducing any simplifications.

Name	size	CPD	total grids
Mesh1	$5d \times 5d \times 14d$	12	725760
Mesh2	$5d \times 5d \times 14d$	15	1417500
Mesh3	$5d \times 5d \times 14d$	18	2449440
Mesh4	$5d \times 5d \times 14d$	20	3360000

Tab. 3.3: Summary of total mesh numbers for the sensitive analysis of mesh resolution

In Fig. 3.9, the bubble terminal velocities predicted by four mesh structures are obtained from the simulation results and plotted against CPD. It is clearly seen that, as CPD increases, the predicted terminal velocities tend to fall on a line as CFD increases. When CPD is larger than 15, the terminal velocity of the simulated bubble is almost a constant and its value is almost 0.205 m/s. The experimental data of a single bubble is almost 0.207 m/s [88] and indicated as a black line in this figure. It can be concluded that, when CPD is large than 15, the employed CFD approach predicts the bubble terminal velocity with an acceptable accuracy and a good agreement between simulation and experiment is achieved.

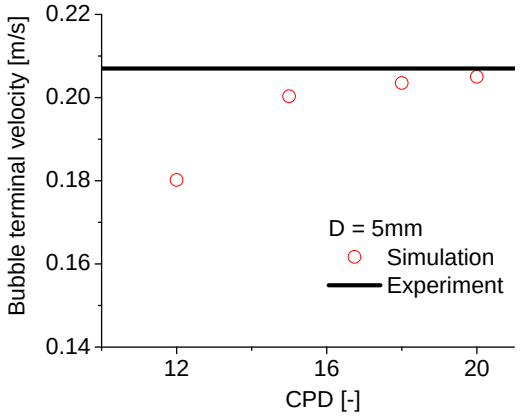

Fig. 3.9: Prediction of bubble terminal velocities with different mesh resolutions (d=5mm)

The surface tension force acting on the bubble interface is inversely proportional to the bubble diameter. For a small bubble, its spherical shape is kept due to this force. As bubble diameter increases, it is gradually deformed from a spherical bubble to an oblate one. In Fig. 3.10, the snapshot of the computed bubble shape obtained in Mesh3 is provided, showing that its shape is deformed obviously. The obtained bubble shape which is like an oblate spheroid is consistent with the one expected based on the experimental observation (Tomiyama et al. [88]).

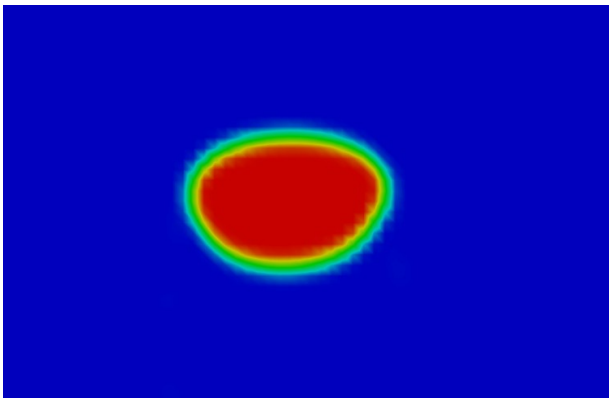

Fig. 3.10: Snapshot of a deformed bubble obtained in Mesh3 (d=5mm)

The bubble aspect ratios provided by four mesh structures are also compared and plotted against CPD in Fig. 3.11, using the major and minor axes obtained from the simulation results. In order to assess the deformed bubble shape obtained in the simulation, a correlation proposed by Wellek et al. [94] is employed to estimate the aspect ratio of a single bubble and shown as follows:

$$E = \frac{1}{1 + 0.163 Eo^{0.757}} \tag{3.55}$$

In Fig. 3.11, it is illustrated that the variation of bubble aspect ratios is quite similar to that of bubble terminal velocity. As CPD increases, the predicted aspect ratios tend to approach a constant value. When CPD is large than 15, the predicted bubble aspect ratio is almost 0.68. The value provided by Wellek's model is a little larger 0.71 and it is indicted as a black line in this figure. It is seen that the difference is small and the simulation predicts the deformed bubble shape with an acceptable accuracy.

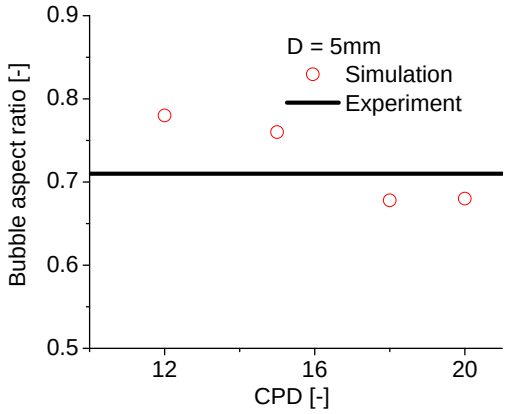

Fig. 3.11: Comparison of bubble aspect ratios with different mesh resolutions (d=5mm)

From the sensitive analysis of mesh structure, it is illustrated that when the parameter named grids per bubble diameter reaches 18, the effect from the grids can be neglected. In the following analysis, this criterion is adopted.

Sensitive analysis of geometry size

The sensitive analysis of geometry size is carried out to minimize the influence from the simulation domain. Seven cases are made in the current study, in which the size of simulation

domain varies in both lateral and vertical directions with the same CPD=18 suggested in the previous section. The employed geometry sizes are summarized in Tab. 3.4. As reported in the literature, a large diameter bubble exhibits an oscillating trajectory in the lateral direction. In Case1, Case2, and Case3, the influence from the lateral size of simulation domain is analyzed. Since the wake structures develop in the vertical direction, a longer channel in the vertical direction is very helpful for capturing the evaluation of wake. In Case2, Case4, Case5 and Case6, the influence from the height of simulation domain is studied. In this part of simulation, the same numerical configuration as the sensitive analysis of mesh resolution is adopted.

Name	X	Y	Z
Case1	4	4	14
Case2	5	5	14
Case3	6	6	14
Case4	5	5	10
Case5	5	5	12
Case6	5	5	16

Tab. 3.4: Summary of geometry sizes for the sensitive analysis of simulation domain

In Tab. 3.5, the terminal velocities predicted by seven different geometry sizes are summarized. It can be seen that the discrepancy of predicted terminal velocities in all seven cases is quite small. Furthermore, the predicted aspect ratios summarized in Tab. 3.6 also exhibit a similar behavior. It can be concluded that the behavior of bubble motion can be well captured by different geometry sizes and a good prediction accuracy is achieved in the simulation. Nevertheless, Case2 is chosen in the following simulation. Compared to other geometries, it provides a good compromise between the geometry size in the vertical direction and the computation efforts.

-	Case 1	Case 2	Case 3	Case 4	Case 5	Case 6
V_T [m/s]	0.204	0.205	0.214	0.205	0.207	0.204

Tab. 3.5: Summary of predicted terminal velocities in the sensitive analysis of geometry size

-	Case 1	Case 2	Case 3	Case 4	Case 5	Case 6
E [-]	0.64	0.68	0.651	0.679	0.684	0.704

Tab. 3.6: Comparison of predicted aspect ratios in the sensitive analysis of geometry size

Sensitive analysis of turbulence model

Two LES models have been briefly described in the previous section. In this part, the influence from turbulence model is discussed and the employed models are summarized in Tab. 3.7. The mesh resolution and geometry size are selected based on the previous sensitive analysis.

Name	Turbulence model
T1	One equation model
T2	Smagorinsky model

Tab. 3.7: Summary of LES models employed in the simulation

Similar to the previous studies, the predicted terminal velocities and bubble aspect ratios are summarized in Tab. 3.8 and Tab. 3.9, respectively. As shown in these two tables, the predicted values of terminal velocity and bubble aspect ratio do not depend on the choice of turbulent model. Smagorinsky model, which gives a good prediction of both parameters, is employed in the current study due to its simplicity and stability

-	T1	T2
V_T [m/s]	0.214	0.205

Tab. 3.8: Comparison of predicted terminal velocities in the study of turbulence model

-	T1	T2
E [-]	0.651	0.68

Tab. 3.9: Comparison of predicted aspect ratios in the study of turbulence model

Comparisons of simulation results with literature

In this section, the validation calculations are carried out against DNS simulation of Gaudlitz and Adams [25] and experimental study of Brücker [11] in which a single bubble is studied. The simulation is initialized with a spherical bubble within a liquid at rest. It should be noted that, in the simulation of Gaudlitz, the viscosity of mixture which consists of 90% mass fraction water and 10% glycerin is twice that of pure water with a viscosity ratio $\mu_b/\mu_l = 1/27$, but density and surface tension remain almost constant. The bubble diameters and the corresponding dimensionless numbers are summarized in Tab. 3.10. The computational domain of the size $L_x \times L_y \times L_z = 5d \times 5d \times 14d$ has been discretized by $N_x \times N_y \times N_z = 90 \times 108 \times 252$ grid cells. Moreover, all the numerical configurations are chosen based on the previous sensitive analysis. With these parameters and configurations, a large diameter bubble rising with a zigzagging trajectory is obtained and it will be validated further in the following sections.

Name	Case A	Case B
Reference	Brücker [11]	Gaudlitz and Adams [25]
d [mm]	5.22	5.2
Re_b	1181	587
Eo	3.66	3.63
Mo	2.52e-11	4.03e-10

Tab. 3.10: Bubble diameters with the corresponding dimensionless numbers for validation calculation of the employed CFD approach

The simulations cover several periods of the lateral zigzagging bubble motion. From the obtained results which include the rising velocity, the ellipsoidal shape, and the oscillations both in rising velocity and in trajectory, it can be found that the employed CFD approach is capable of capturing the main features of the bubbles in both cases. For instance, vertical velocity component vs. time for both cases are plotted in Fig. 3.12. The occurrence of a zigzagging motion, typical of the considered range of Re_b, is observed in both cases. Moreover, the instantaneous bubble rising velocity clearly shows that the motion of bubble exhibits a complex velocity oscillation. Its maximum value is reached for a short period, followed by a sharp decrement as the simulated time advances. When the simulated time is sufficiently large, the simulated bubble reaches its steady state and shows an oscillation both in rising velocity and in trajectory. The time-averaged values of their oscillating rising velocities are 0.208 and 0.21 m/s in Case A and Case B, respectively. Meanwhile, the obtained results in literature are 0.204 and 0.226 m/s, respectively. Both of them are indicated as black lines in two figures. It can be observed that a good agreement is achieved when the simulated bubbles reach their steady state.

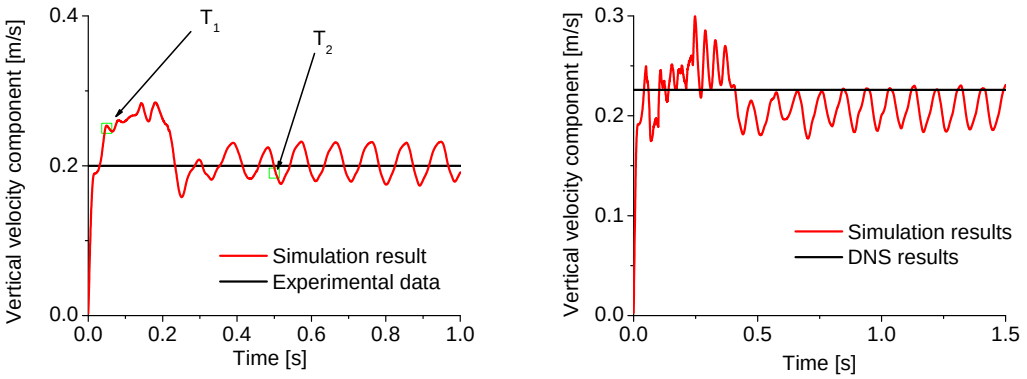

(a) Case A **(b)** Case B

Fig. 3.12: Rising velocity vs. time for an air bubble rising in the stagnant water obtained in Case A and Case B

A more detailed evaluation of the simulations can be obtained from the predicted bubble terminal velocities when bubble diameter varies. Experimental data for the teminal velocity V_T, of air bubbles rising in water with relations to equivalent diameter is shown in Fig. 3.13, reproduced from Clift et al. [17]. Data are given for bubbles rising in a pure system (upper line) and in a "contaminated system" (lower line), while the region in between is shaded. As shown in this figure, the experimental data is classified in three main regimes. For small diameters the bubble is spherical and rises along a rectilinear path. For very large bubbles the bubble shape is spherical cap like. The bubbles simulated in the current study fall into the intermediate regime and denoted as ellipsoidal. This regime is the most complex one. It is indicated that surfactants which are unavoidable in the industrial processes have a significant on the bubble motion. The predicted terminal velocities are also plotted in Fig. 3.13. It is indicated that a good agreement is achieved if considering large scatter of the experimental data. This confirms the ability of computational fluid dynamics to effectively simulate such an air-water system.

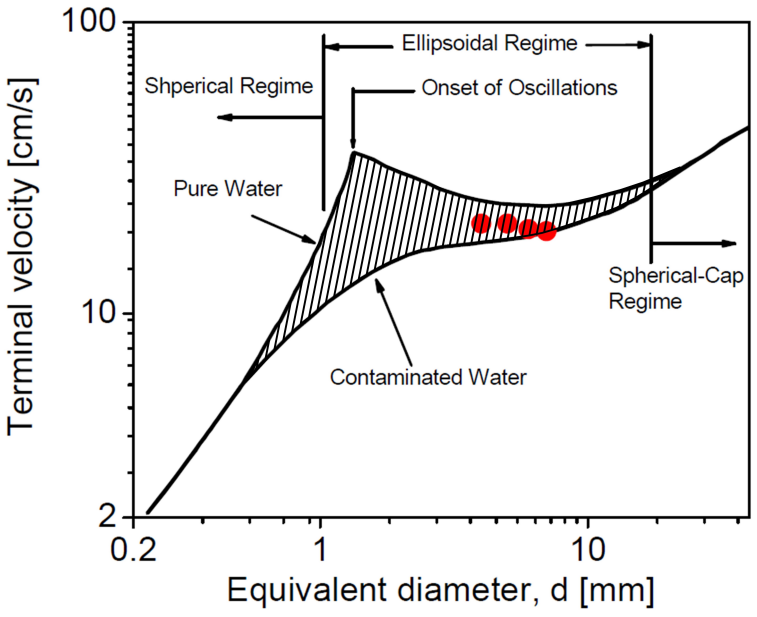

Fig. 3.13: Terminal velocities obtained in the simulation of bubbles with different diameters and compared with experimental data reproduced from Clift et al. [17]

The snapshot of the computed bubble shape obtained in Case A is shown in Fig. 3.14, with the velocity vectors around the bubble interface. It is obvious that the bubble shape is ellipsoidal and in agreement with the one expected based on the experimental observation of Brücker. The predicted bubble shape is also compared with experimental data quantitatively. The obtained aspect ratio in the simulation is 0.67, while the experiment gave a little bit smaller value 0.66. It can be concluded that the discrepancy is small and CFD approach can predict the deformed bubble shape with an acceptable accuracy.

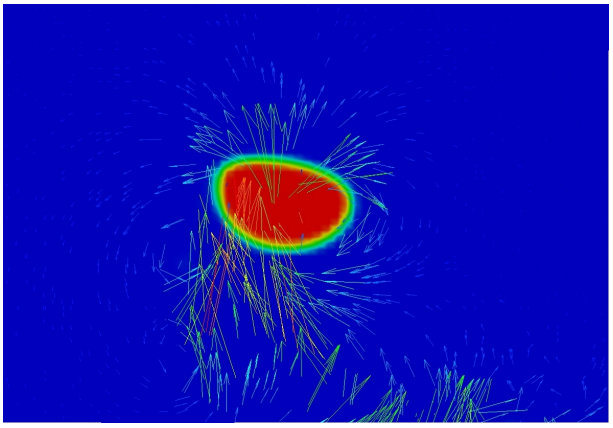

Fig. 3.14: Air bubble freely rising in water (Case A)

The phenomenon that bubbles in the ellipsoidal regime exhibit an oscillation both in velocity and in bubble path is a very interesting topic. In Fig. 3.12, it is clearly indicated that the vertical component of the simulated bubble shows a complex oscillation when its steady state is reached. Usually, the dynamic behaviors of unstable wake are attributed to this instability. It is found that the wake instability induces an oscillatory instability of both bubble path and velocity. In order to take a deep look at this phenomenon, the wake structures at time T_1 and T_2 as indicated in Fig. 3.12 are displayed in Fig. 3.15. Time T_1 and T_2 correspond to the straight path and the planar zigzagging path, respectively. It is illustrated that the wake structure at time A is axis-symmetric. Meanwhile, a three-dimensional wake which is composed by two counter-rotating vortices is observed at time B. As the bifurcation of the rising velocity evolution occurs, a breaking of the axial symmetry of the initial wake is observed and its structure becomes three-dimensional. This results in the decrease of the vertical velocity component of the simulated bubble due to the reduced pressure in the cores of the unstable vortices underneath the bubble. A similar phenomenon is also reported in the DNS simulation by Mougin and Magnaudet [54].

The wake instability which is closely related to the interactions between the wake and the external flow happens continuously during the simulation. It is manifested by cyclic phenomena of vortex formation and shedding [43] and leads to a zigzagging trajectory of bubble. The corresponding zigzagging trajectory is reproduced in Fig. 3.16. According to this figure, the bubble successively follows a straight path, and eventually a planar zigzag path. The bifurcation of the rising velocity evolution corresponds to a breaking of the axial symmetry of the initial wake as discussed before. It should be noted that the zigzagging trajectory of bubble remains in a vertical plane during the simulation. This phenomenon can be also explained with consideration of the wake structure which still preserves symmetric with respect to a plane perpendicular to that of the vortices and containing the symmetry axis of the bubble in the simulation.

The zigzagging motion of the bubble is observed in the simulation and its amplitude is also an interesting topic. In the experiment of Brücker, the zigzagging motion of the bubble is clearly seen as a sinusoidal function of the lateral coordinate over time with amplitude of

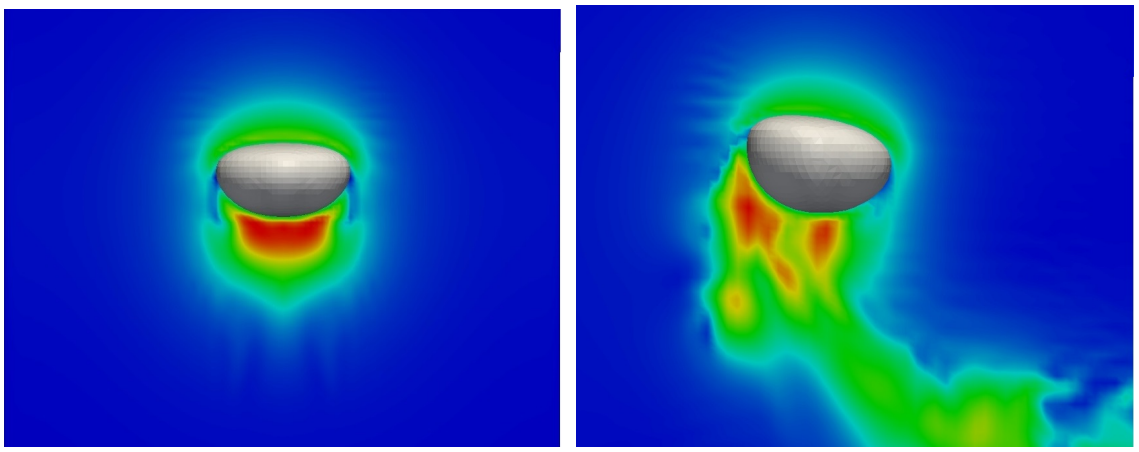

(a) Time T_1 **(b)** Time T_2

Fig. 3.15: Contour of the wake velocity profiles at different times (Case A)

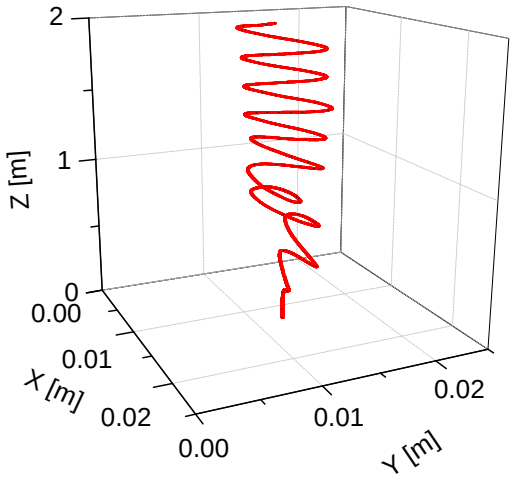

Fig. 3.16: Rising trajectory of the simulated bubble obtained in Case A(x,y: horizontal axes).

7.8 mm and frequency of 4.66 Hz. In Case A, the amplitude of the zigzagging motion in the lateral direction is almost 8 mm as indicated in Fig. 3.17, and a spectral analysis of the bubble lateral motion reveals a frequency nearly 4.8 Hz. Both of them have a good agreement with the experimental data.

Moreover, the lateral velocities obtained in Case A are also plotted against time in Fig. 3.18. It is clearly indicated that the evolutions of lateral velocities can be also treated as a sinusoidal function over time with amplitude of almost 0.12 m/s. In the experiments of Brücker, the maximum lateral velocity is found to be up to approximately 0.1 m/s. And in the simulation of Gaudlitz this value is 0.09 m/s. The simulation overestimates the maximum lateral velocity slightly.

By considering the time evolution of the bubble velocity which is calculated as $U_b(t) = \sqrt{u_b(t)^2 + v_b(t)^2 + w_b(t)^2}$, the instantaneous acceleration of the bubble $A(t)$ can be determined by:

$$A(t) = \frac{dU_b(t)}{dt} \tag{3.56}$$

The instantaneous acceleration of bubble obtained in Case B is plotted against time in

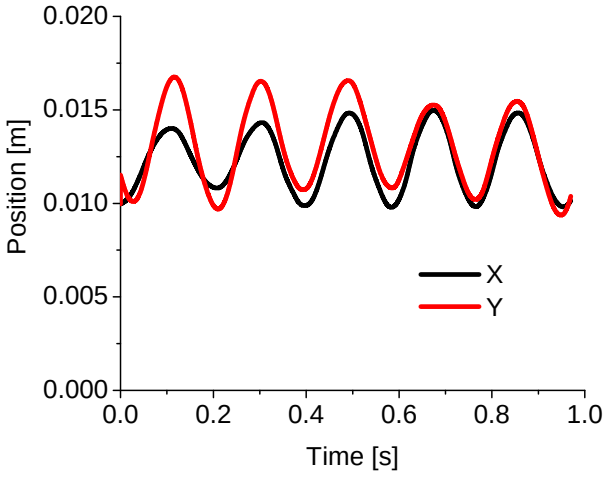

Fig. 3.17: Bubble lateral movements obtained in Case A (x,y: horizontal axes).

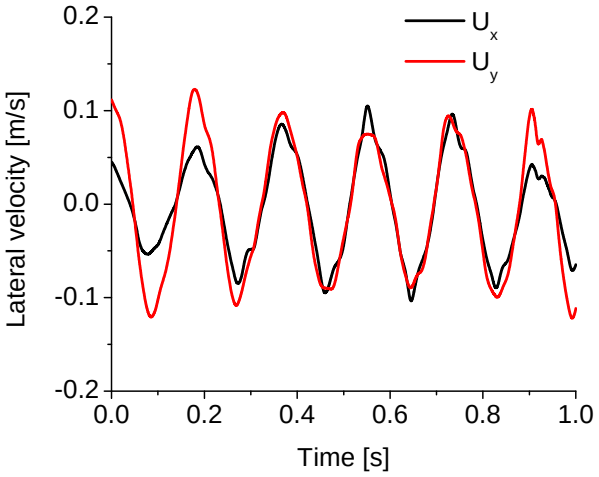

Fig. 3.18: Bubble lateral velocities obtained in Case A (x,y: horizontal axes).

Fig. 3.19. It is shown that, the bubble experiences periodically negative and positive accelerations of up to almost $\pm 2.2 m/s^2$ in direction of its instantaneous motion, which is with the range of bubble accelerations found in simulations by Gaudlitz and Adams [25] and experiments by Lunde and Perkins [45]. A spectral analysis of $A(t)$ revealed a frequency of 25.6Hz for acceleration. In experiment by Lunde and Perkins [45] a similar value of 24.9Hz for a bubble of d = 5.04mm and in DNS simulations by Gaudlitz and Adams [25] a value of 26.2Hz for a bubble with a diameter of d = 5.2mm have been found.

The structure of wake is of importance to represent the wake properties. In general, the observed variation of the wake structure can be described based on the dual-wake-structure concept. In this concept, the wake consists of a primary wake and a secondary wake. As shown in Fig. 3.20, the existence of the primary wake which contacts with the lower interface of bubble is captured in Case A, while a secondary wake extends far downstream. In Case A, its Re_b falls into the range between 300 and 6000 in which wake is found to exhibit an unsteady motion. This criterion is proposed by Fan and Tsuchiya [23] to determine whether the wake exhibits an unsteady motion. If Re_b is larger than the second critical Reynolds number (about 100-300) and smaller than the third critical Reynolds number (above 6000), the wake shows an unsteady motion with a large-scale vertical structure. This phenomenon is

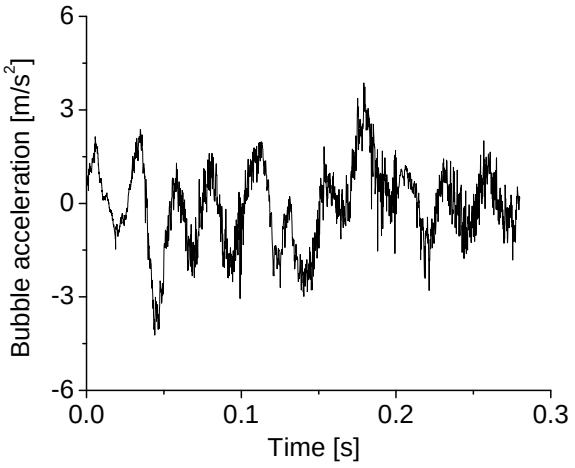

Fig. 3.19: Bubble acceleration rate in direction of the instantaneous motion.

captured in our simulation in which a periodic asymmetric wake about the vertical axis of the bubble movement is revealed. It is also consistent with the numerical simulation conducted by Li et al. [43].

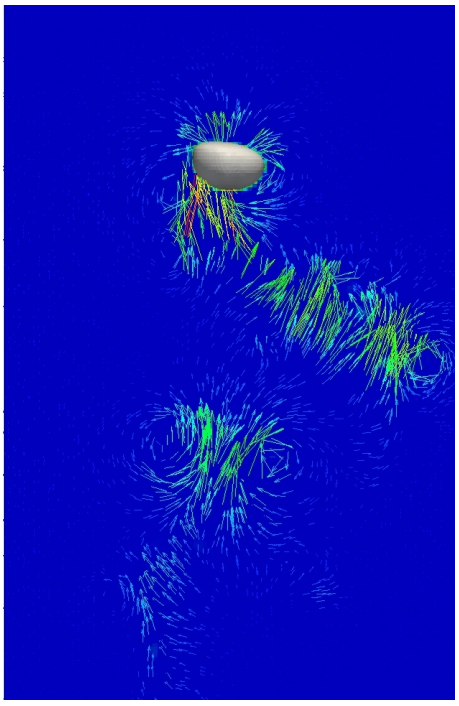

Fig. 3.20: Simulation results of bubble wake structure in Case A

A periodic formation and shedding of wake at the lower interface of bubble is related to the zigzagging ascent path of bubble. To give a detailed description about the structure of these vortices and consider its influence on the bubble motion, a snapshot of the bubble wake obtained in Case B is provided in Fig. 3.21. For this time instant, the bubble moves laterally in positive $x-$ and negative $y-$direction. The center of bubble is located at $4d$ below the top of simulation domain. In the region whose distance to the bubble center is smaller than $3d$, a chain of hairpin vortices which are generated at the lower interface of bubble can be observed. Four hairpin vortices exist in the vortex chain attached to the lower interface of bubble. In this figure, the distribution of vorticity is obviously non-uniform. It explains that the

lateral movement of bubble in positive $x-$ and negative $y-$direction is led by an asymmetric structure of wake. In the region which is more far away from the bubble center, a broken leg of the hairpin vortex chain is found. This vortex chain is generated because of previous path oscillation period. The dynamic of wake obtained in our simulation is quite similar to DNS results of Gaudlitz. As reported by Gaudlitz, the phenomenon that no complete hairpin vortex exists when the distance to the bubble center is larger than 5.5d is also found in our simulation. It is attributed to the breakup of the vortex chain and viscous dissipation.

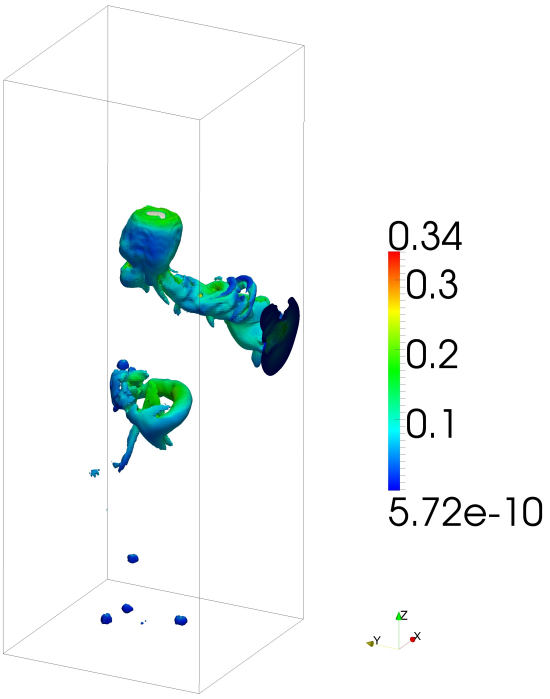

Fig. 3.21: Contour of vorticity generated by a zigzagging bubble at a time instant, colored with vertical liquid velocity

All the discussions above only focus on the wake structure. To provide a detailed evaluation of the shape and strength of vortex chain quantitatively, the vertical vorticity ω_z is calculated in a horizontal plane at distance $1.3d$ below the bubble center which cuts the vortex legs. The simultaneous lateral velocity of bubble is also indicated in the figure. In Fig. 3.22, it is illustrated that the asymmetric distribution of vorticity dominates the current lateral bubble motion in this time instant. The magnitude of the vertical vorticity is well within the range found in the numerical simulation of zigzagging bubbles with both fixed and varied shapes [25, 53]. In this figure, vortex system can be identified as a pair of vortex legs which is still preserves symmetric with respect to a plane perpendicular to that of the vortices and containing the symmetry axis of the bubble in the simulation. This can explain that the zigzagging trajectory is still in a vertical plane.

Conclusion and discussion

The comparison between the simulation results and the data found in the literature demonstrates the capability of VOF method with LES model to capture the interface movements and predict the properties of unstable wake. This is seen with validation calculations of experiment and DNS simulation conducted by Brücker [11] and Gaudlitz and Adams [25]. The diameter of the simulated bubble is in the ellipsoidal regime and its rising velocity and deformed shape, which is caused by the buoyancy force and surface tension force, are reasonably predicted. In addition, the parameters which are related to the wake properties are also well predicted.

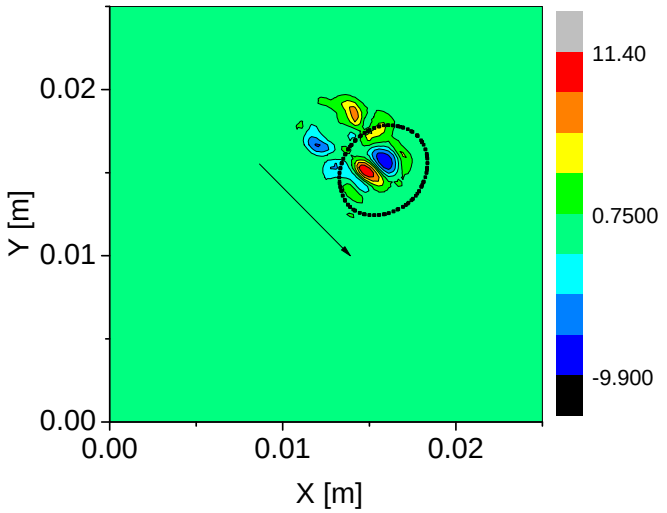

Fig. 3.22: Vertical vorticity in the bubble wake, seen from top view

A good agreement is successfully achieved while comparing the simulation results obtained in the current study against the characteristics of wake obtained in the DNS simulation by Gaudlitz and Adams [25]. It is shown that four hairpin vortices attached to the lower interface of bubble are present in the vortex chain, with which the simulated bubble exhibits oscillations both in rising velocity and in trajectory.

Furthermore, due to the lacking knowledge of three-dimensional measurement results, validation of the employed CFD approach is conducted on the basis of several macroscopical parameters which are related to the wake properties, i.e. the bubble oscillation frequency in trajectory, the amplitude of bubble oscillation and the bubble lateral velocity. As three-dimensional measurement or simulation results, such as the detailed wake velocity profile as well as the transient forces acting on the bubble interface, become available in the future, more validation calculations of the employed CFD approach summarized in this section should be carried out.

3.5.3 Simulation and analysis of wake velocity profile using CFD approach

Based on the validation calculations in chapter 3.5.2, VOF method with LES model is employed in the current study to investigate the velocity profile of unstable wake. The investigated wake is generated by a single bubble which is rising freely in the stagnant water. Its bubble Reynolds number is high and a deformed bubble is encountered. In order to employ the proposed drag force model in the simulation of industrial processes, in which bubble diameter varies over a wide range, it is more applicative to propose a general correlation to estiamte the wake velocity profile in terms of some characteristic parameters of the investigated bubble. It is also because of the limited computational resource. As mentioned before, turbulent boundary layer theory is employed to provide a expression of wake velocity, in which unknown parameters still exist. In the current study, the wake velocity profile obtained in the simulation will be used to fit all the unknown factors, with which a correlation of wake velocity profile is proposed.

In the following section, an overview of numerical configuration is firstly provided. After that, the wake velocity profile obtained in the simulation is investigated carefully. Two key distributions of wake velocity are examined in detail: the distribution of maximum wake velocity in

the vertical direction and the wake velocity profile in the radial direction. For this task, wake velocities at different locations are studied by posting-processing the simulation results. Finally, following the ideas proposed by Prandtl [62] and Sato and Sadatomi [76], the expression derived by turbulent boundary layer theory is closed by fitting the numerical results in terms of bubble diameter and bubble terminal velocity.

Overview of numerical configuration

In the current study, air-water system under room temperature and the corresponding physical properties are used as working fluid. Water is modeled as continuous liquid phase, while air as dispersed bubble whose diameter ranges from 4 mm to 7 mm. The choice of bubble diameter is based on the experimental data which are available in open literature. The selected experiments, which are under high Re_b conditions, can be classified into two groups: bubble chain and bubbly flow. In the experiment conducted by Tsuge and Hibino [91], several bubble chains which have the same diameter are studied. However, a wide range of bubble diameters is covered in the studies of bubbly flow and it is infeasible to cover all the possibilities. In the current study, the range of bubble diameter selected in the simulation covers the bulk of experimental studies. It is also the best option we could provide due to the limitation of computational efforts. Bubble diameters with their corresponding dimensionless numbers are summarized in Tab. 3.11.

Name	Case1	Case2	Case3	Case4
d [mm]	4	5	6	7
Re [$-$]	792	1107	1456	1834
Eo [$-$]	2.15	3.36	4.83	6.58

Tab. 3.11: Bubble diameters with the corresponding dimensionless numbers for the study of wake velocity profile

The numerical configurations, which includes mesh resolution and numerical schemes, are the same as the validation calculations as described in section 3.5.2. Several cross-sections which are vertical to the gravity direction are chosen to study the variations of wake velocity in different directions. A schematic sketch of the simulation domain with the chosen cross-sections are shown in Fig. 3.23. With a moving mesh whose velocity depends on the bubble rising velocity, the rising bubble is kept still with respect to the mesh. So that it is feasible to study the variation of wake velocity in both vertical and radial directions.

Maximum wake velocity distribution in the vertical direction

Eq. 3.9 is deduced based on turbulent boundary layer theory and several assumptions are employed to simplify the governing equations of wake. In this equation, the value of ν_{eff} is still undetermined. In order to prove that this expression has potential to provide a good estimation of the wake velocity profile under high Re_b condition, it is required to comprehensively compare its prediction against the simulation results.

In the current study, turbulent viscosity ν_t is assumed to be a constant, and its variation is also neglected in the calculations of Tennekes and Lumley [86]. Therefore, it is necessary to investigate the turbulent viscosity more closely to provide a justification for this assumption. If adopting the expression of turbulent viscosity which is proposed in the standard $k-\varepsilon$ model, turbulent viscosity is related to the ratio between turbulent kinetic energy k and turbulent dis-

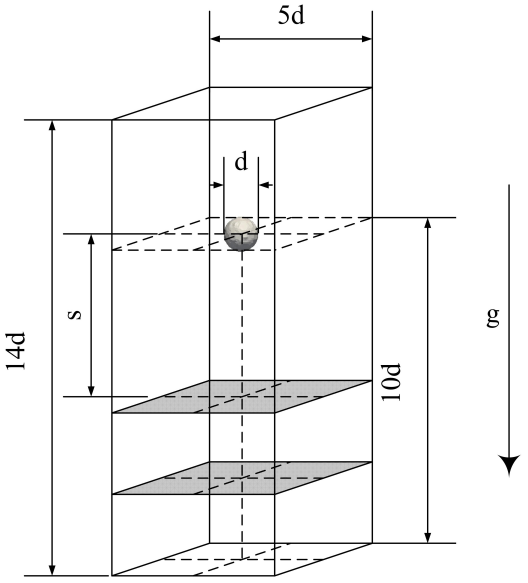

Fig. 3.23: Sketch of the simulation domain with the selected cross sections for sampling the wake velocity profile

sipation rate ε as follows:

$$\nu_t = C_\mu \frac{k^2}{\varepsilon} \tag{3.57}$$

where C_μ is a constant and its value is taken as 0.09. Turbulent dissipation ε is the rate at which turbulent kinetic energy is converted into the thermal internal energy and calculated as:

$$\varepsilon = \nu \overline{\left(\frac{\partial u'_i}{\partial x_k}\right)\left(\frac{\partial u'_i}{\partial x_k}\right)} \tag{3.58}$$

where prime denotes the velocity fluctuation. With these two equations, the distribution of turbulent viscosity is obtained from the simulation results. The assessment of the turbulent viscosity was performed by plotting the maximum value of turbulent viscosity of every cross-section against the vertical distance to the bubble center. In Fig. 3.24, the evolution of $\nu_t/(2aV_T)$ with relation to $s/(2a)$ is plotted. The results from simulation tend to fall on to a line when $s/(2a)$ is larger than 2. The constant turbulent viscosity indicates that, the flow is developing in the near-wake region until $s/(2a) = 2$, beyond which it appears to have settled into an equilibrium similarity state. In the far-wake region, a constant turbulent viscosity seems to be able to describe the turbulent properties in the wake. Therefore, a constant turbulent viscosity is acceptable in the investigation of the velocity profile of unstable wake, and the feasibility of the assumption employed in the derivation of Eq. 3.9 is examined.

As shown in Eq. 3.9, when the radial distance to the bubble centerline is equal to 0, the maximum value of wake velocity is obtained. For clearness, a parameter U_s is introduced to denote the maximum value of wake velocity for every cross-section. Its value is dependent on the bubble terminal velocity V_T, the effective viscosity ν_{eff}, the drag force coefficient C_d, the major axis of bubble a and the vertical distance to bubble center s. To understand the dependency of U_s and identify a promising direction for description, an investigations on the expression deduced by turbulent boundary layer theory is carried out. Following the above discussion, the effective viscosity ν_{eff} is assumed to be a constant and consequently, it can be found that a linear relationship between U_s and s^{-1} exists. For mathematical description of the dependency of U_s, Eq. 3.9 is simplified as:

$$\frac{U_s}{V_T} = k\left(\frac{s}{2a}\right)^{-1} \tag{3.59}$$

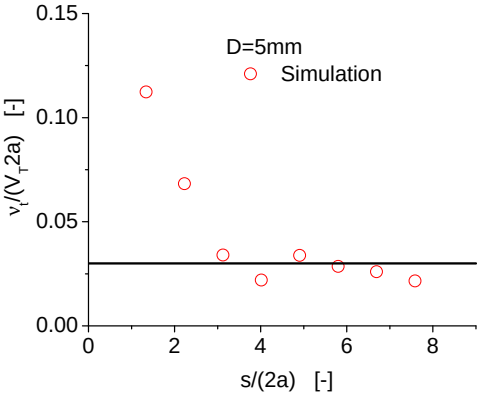

Fig. 3.24: Dependence of the turbulent viscosity ν_t on the vertical distance to the bubble center s ($d = 5mm$)

where k is a constant and equal to $C_d a V_T/16\nu_{eff}$. This relation shows the dependency of U_s on the vertical distance to the bubble center s. It implies that for a rising bubble, the maximum wake velocity decreases as s increases. Target of this set of simulation is to examine whether there is a dependency between the maximum wake velocity U_s and the vertical distance to bubble center s.

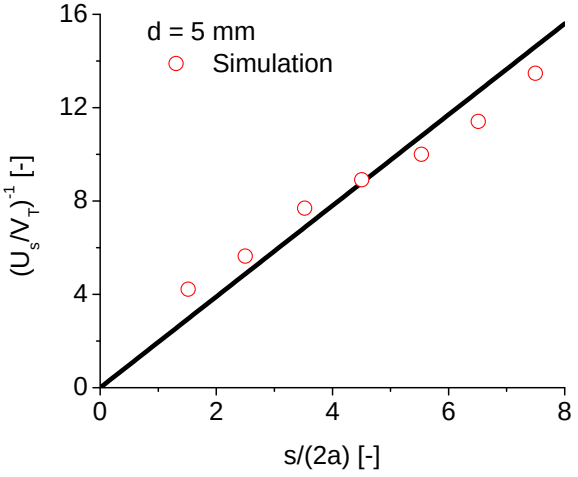

Fig. 3.25: Dependence of the characteristics velocity U_s on the vertical distance to the bubble center ($d = 5mm$)

In Fig. 3.25, the evolution of U_s/V_T with relation to s/d is plotted. As indicted in this figure, a fairly good linear relationship crossing the origin point between the normalized distance to the bubble center s/d and the ratio of the maximum wake velocity U_s to the bubble terminal velocity V_T is obtained. The slope of the obtained linear function is almost 1.95 and have a qualitatively agreement with Eq. 3.59 whose slope is equal to 2.09. Here, the determination of ν_{eff} will be discussed later. Moreover, it confirms the fact that the the variation of effective viscosity has negligible influence on the distribution of U_s while U_s is strongly dependent on the vertical distance to the bubble center. Based on the above discussion, it is shown that Eq. 3.9 is sufficient to evaluate the variation of U_s in the vertical direction.

In the wake, the turbulence intensity is assumed to be of order U_s, so that it can be expected that Reynolds stress may be also described by a relationship between the velocity fluctuation $\overline{u_i' u_i'}$ and the characteristic velocity U_s. If assuming that Reynolds stress is invariant

with respect to s, it can be expressed in terms of U_s. In order to examine the feasibility of this assumption, the choice for these similarity parameters should be appropriate. Here, following the work by Johansson [33], U_s and the maximum value of turbulent kinetic energy k_{max} are chosen, respectively. The ratio of $\sqrt{k_{max}}$ and U_s is plotted in Fig. 3.26 versus $s/(2a)$ as the plot of V_t/U_s against $s/(2a)$. It is indicated that the simulation results also tend to fall on to a line when $s/(2a)$ is larger than 2. The constant ratio of turbulent kinetic energy to the maximum wake velocity confirms that the flow is developing in the near-wake region until $s/(2a) = 2$. It is found that U_s seems to be able to describe the velocity fluctuation in the far wake region when Reynolds stress is invariant with respect to s and normalized by U_s.

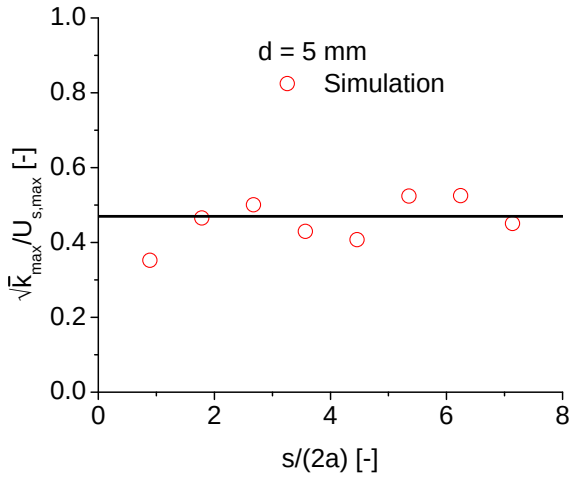

Fig. 3.26: Dependence of the turbulent intensity I on the vertical distance to the bubble center ($d = 5mm$)

The distributions of ν_t, U_s and Reynolds stress are described in the vertical direction. Following them, two important conclusions can be draw:

1. A strong dependency of U_s on the vertical distance to the bubble center s is revealed. It is acceptable to employ a simple function crossing the origin point to approximate the distribution of U_s in the vertical direction. It confirms the expression derived by turbulent boundary layer theory.

2. The normalized turbulent kinetic energy shows that it is appropriate to adopt U_s to describe the Reynolds stress when the equilibrium similarity state is reached. Moreover, the assumption that turbulent viscosity is a constant in the wake is also verified based on the simulation results.

Based on the above conclusion, attempts will be made in the next section to investigate the wake velocity profile in the radial direction.

Wake velocity profile in the radial direction

As given in Eq. 3.9, for every cross-section in which s is a constant, non-dimensional wake velocity can be obtained by multiply the reciprocal of U_s. This yields:

$$\frac{U_w}{U_s} = \exp\left(-\frac{r^2 V_T}{4 s \nu_{eff}}\right) \tag{3.60}$$

It is illustrated that the dependency of U_w/U_s on ν_{eff} is quite clear. In the previous part, ν_{eff} is assumed to be a constant, but no attempt is made to determine its value. In order to compare the wake velocity profile obtained in the simulation against the prediction of Eq. 3.60, the value of ν_{eff} should be estimated. For mathematical description of it, Prandtl [62] proposed a well-known hypothesis to approximate the turbulent viscosity in the wake behind a solid sphere as shown:

$$\nu_t = \kappa b u_{1,max} \tag{3.61}$$

where b is the width of the mixing zone, $u_{1,max}$ the maximum deficit velocity and κ is the Karman constant. This relation correlates turbulent viscosity with turbulent velocity scale and mixing length. However, establishment of these parameters requires an accurate prediction of wake properties, which is not feasible. Sato and Sadatomi [76] advanced the turbulence modeling for bubbly flow in which turbulence is enhanced due to the existences of gas bubbles. The "drift" phenomenon of liquid particles was considered and the following formula which has a similar form was proposed:

$$\nu_t = k' \alpha R U_r \tag{3.62}$$

where k' is an empirical constant, α is the local volume fraction and R and U_r are the bubble radius and relative velocity between two phases, respectively. Target of this set of simplification is to introduce a dependency of the turbulent viscosity ν_t on some parameters which can be obtained easily.

Generally no additional equation needs to be solved for quantifying turbulence in the liquid in these two methods. Rather simple algebraic correlations are used, based on the characteristics velocity and length of the concerned flow, to estimate the turbulent viscosity. Especially in Sato's model, the turbulent viscosity is poorly represented by the averaged bubble diameter and the relative velocity due to the lacking knowledge of the detailed information about the wake properties. Given the complexity of turbulence, a simple correlation is adopted in the current study to estimate the turbulence viscosity as long as it contains most of the relevant physical description of turbulence structure in the wake. With the combination of Eq. 3.61 and Eq. 3.62, the following basic formula is proposed:

$$\nu_t = 2 c \kappa V_T a \tag{3.63}$$

where c is a factor to incorporate the influence from all simplifications. With Eq. 3.63, turbulent viscosity with dependence on terminal velocity and bubble diameter is determined. It is seen that turbulent viscosity is a constant in the wake region. It is consistent with the founding in the previous section that the variation of turbulent viscosity in the vertical direction is negligible.

To determine the proportional factor c with dependence on bubble terminal velocity and bubble diameter and find the optimal value of it, the wake velocity obtained in the simulation are taken as the "true values". The best fitted line predicted by Eq. 3.60 is obtained by varying the value of c. In the following studies, the following equation is found to provide the most optimal value of wake velocity and employed to predict the turbulent viscosity in the wake. It is indicated that, with a small drag force coefficient, the turbulent viscosity can be neglected in the wake.

$$c = 0.035 \times C_d \tag{3.64}$$

With Eq. 3.64, turbulent viscosity ν_t is assumed to be dependent on drag force coefficient C_d. A justification for this assumption is quite necessary. As shown in Fig. 3.24, a constant turbulent viscosity is acceptable to describe the turbulent properties in the far wake region. Hence, the maximum value of turbulent viscosity of every cross-section is averaged in the vertical direction and plotted against the drag force coefficient of the simulated bubble when bubble diameter ranges from 4 to 7 mm, as shown in Fig. 3.27. As indicated in this figure, a

farily good linear relations ship crossing the origin point between the turbulent viscosity ν_t and the drag force coefficient C_d is obtained. It proves that Eq. 3.64 is sufficient to describe the variation of the factor c while bubble diameter varies.

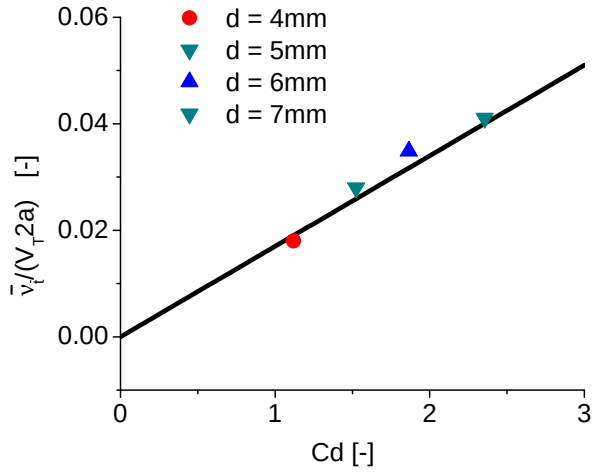

Fig. 3.27: Dependence of the averaged turbulent viscosity $\overline{\nu_t}$ on the drag force coefficient

With the proposed Eq. 3.63 and Eq. 3.64, Eq. 3.60 is then closed and can be employed to provide an estimation of wake velocity profile in the radial direction. When the vertical distance to the bubble center s varies, the obtained profiles are compared against the simulation results. As shown in Fig. 3.28, the predicted wake velocity profile for $d = 5mm$ are shown when s/d varies from 1 to 8. It is illustrated that when s/d is larger than 2, Eq. 3.60 has a good agreement with the simulation results. Therefore, Eq. 3.63, Eq. 3.64 and Eq. 3.10 will be employed to estimate the averaged wake velocity and compared with the simulation results when bubble diameter varies.

As shown in Fig. 3.29, the averaged wake velocity $\overline{U_w}$ obtained with the proposed correlations is plotted against the vertical distance to the bubble center s and compared with the simulation results. It can be found that, when bubble diameter ranges from 4 mm to 7 mm, the proposed correlation has a good agreement with the simulation results. The dependency of the averaged wake velocity $\overline{U_w}$ on the bubble diameter d is quite clear. $\overline{U_w}$ increases as d increases. To sum up, with a constant turbulent viscosity, a good agreement between simulation results and Eq. 3.9 can be achieved. Thus, this correlation will be employed to predict the drag force coefficient of the affected bubble in the following section.

3.5.4 Summary and comparison of the proposed drag force model

Summary of the proposed drag force model

For completeness, the proposed drag force model which includes correlations for the increased bubble rising velocity, the vertical distance between bubbles and the wake velocity profile are summarized here. The drag force coefficient of the affected bubble is estimated based on the balance between the drag force and the buoyancy force as:

$$C_{d,2} = \frac{4\left(\rho_l - \rho_g\right) gd}{3\rho_l V_{T,2}^2} \tag{3.65}$$

The key constitutive relation which correlates the relationship between the increased bub-

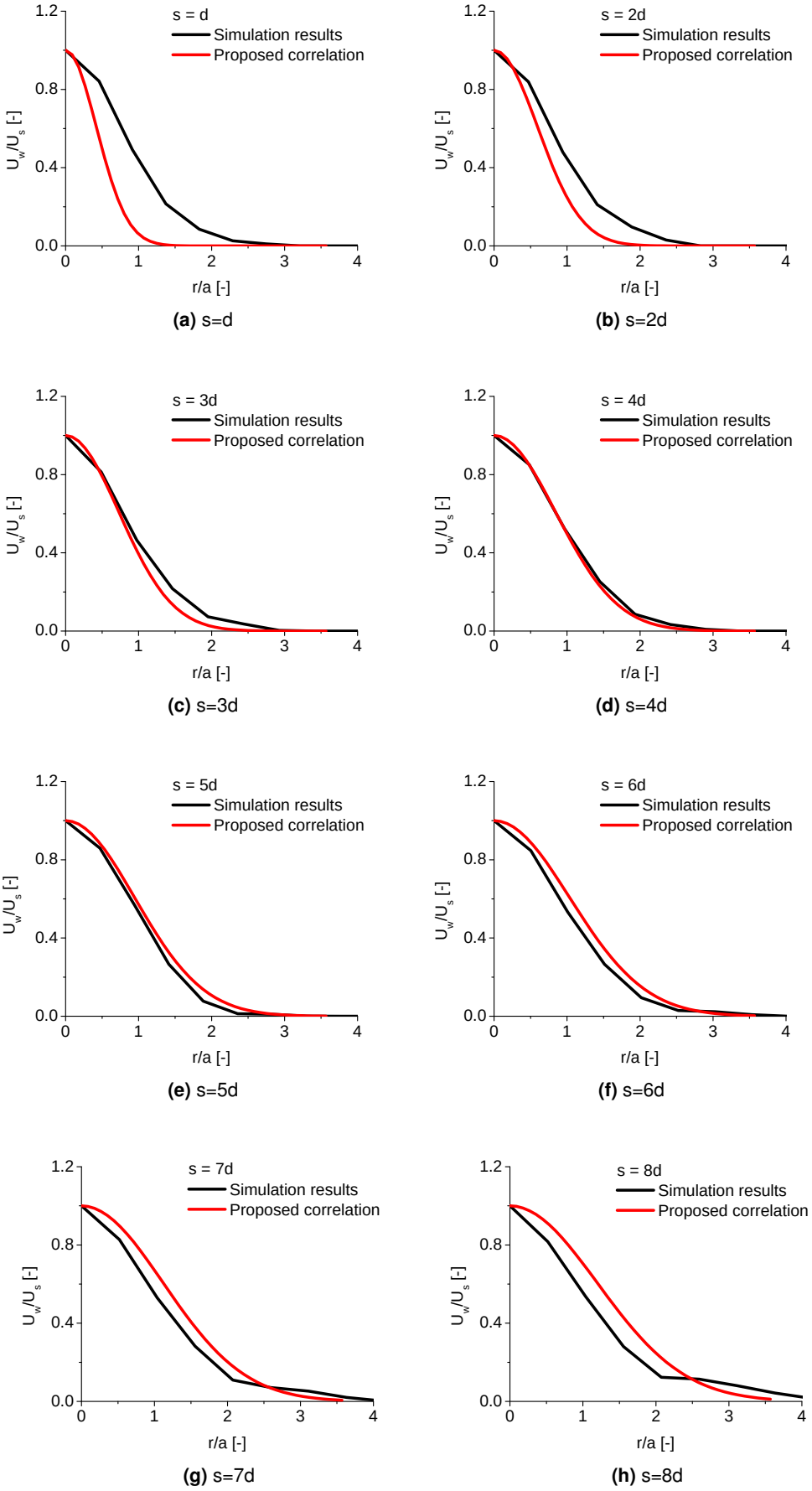

Fig. 3.28: Radial profiles of the predicted wake velocity normalized by its maximum value and compared with the proposed correlations (d=5mm)

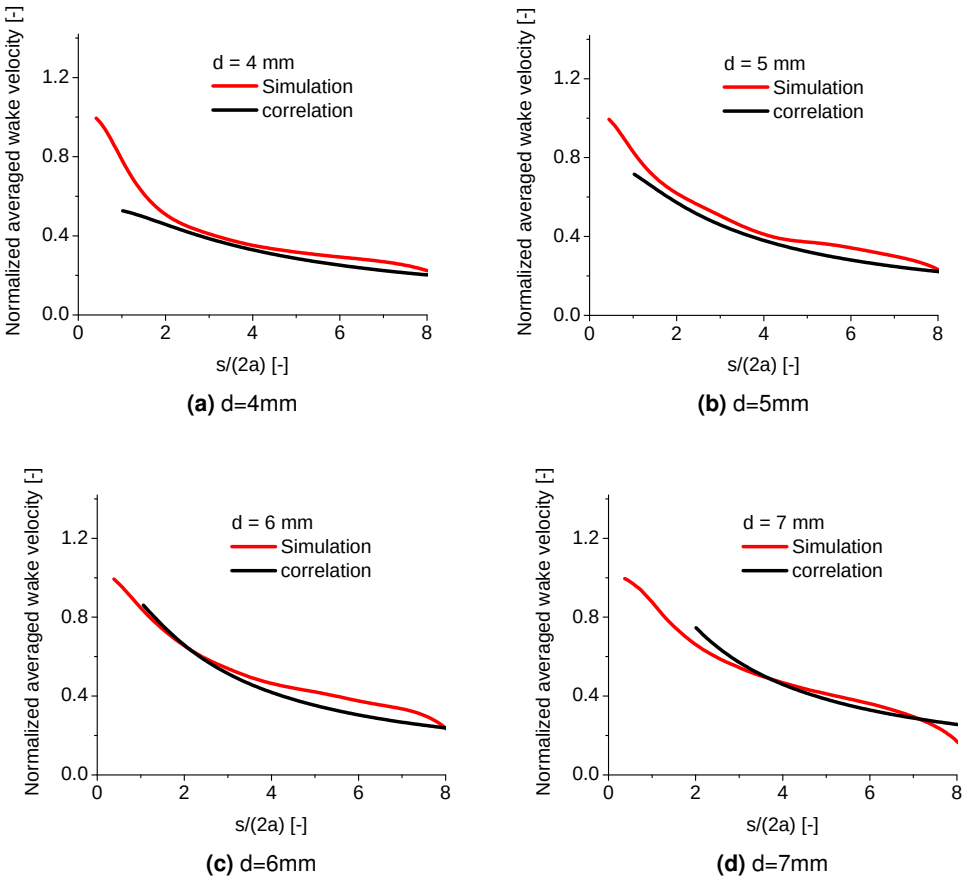

Fig. 3.29: Dependence of the normalized averaged wake velocity on the vertical distance to the bubble center and compared with the results predicted by the proposed correlations

ble rising velocity and the wake velocity is written as:

$$f(E)\sqrt{1-E^2}V_{T,2} - E\overline{U_w} = f(E)\sqrt{1-E^2}V_{T,1} \tag{3.66}$$

with $f(E)$ according to Eq. 3.20.

In Eq. 3.66, $V_{T,1}$ stands for the terminal velocity of a single bubble. Its value can be predicted by the drag force coefficient of a single bubble $C_{d,1}$ as:

$$V_{T,1} = \sqrt{\frac{4\left(\rho_l - \rho_g\right)gd}{3\rho_l C_{d,1}}} \tag{3.67}$$

where $C_{d,1}$ can be estimated by a lot of drag force models as summarized in Tab. 2.1 and Tab. 2.2.

Under low Re_b condition, if the vertical distance between two neighboring bubbles is equal to L, the following analytical expression can be employed to estimate the value of $\overline{U_w}$:

$$\overline{U_w} = V_{T,2}\frac{C_{d,2}}{2}\left(1 - \exp\left(-\frac{Re_{b,2}d}{16L}\right)\right) \tag{3.68}$$

Under high Re_b condition, attempts are made to calculate the velocity profile of unstable wake with turbulent boundary layer theory. It is written as:

$$\overline{U}_w = V_{T,2}\frac{C_{d,2}}{2}\left(1 - \exp\left(-\frac{V_{T,2}a^2}{4\nu_{eff}L}\right)\right) \tag{3.69}$$

Based on a systematic simulation covering a wide range of bubble diameter, a correlation is proposed to estimate the turbulent viscosity in terms of bubble terminal velocity and bubble diameter as:

$$\nu_{eff} = \nu_t + \nu = 2c\kappa V_T a + \nu \tag{3.70}$$

The factor c in Eq. 3.70 is dependent on the drag force coefficient as:

$$c = 0.035 \times C_d \tag{3.71}$$

For cases in which bubble aspect ratio is not provided, the correlation proposed by Wellek et al. [94] is employed as:

$$E = \frac{1}{1 + 0.163Eo^{0.757}} \tag{3.72}$$

Comparison of the proposed drag force model against the existing models

In this section, the proposed drag force model is compared against the existing models selected from literature. As summarized in chapter 2.5.2, Zhang and Fan [101] considered the influence from the reduced drag force, the added mass force and the basset force. It was also validated against experimental data when Re_b ranged from 3 to 35. Its expressions are given in Eq. 2.18, Eq. 2.19 and Eq. 2.20. Ramírez-Muñoz et al. [65] proposed a new reference fluid velocity when the flow structure of wake is highly non-uniform in the radial direction. This method was validate against the numerical results when Re_b ranged from 50 to 200. Its expression is summarized in Eq. 2.21 and Eq. 2.22.

As shown in Fig. 3.30, the performance of the proposed drag force model is compared with Zhang's model and Ramirez's model. In this figure, the averaged wake velocity $\overline{U_w}$ is estimated by Eq. 3.68. x and y axes denote the dimensionless distance between neighboring bubbles L/d and the velocity ratio between the affected and single bubble $V_{T,2}/V_{T,1}$, respectively. Overall, the increased bubble rising velocity decreases as L/d increases. From this figure, it is shown that the increased bubble rising velocity predicted by the proposed model is in between the models selected from the literature. Zhang's model predicts the highest values of $V_{T,2}/V_{T,1}$. The factor γ employed in Ramirez's model decreases as Re_b decreases and it contributes to an underestimation of $V_{T,2}/V_{T,1}$ when Re_b=3.

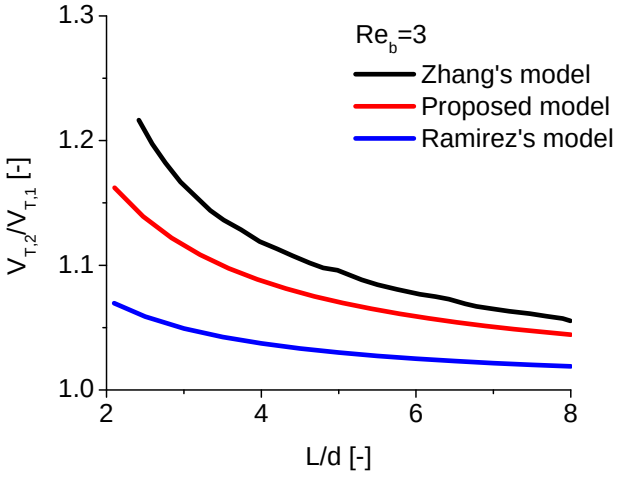

Fig. 3.30: Comparison of the proposed model and Zhang's model [101] when Re_b= 3.

For large diameter bubbles, Marks [48] proposed a model to estimate the rising velocity of bubbles rising in a chain and this model correlate the experimental data well when bubble diameter ranges from 1 mm to 8 mm. Its expression is written as follows:

$$\left(\frac{V_{T,2}}{V_{T,1}}\right)^{5/3} - \left(\frac{V_{T,2}}{V_{T,1}}\right)^{2/3} = K\left(\frac{gL}{V_{T,1}V_{T,2}}\right)^{1/3}\left(\frac{dV_{T,2}}{LV_{T,1}}\right) \tag{3.73}$$

As shown in Fig. 3.31, the performance of the proposed drag force is compared with Marks' model. In this figure, the averaged wake velocity $\overline{U_w}$ is estimated by Eq. 3.69 and bubble diameter is set to 5 mm. It is indicated that the distribution of the increased bubble rising velocity predicted by the proposed model is quite similar to the estimation of Marks' model. The difference between two models is that the predicted values of Marks' model is much larger than the proposed model.

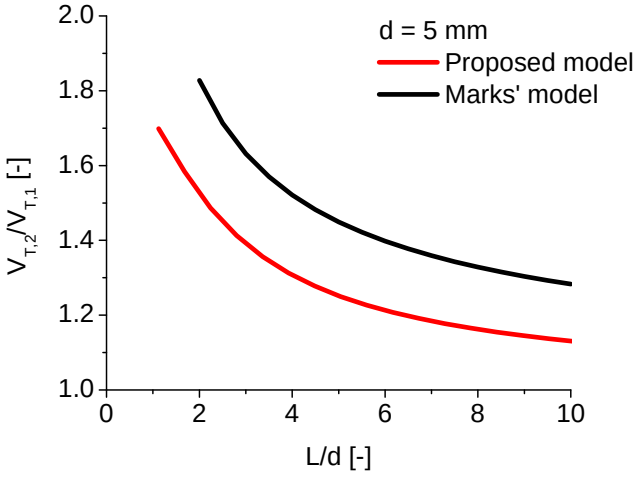

Fig. 3.31: Comparison of the proposed model and Marks' model [48] when d=5 mm.

3.6 Conclusion

In this chapter, a drag force model is proposed to account for the wake acceleration effect. Key constitutive relation of the newly proposed model is the modeling of the relationship between the increased bubble rising velocity and the wake velocity. The most important conclusions are summarized here:

- With consideration of the velocity distribution around the affected bubble which is modified by its surrounding wake, the new drag force model is derived. The constants in the model are obtained by the derivation proposed by Lamb [39] and no artificial factor is employed in the model. Hence, there is no necessity to optimize the proposed model.
- The derivation is based on the analysis of an oblate bubble. The increased rising velocity of the affected bubble is dependent on the wake velocity, the bubble aspect ratio and the terminal velocity of a single bubble. The solution of a spherical bubble can be easily obtained by taking the limit $E \rightarrow 1$.

Otherwise, the wake velocity which is required in the proposed drag force model is a very important topic in this chapter. When Re_b varies over a wide range, different expressions are employed to estimate its value. Descriptions about the wake velocity include two aspects:

- At low bubble Reynolds number, the influence from bubble deformation can be neglected. When the wake is regarded as a laminar flow, an analytic expression which is deduced based on laminar boundary layer theory is employed to estimate the wake velocity profile.
- At high Reynolds number, the influence from bubble deformation should be considered and the wake becomes turbulent. Based on systematic CFD analysis covering a wide range of bubble diameter, a close examination of wake velocity revealed that turbulent boundary layer theory has potential to evaluate the velocity profile of unstable wake in both vertical and radial directions. The approximation of constant turbulent viscosity in the wake is also justified. Finally, correlations are proposed to provide an estimation of wake velocity profile in terms of bubble terminal velocity and bubble diameter.

4. Validation of the proposed drag force model for bubbles aligned in line

In this chapter, the proposed drag force model will be validated against the experimental and numerical studies in which interactive bubbles are aligned in line vertically. Firstly, the proposed drag force model will be validated against experimental and numerical results of bubble pairs obtained at low Re_b. An analytical expression derived by laminar boundary layer theory is employed to evaluate the required wake velocity. Subsequently, the experimental studies of the wake effect on bubble rising velocity for air bubbles at high Re_b is employed in the validation calculations. Bubbles are in the ellipsoidal regime and the correlations which are proposed in chapter 3.5.3 are employed to estimate the wake velocity profile at high Re_b.

4.1 Bubble pairs at low bubble Reynolds number

In this part of work, the proposed drag force model is firstly validated against the experiment by Katz and Meneveau [34] in which Re_b ranges from 3 to 35. Subsequently, DNS results by Yuan and Prosperetti [98] are employed to validate the proposed drag force model when Re_b ranges from 50 to 200. In these two studies, the wake is still regarded as a laminar flow. As summarized in section 3.5.4, the analytical expression Eq. 3.68 is employed to estimate the velocity profile of laminar wake. It should be mentioned that the selected experiment and simulation were conducted to investigate the motions of a pair of two spherical bubbles rising in line vertically. It is found that the leading bubble remains almost unaffected by the proximity of the affected bubble. In this case, the averaged wake velocity experienced by the affected bubble is dependent on the rising velocity of the leading one whose rising velocity can be predicted by a lot of drag force models which are proposed for single bubble. For this reason, Eq. 4.1 is used in this part of validation calculations to estimate the value of wake velocity.

$$\overline{U_w} = V_{T,1}\frac{C_{d,1}}{2}\left(1-\exp\left(-\frac{Re_{b,1}d}{16L}\right)\right) \tag{4.1}$$

Tests from Katz and Meneveau [34]

Katz and Meneveau [34] performed experiments to measure the rising velocities of air bubbles rising in the stagnant water. The motions of interactive bubbles which were aligned in a straight line were visualized and Re_b ranged from 3 to 35. Their data of bubble rising velocity were measured at small Eo, therefore the trajectory oscillation and the deformation of bubble shape can be neglected in our analysis. In the experiment, the bubble rising velocity was measured while the vertical distance between bubbles L varied. The model calculation are conducted for three cases of bubble pair motion at Re_b of 3, 21 and 35, which corresponds to the bubble diameter 158, 349 and 475 μm, respectively. The corresponding single bubble rising velocities, $V_{T,1}$, were measured to be 19.5, 62 and 75 mm/s, respectively. Based on the relationship,

$C_{d,1} = 4gd(\rho_l - \rho_g)/3\rho_l V_{T,1}^2$, the drag force coefficients of the single bubbles are obtained as 5.43, 1.19 and 1.10 for the three cases, respectively. The above data for $V_{T,1}$ and $C_{d,1}$ are used in the present model calculation of the required wake velocity profile.

The performances of the proposed drag force model are compared with experimental data and shown in Fig. 4.1. x and y axes denote the dimensionless vertical distance between bubbles L/d and the rising velocity ratio between the affected bubble and a corresponding single one $V_{T,2}/V_{T,1}$, respectively. From these figures, it is shown that the proposed drag force model can predict the general trend of the increased bubble rising velocity varying with the vertical distance between bubbles. The ratio of $V_{T,2}/V_{T,1}$ increases with the decreasing vertical distance. It is always larger than the terminal velocity of a single bubble due to the wake acceleration effect. The best agreement is achieved in the far wake region. It is illustrated that the performances of the proposed drag force model in predicting the increased bubble rising velocity are excellent when the non-dimensional distance L/d is larger than 2 for all three cases. However, slight discrepancies between the predicted values and the measured data still exist in the near wake region. It is shown that the proposed drag force model underestimates the value of $V_{T,2}$ in comparison with the experimental data. These discrepancies may be related to the assumptions which are employed to deduce the analytic expression of laminar wake velocity. For an instance, one of the employed assumptions reads that the variation of wake velocity is negligible in comparison with the bubble rising velocity. This assumption is used to simplify the governing equation of wake and ceases to be valid in the near wake region. In this case, a good prediction accuracy of the increased bubble rising velocity cannot be achieved in the near-wake region where the wake velocity profile is not well predicted. In addition, the existence of a recirculation region which contacts with the lower interface of bubble is also observed. In the recirculation region, the radial component of wake velocity is somewhat comparable to its vertical component. Hence, the influence from the radial component of wake velocity cannot be excluded when L is sufficiently small.

Tests from Yuan and Prosperetti [98]

DNS simulation results by Yuan and Prosperetti [98] are also chosen for validation purpose. In the simulation, two bubbles were still aligned in line vertically and moved through an infinite Newtonian fluid along their centerline. Both of them had the same constant rising velocity $V_{T,1}$ which corresponded to the terminal velocity of a single bubble with the same diameter. The drag forces acting on the both bubbles were calculated by integrating the pressure and shear stress around the bubble interface.

In Yuan's simulation, it is clearly shown that the drag force acting on the affected bubble is greatly smaller than that of a single one. Due to the reduced drag force, the total force acting on the affected bubble is non-zero and its steady state is still not reached. However, as discussed before, the proposed drag force model correlates the increased bubble rising velocity with the wake velocity when the steady state is reached. Hence, to predict the reduced drag force coefficient provided by Yuan's simulation with the proposed drag force model, an additional correlation is required.

Firstly, we consider two time instants of the affected bubble. At the first instant, its rising velocity is equal to that of a corresponding single bubble $V_{T,1}$. This moment maps very specifically to the simulation condition carried out by Yuan. At the other instant, this bubble reaches its steady state and its rising velocity is denoted by $V_{T,2}$. The value of $V_{T,2}$ can be predicted by the proposed drag force model. With definitions of two instants, our assumption reads: the ratio of $V_{T,1}$ to $V_{T,2}$ is inversely proportional to the ratio of the corresponding drag force coefficients. This assumption is based on the work of Zhang and Fan [101] in which the drag force coefficient is assumed to be dependent on the bubble Reynolds number. It has

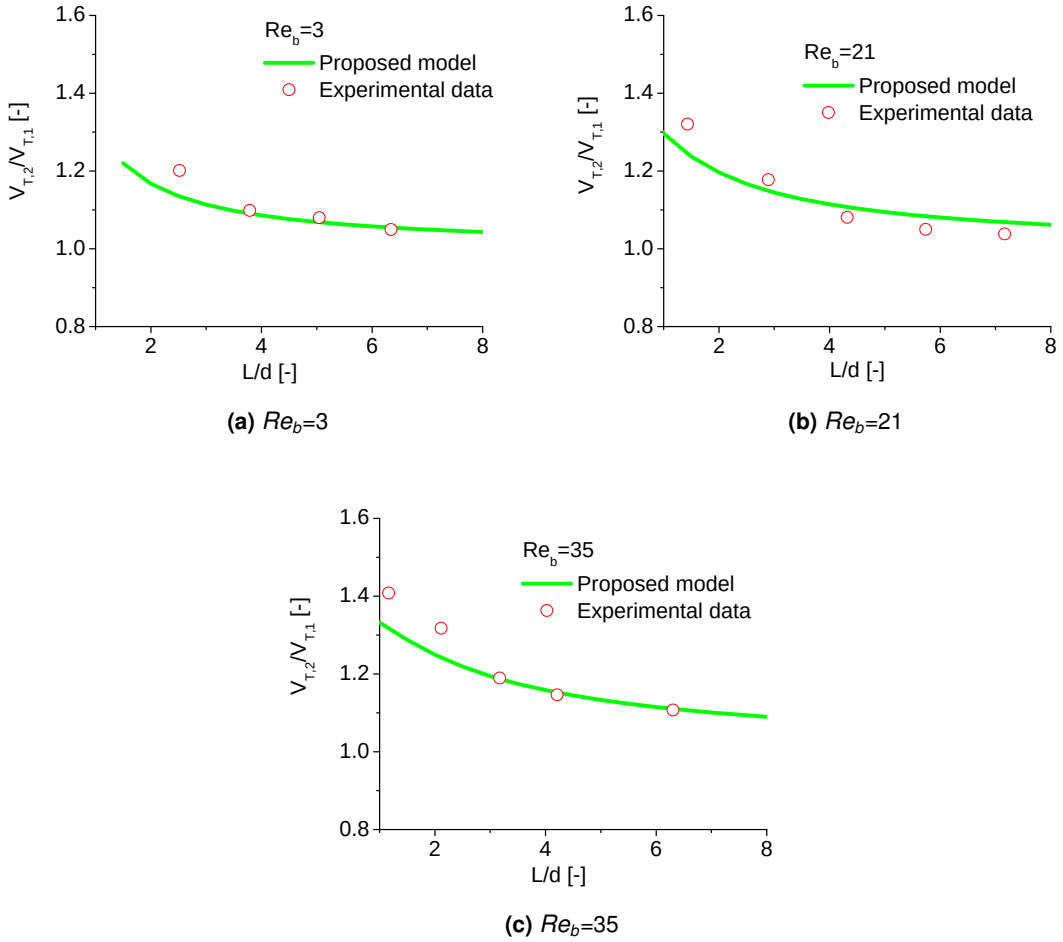

(a) Re_b=3

(b) Re_b=21

(c) Re_b=35

Fig. 4.1: Velocity ratio between the affected bubble and a corresponding single one with relations to L/d predicted by the proposed model and compared with the experimental data provided by Katz and Meneveau [34]

been verified for the case of particles aligned in tandem in a flow field for particle Re_b in the order of 100[100] and extended to the case of interactive bubbles whose Re_b is in the order of 10[101]. For the reason that this assumption is simple and gives a good approximation to the drag coefficient, it is employed in our analysis. Based on it, the reduced drag force coefficients are evaluated.

This assumption is given as a function of the bubble Reynolds number:

$$\frac{C_{d,y}}{C_{d,2}} = \frac{V_{T,2}}{V_{T,1}} \tag{4.2}$$

Here, $C_{d,y}$ is the reduced drag force coefficient predicted in Yuan's simulation and $C_{d,2}$ is the drag force coefficient predicted by the proposed drag force model. It is illustrated that when the rising velocity of the simulated bubble approaches to $V_{T,2}$, the same drag force coefficient can be expected. Moreover, Re_b ranges from 50 to 200 in Yuan's simulation.

Usually, drag force F_d is calculated as:

$$F_d = \frac{1}{8}\pi d^2 \rho_l C_d V_T^2 \tag{4.3}$$

If substituting Eq. 4.3 into Eq. 4.2 and employing Eq. 4.1, the drag force ratio can be

calculated as:

$$\frac{F_{d,2}}{F_{d,y}} = \frac{V_{T,2}}{V_{T,1}} = 1 + 0.67F\left(s, d, \mathrm{Re}_{b,1}, C_{d,1}\right) \tag{4.4}$$

where $F_{d,y}$ stand for the reduced drag force predicted in Yuan's simulation and $F_{d,2}$ is the drag force predicted by the proposed drag force model.

The predicted values are also compared with the Katz's model [34] which is written as:

$$\frac{F_{d,2}}{F_{d,y}} = 1 + F\left(s, d, \mathrm{Re}_b, C_d\right) \tag{4.5}$$

Comparison of the reduced drag force are shown in Fig. 4.2 with relations to the non-dimensional vertical distance L/d at different Re_b values. For purposes of comparison, the black lines indicate the predictions of Katz's model at Re_b of 50, 100 and 200 and the green lines are given by the proposed model. The presented model shows a very good agreement with Yuan's numerical results, especially when Re_b is equal to 50. However, the discrepancies are still evident in the near wake region, especially when L/d is smaller than 3. It is shown that the proposed model underestimates the reduced drag force in comparison with the simulation results by Yuan. As mentioned before, a similar trend is also observed under low Re_b conditions. It may be lead by the same reason that the predicted value of wake velocity needs to be improved in the near wake region.

The predicted values of Katz's model are also included in Fig. 4.2. It is illustrated that Katz's model overestimates the reduced drag force in all three cases. Although the discrepancy between Katz's model and the presented model keeps improving as Re_b increases, this asymptotic behavior can be explained by analyzing the dependency of the reduced drag force on the wake velocity. In both models, the same value of the averaged wake velocity $\overline{U_w}$ can be expected due to the same expression of wake velocity. However, in the proposed model, an addition factor which is equal to 0.67 appears in the expression and reduces the contribution from $\overline{U_w}$. Therefore, regardless of the value of $\overline{U_w}$, the drag force predicted by Katz's model are always smaller than the predicted values of the proposed model.

On the other hand, as the non-dimensionless vertical distance L/d increases, the discrepancy between Katz's model and the proposed model keeps improving. Compared to the near wake region, the value of the velocity ratio F is much smaller in the far wake region due to the dependency of the wake velocity on the non-dimensionless vertical distance L/d. It is shown that a slighter discrepancy between Katz's model and the proposed model can be expected in the far wake region due to the decreased velocity ratio F. According to our analysis, an appropriate factor employed in the term of F is capable of providing a good predictiona accuracy of the reduced drag force. In the proposed model, much of these discrepancies between Katz's prediction and Yuan's data are removed with the inclusion of a factor which smaller than unity. This factor is deduced in a more general way and only dependent on the bubble aspect ratio. No optimization is involved in its derivation.

For a bubble pair rising in the stagnant water, the inviscid inertia force needs to be considered, especially when the vertical distance between bubbles is smaller than 3. This force is equal to the inviscid component of the total pairwise interaction force found by Yuan and comes from the inertial effect of a body moving in fluid. The presence of the body induces a flow field that communicates pressure forces on other bodies. For a vertically aligned pair of equal-size bubbles simulated by Yuan, this force is symmetric, repulsive and decaying rapidly with vertical distance. This reflects the simple fact that the liquid entrapped in the gap between rising bubbles moves slowly and has a higher pressure. The repulsive force F_{HDI} experienced

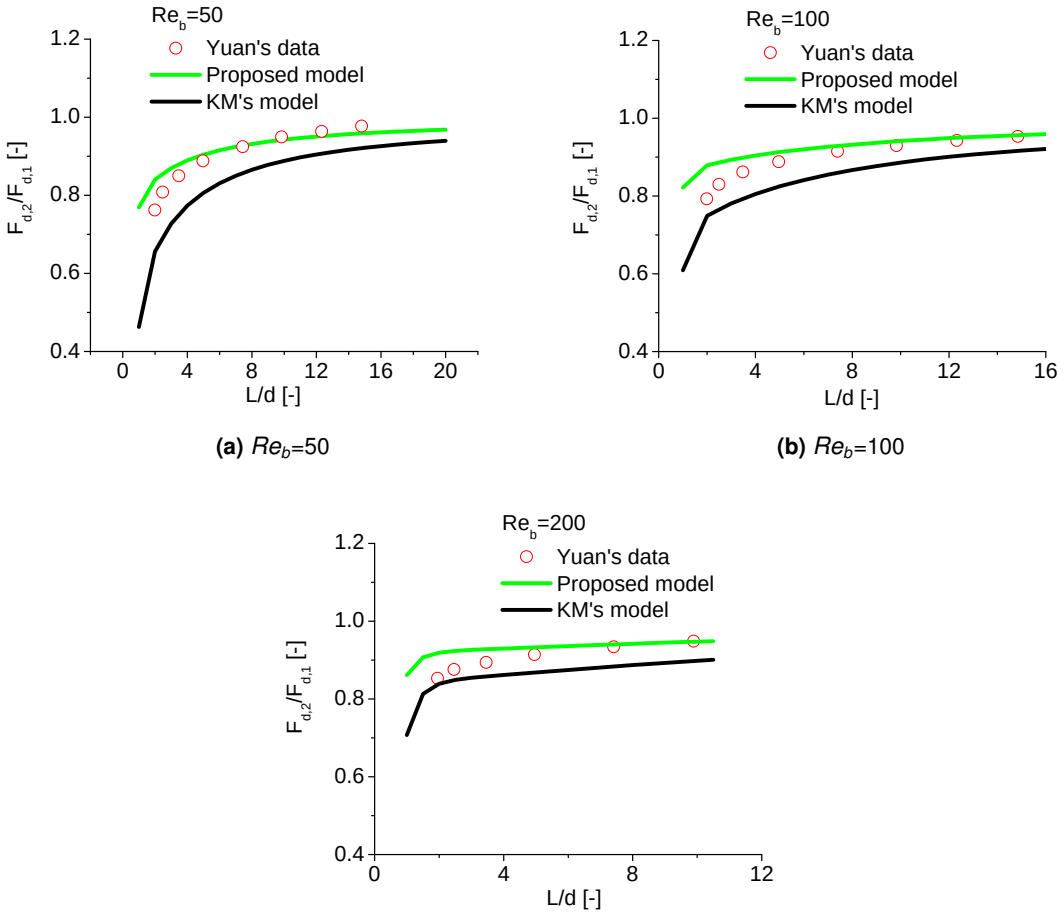

(a) Re_b=50 **(b)** Re_b=100

(c) Re_b=200

Fig. 4.2: Drag force ratio between the affected bubble and a corresponding single one with relations to L/d predicted by the proposed model and compared with DNS results provided by Yuan and Prosperetti [98]

by each bubble found by Lamb [39] can be obtained as:

$$F_{HDI} = \rho_L V_T^2 \pi d^2 \left(1 + C_{vm}\right) \left(\frac{d}{L}\right)^4 \tag{4.6}$$

where, C_{vm} is the virtual mass coefficient and its value for a spherical body is equal to 0.5. It can be observed that the repulsive force is only dependent on the vertical distance between two bubbles. The equilibrium distance L_e is reached when the inviscid repulsion pairwise interaction force $2F_{HDI}$ is equal to the drag force difference between two bubbles $F_{d,1} - F_{d,2}$ as discussed by Ruzicka [68], shown as:

$$\frac{2F_{HDI}}{F_{d,1} - F_{d,2}} = 1 \tag{4.7}$$

The relative strength of this ratio between two bubbles is shown in Fig. 4.3 for Re_b =50, 100 and 200. It follows that the inviscid component of the inter-bubble interaction force is a short-range repulsive force and does not depend on Re_b. The equality of these forces determines the value of the stable equilibrium distance L_e and depends on the Re_b. The equilibrium distance increases as Re_b increases.

Yuan and Prosperetti [98] also proposed a correlation to approximately evaluate the computed equilibrium distances L_{eq} for Re_b = 50, 100 and 200. The three results lie remarkably

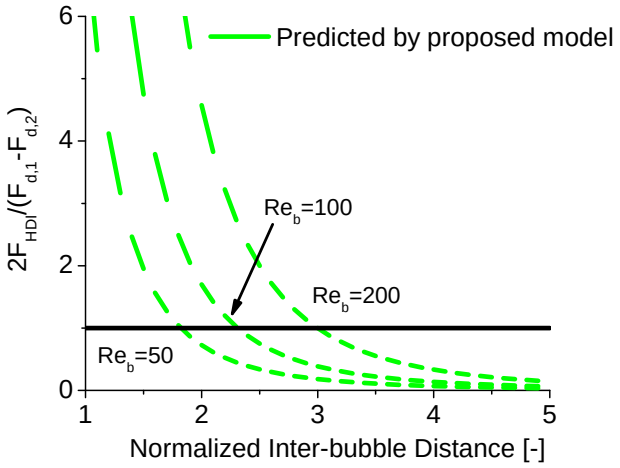

Fig. 4.3: Relative strength of the inviscid and wake attraction forces: $2F_{HDI}/(F_{d1} - F_{d2})$)

close to the line:

$$D_e = \frac{L_{eq}}{d} = 2.2 \log \mathrm{Re_b} - 2.19 \tag{4.8}$$

The values of the equilibrium distance predicted by the proposed drag force model for Re_b of 50, 100 and 200 are plotted in Fig. 4.4 and compared with the results by Yuan. From this figure, it is shown that the parameter dependence of the steady equilibrium distance predicted by the proposed model agrees well with Yuan's results. The small discrepancy can be attributed to the neglecting of the wake effect on the leading bubble. In Yuan's simulation, an increased drag force of the leading bubble is observed when the vertical distance between bubble L/d is quite small. Moreover, the inaccurate prediction of wake velocity in the near-wake region may also lead to the overestimation of equilibrium distance, especially when non-dimensional inter-bubble distance L/d is smaller than 3 as discussed before.

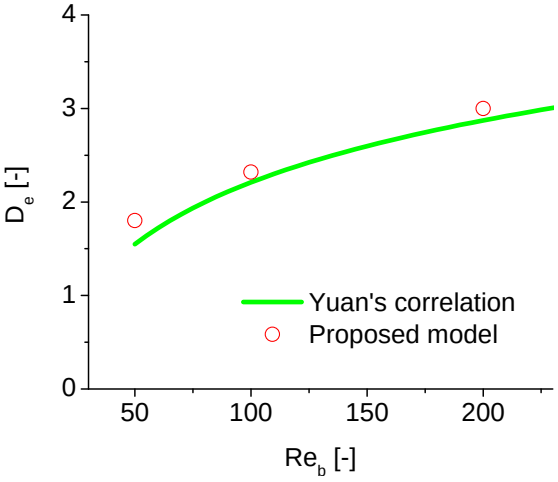

Fig. 4.4: Equilibrium distance as a function of Re_b for Re_b = 50, 100 and 200

To sum up, the proposed drag force model which models the relationship between the increased bubble rising velocity and the wake velocity, has a good performance when Re_b ranges from 3 to 200 and the non-dimensional vertical distance between bubbles L/d is larger than 2. However, the proposed drag force model also provides a slight underestimation of the

wake acceleration effect in the near wake region. This discrepancy is attributed to the poor prediction accuracy of wake velocity in the near wake region. If the value of wake velocity is predicted more accurately in this region, further improvements of prediction accuracy of the proposed model can be expected.

4.2 Bubble pairs at high bubble Reynolds number

To examine the performance of the proposed drag force model under high Re_b condition, the experiment conducted by Tsuge and Hibino [91] is chosen for purposes of validation. The wake acceleration effect on large diameter bubbles were studied in the experiment and his work was also reproduced by Celata et al. [14]. In the experiment, air bubbles have a diameter ranging from 5 to 9 mm. Single bubbles or bubble chains with variable (imposed) frequency were generated, and it is clearly illustrated that the rising velocities of the investigated bubbles were increased by the wake of the bubble preceding it because of the short distance between two adjacent bubbles. In the post processing of experimental data, the bubble rising velocity $V_{T,2}$ normalized against the single bubble rising velocity $V_{T,1}$ is plotted against the vertical distance between two adjacent bubbles normalized against the equivalent bubble diameter L/d. The wake effect is definitely obvious for such large bubbles, being remarkable even for large distances between two adjacent bubbles.

The predicted values of the proposed drag force model with the wake velocity profile obtained in the simulation are compared with experimental data and shown in Fig. 4.5. From these figures, it is clearly seen that the proposed model is capable of predicting the general trend of the increased bubble rising velocity. The ratio of $V_{T,2}/V_{T,1}$ increases as the vertical distance between bubbles decreases and is always greater than the terminal velocity of a corresponding single one due to the wake acceleration effect. The best agreement is achieved when bubble diameter is equal to 5 mm. It is shown that the predicted values of the proposed model are in excellent agreement with experimental data when the non-dimensional distance is smaller than 8. However, the discrepancy between the proposed drag force model and the measured data becomes evident as bubble diameter increases. It can be observed that, when bubble diameter is equal to 7 cm, the proposed model underestimates the increased bubble rising velocity in comparison with the test data. The discrepancy improves with a decreasing vertical distance between adjacent bubbles. Although the prediction accuracy is not quite promising when L/d is larger than 8, the proposed model predicts the increased bubble rising velocity with an acceptable accuracy when L/d is smaller than 8.

The underestimated bubble rising velocity is attributed to the wake velocity profile estimated by the proposed correlations. In the current study, the height of the simulation domain is limited to $14d$ due to the limitation of computational resource. In this case, the wake length which is investigated in our analysis is even smaller. In order to avoid the influence from the existence of boundary, its value is set to $8d$. For this reason, the proposed correlations of wake velocity profile may be not accurate in the region which is not covered by the simulation. Besides, the assumption that turbulent viscosity is a constant may also underestimate the value of wake velocity when L/d is large. At last, the deformed bubble shape caused by the wake affect may also lead to some unknown effect on the wake acceleration effect.

4.3 Conclusion and discussion

In this chapter, the drag force model which correlates the increased bubble rising velocity with the wake velocity is validated against the experimental and simulation results of interactive

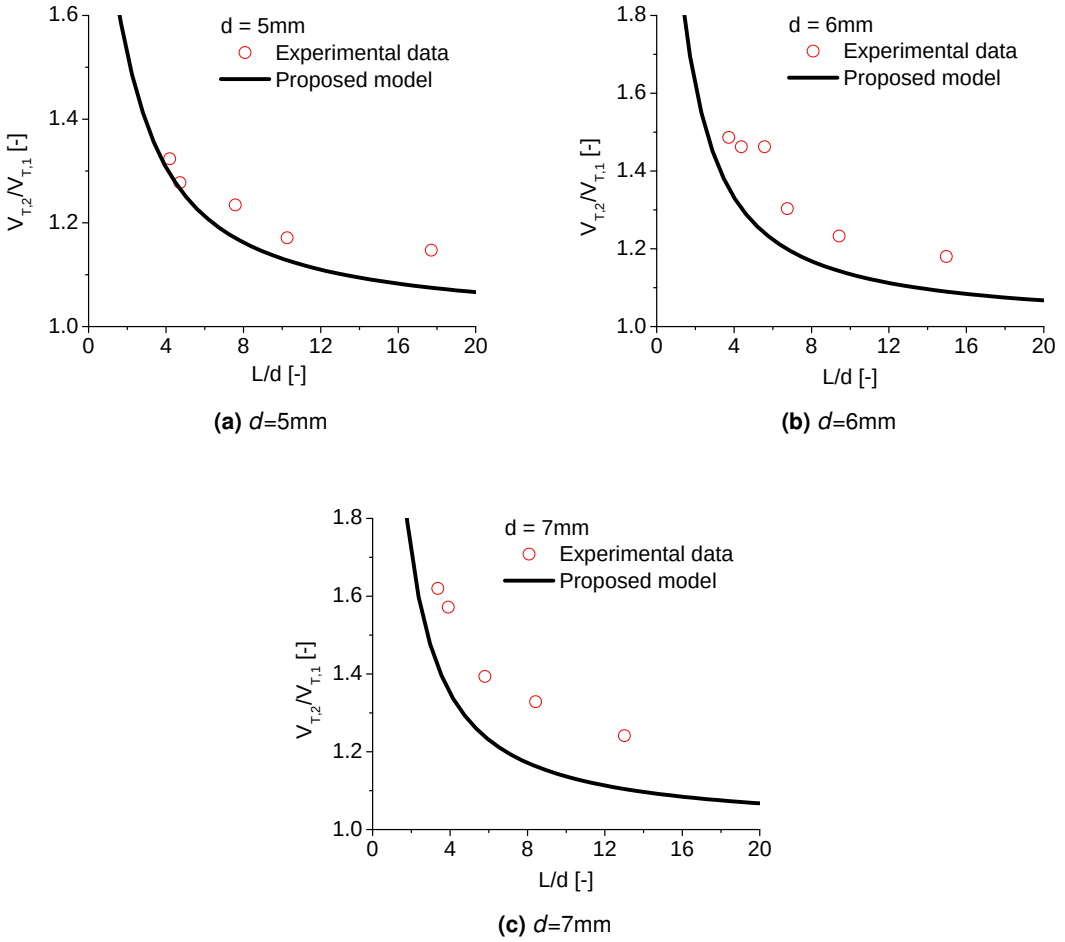

Fig. 4.5: Velocity ratio between the affected bubble and a corresponding single one with relations to L/d predicted by the proposed model and compared with the experimental data provided by Tsuge and Hibino [91]

bubbles which are aligned in line vertically. The investigated Re_b varies over a wide range. The most important conclusions are summarized here:

- Under low Re_b condition, the expression which is derived based on laminar boundary layer theory is employed to estimate the wake velocity profile and shows a good performance in the validation processes, especially in the far wake region. However, a slight underestimation of the wake acceleration effect is still found in the near wake region. Further improvement of prediction accuracy can be expected with a more accurate expression of wake velocity.
- When bubble diameter is large, the proposed correlations of wake velocity are employed to estimate the wake velocity profile. Generally, a good agreement is achieved. However, discrepancies arise when vertical distance between bubble is large. It is attributed to the underestimation of wake velocity in the far wake region and needs further investigations.

5. Application of the proposed drag force model for simulation of bubbly flow

The hydrodynamic behaviors of multi bubbles in bubbly flow generally differ from that of bubble pairs in the stagnant water. In this chapter, the proposed drag force model is employed to predict flow properties of bubbly flow and compared with the existing drag force models. Firstly, a brief introduction of computational methodology which includes two-fluid model and different BIT models is provided. After that, the flow properties of bubbly flow are predicted while the superficial velocities of both phases vary. The predicted values of the proposed drag force model are summarized and compared with experimental data. Subsequently, the proposed drag force model is employed to predict the enhanced turbulence caused by the dispersed bubbles. Finally, different modeling approaches of bubble induced turbulence are also assessed by comparing the predicted values of turbulent kinetic energy.

5.1 Computational methodology

The following section presents a brief description of two-fluid model, with the turbulence model to predict the turbulent properties in the flow field. The method to estimate the vertical distance between neighboring bubbles are also included.

5.1.1 Two-fluid model

Two-fluid model is a widely used approach to model two phase flow with significant volume fractions of both phases. The following section presents a brief description of two-phase flow modeling with the two-fluid model in OpenFOAM. Two-fluid methodology is applicable to all flow regimes including separated, dispersed or intermediate regimes. In this approach, both phases are still treated as continuum which interpenetrates each other in the whole simulation domain. The governing equations of mass and momentum are written for each phase separately and weighted by the corresponding volume fraction which represents the ensemble averaged probability of occurrence for each phase at a certain point in time and space. The information of the small length scales related to the interactions between two phases at the interface are lost when the ensemble averaging process is applied to the governing equations and the results of the large length scales are calculated directly. Hence, additional constitutive relations are needed in the governing equations to describe the exchanges of mass, momentum and energy due to the small scale structures at the interface with the purpose of obtaining a closed model.

Governing equations

For adiabatic incompressible flow, the continuity equation of the two-fluid model for flows with no interfacial mass transfer is written as (Ishii and Hibiki [31]):

$$\frac{\partial}{\partial t}\left(\rho_k \alpha_k\right) + \nabla \cdot \left(\rho_k \overline{u_k} \alpha_k\right) = 0 \tag{5.1}$$

where α is the volume fraction, ρ is the constant density of each phase and $\overline{u_k}$ is the mean velocity. The subscript $k = l$ or g denotes the liquid or gas phase.

If neglecting the break-up and coalescence of bubbles, the momentum equation of the phase k is written as follows:

$$\frac{\partial}{\partial t}\left(\rho_k \alpha_k \overline{u_k}\right) + \nabla \cdot \left(\rho_k \alpha_k \overline{u_k}\,\overline{u_k}\right) = -\alpha_k \nabla P_k + \alpha_k \rho_k \mathbf{g} + M_k + \nabla \cdot \left(\alpha_k \left(T_k + T_k^{\mathrm{Re}}\right)\right) \tag{5.2}$$

where P_k, $\mathbf{g}$ and T_k are the mean pressure, the gravitational acceleration and the laminar viscous shear, respectively. T_k^{Re} is the Reynolds stress and M_k is the averaged inter-phase momentum transfer term. The last two terms arise from the averaging process and require further modeling which will be discussed later.

In general, each phase has its own velocity, temperature and physical properties. The pressure in every control volume is assumed to be the same for each phase, so that the pressure difference between gas and liquid phases is neglected in two-fluid model. In case of bubbly flow, this assumption is justified as long as the surface tension has a minor impact on the flow behavior. However, it is found that the drag force acting on a large diameter bubble is governed by the surface tension force so that the modeling of interfacial momentum transfer has to be examined closely.

Inter-phase momentum transfer

As discussed before, the information about the small length scales at the interface is lost during the averaging process. In order to close the modeling, the averaged inter-phase momentum transfer term M_k in Eq. 5.2 has to be estimated for each phase. Usually, it is decomposed into several parts in which different effects from the liquid on the dispersed bubbles are considered. The study of the inter-phase momentum transfer term is widely carried out by a lot of researchers and a review of relevant models can be found in Zhang et al. [99]. Here, only some fundamental models will be stated in the following section and implemented in the two-fluid solver.

The inter-phase momentum transfer term can be naturally decomposed into elemental components depending on their different origins. It is shown as:

$$M_k = F_k^{drag} + F_k^{lift} + F_k^{vm} + F_k^{wall} + F_k^{td} \tag{5.3}$$

where F_k^{drag}, F_k^{lift}, F_k^{vm}, F_k^{wall} and F_k^{td} stand for the drag force, the lift force, the virtual mass force, the wall lubrication force and the turbulent dispersion force, respectively.

The drag force reflects the resistance opposing bubble motion relative to the surrounding liquid. The corresponding liquid-phase momentum source is given by:

$$F_l^{drag} = -F_g^{drag} = \frac{3}{4d}\alpha_g C_d \rho_l \left|\mathbf{U}_r\right| \mathbf{U}_r \tag{5.4}$$

Here, $\mathbf{U}_r$ denotes the relative velocity between two phases.

For the purpose of comparison, Tomiyama model and Schiller-Naumann model are also employed in the current study. Tomiyama model [87] is widely used to predict he drag force coefficient of a single bubble. It is validated in Re_b range of 10^{-2} to 10^3. Experimental data also proved that it produced a good result of bubble terminal velocity when the investigated air bubbles rose in the cylindrical column. In many CFD simulation of two phase flow, interfacial forces between the continuous and the dispersed phases are modeled by using Schiller-Naumann model [77] which is only dependent on bubble Reynolds number. Their expressions are summarized in Tab. 2.1 and Tab. 2.2.

In the experiment conducted by Serizawa et al. [80], the pipe diameter is not quite large. In this case, it is found that the effect from the existence of wall should be taken into consideration due to the large velocity gradient in the near wall region. Legendre and Magnaudet [41] pointed out that the present of liquid velocity gradient increases the drag force acting on a bubble and proposed the following drag multiplier ϕ_{sr}:

$$\phi_{sr} = 1 + 0.55Sr^2 \tag{5.5}$$

where Sr is the non-dimensional shear rate defined by:

$$Sr = \frac{d\omega}{\mathbf{U}_r} \tag{5.6}$$

where ω is the magnitude of the liquid velocity gradient. Hence, the drag coefficient is modified to:

$$C_{dm} = C_d(1 + 0.55Sr^2) \tag{5.7}$$

Eq. 5.7 was employed in the simulation of Hosokawa and Tomiyama [30] and a good agreement was achieved in comparison with experimental data. Hence, it is adopted in our simulation.

If a bubble moves in an unbounded shear flow, the non-uniform velocity field around bubble leads to an asymmetrical distribution of velocity field, which causes an asymmetrical local pressure distribution at the bubble interface. This results in a net force acting on the bubble which is perpendicular to the motion of the bubble relative to the liquid. Therefore, it is summarized as a net lift force, and the lift force related on the unit volume is calculated by Auton [4]:

$$F_l^{lift} = -F_g^{lift} = C_l\alpha_g\rho_l\mathbf{U}_r \times \nabla \times \mathbf{U}_l \tag{5.8}$$

where C_l denotes the lift force coefficient.

Virtual mass force arises when a relative acceleration between two phases exists. It is calculated as:

$$F_l^{vm} = -F_g^{vm} = \alpha_l C_{vm}\rho_l\left(\frac{D\overline{u_g}}{Dt} - \frac{D\overline{u_g}}{Dt}\right) \tag{5.9}$$

where D/Dt stands for the material time derivative. The coefficient C_{vm} is usually set to a constant 0.5 based on the potential flow analysis about a single spherical bubble. When the steady state is reached, this force vanishes.

The turbulent dispersion force describes the effect of the turbulent fluctuations of liquid velocity on the dispersed bubbles. Burns et al. [13] derived an explicit expression by Favre averaging the drag force as:

$$F_l^{disp} = -F_g^{disp} = \frac{3}{4}C_d\rho_l\frac{\alpha}{d}|\mathbf{U}_r|\frac{\nu_l^{turb}}{\sigma_{TD}}\left(\frac{1}{\alpha_g} + \frac{1}{1-\alpha_g}\right)\nabla\alpha_g \tag{5.10}$$

with ν_l^{turb} and $\sigma_{t,l}$ stand for the turbulent viscosity of the continuous liquid phase and the turbulent Schmidt number. The value of $\sigma_{t,l}$ is usually taken as 0.9. From Eq. 5.10, it can be observed that the turbulent dispersion force is dependent on the predicted drag force, the turbulent properties and the distribution of volume fraction. Due to the gradient term of volume fraction, turbulent dispersion force acts in the opposite direction of lift force and hence attempts to force bubbles to move from regions of high volume fraction to regions of low volume fraction.

The gas fraction distribution in the near wall region, which is important for the general flow structure in case of pipe flow, is mainly determined by the balance between the lift force and the wall lubrication force. Antal et al. [3] proposed a wall lubrication force model according to:

$$F_l^{wall} = -\alpha_l \rho_l C_{wl} \left|\mathbf{U}_r^2\right| n_w \tag{5.11}$$

where C_{wl} is a function that has dimension of inverse length and dependent on the distance to the wall y_w. n_w is the unit normal vector perpendicular to the wall pointing into the fluid. In Antal's model, a simple correlation is used to calculate the coefficient C_{wl} as:

$$C_{wl} = \max\left\{\frac{C_{w1}}{d} + \frac{C_{w2}}{y_w}, 0\right\} \tag{5.12}$$

The coefficients are chosen so that C_{w1} is negative and the force vanishes for $y_w/d > -C_{w2}/C_{w1}$ which is usually a few bubble diameters away from the wall. Recommended values for turbulent flow conditions are (Troshko and Hassan [90]):

$$C_{W1} = -0.02 \qquad C_{W2} = 0.06 \tag{5.13}$$

Generally, drag, lift, wall and turbulent dispersion forces are considered in the simulation of bubbly flow. Among these forces, the determination of lift force coefficient is dependent on the profile of volume fraction observed in the experiment. If a wall-peaking profile of volume fraction is found in the experiment, its value is set to be positive. Correspondingly, when a core-peaking profile of volume fraction is observed, a negative value of lift force coefficient is expected sot that the lift force acting in the direction of pushing bubble towards the pipe center. In this case, the wall lubrication force which is artificially introduced to push bubbles away from the wall is not required anymore. For this reason, the wall lubrication force is neglected in the simulation of experiment conducted by Shawkat et al. [81] in which core-peaking profiles of volume fraction are observed in all cases. Hence, in the radial direction, only the lift force and the turbulent dispersion force are included in the momentum equation.

5.1.2 Turbulence modeling

Standard k-ϵ model

The Reynolds stress term T_k^{Re} in the momentum equation Eq. 5.2 still has to be modeled. In the standard k-ϵ model, the enhanced turbulence caused by the dispersed bubble is not considered. Usually the turbulence in the gas phase is neglected and only the velocity fluctuation of liquid phase is considered in the simulation. Hence, the Reynolds stress in the liquid phase can be expressed as:

$$T_l^{\mathrm{Re}} = \rho_l \left(\nu_l^{turb}\left(\nabla \overline{u_l} + \left(\nabla \overline{u_l}\right)^T - \frac{2}{3} I \left(\nabla \cdot \overline{u_l}\right)\right) - \frac{2}{3} I k_l\right) \tag{5.14}$$

where k_l is the turbulence kinetic energy of liquid phase and I is the identity tensor. It is shown that this term is quite similar to the single phase turbulence model.

The liquid turbulent kinetic energy k_l equation and turbulent dissipation ϵ_l equation can be derived from the momentum and continuity equations. They are reduced to a practically useful form and written as (Sokolichin and Eigenberger [84]):

$$\frac{\partial}{\partial t}\left(\alpha_l \rho_l k_l\right) + \nabla \cdot \left(\alpha_l \rho_l u_l k_l\right) = \nabla \cdot \left(\alpha_l \left(\mu_l^{mol} + \frac{\mu_l^{turb}}{\sigma_k}\right) \nabla k_l\right) + \alpha_l \left(T_l^{\mathrm{Re}} : \nabla u_l - \rho_l \epsilon_l\right) \tag{5.15}$$

$$\frac{\partial}{\partial t}\left(\alpha_l \rho_l \epsilon_l\right) + \nabla \cdot \left(\alpha_l \rho_l u_l \epsilon_l\right) = \nabla \cdot \left(\alpha_l \left(\mu_l^{mol} + \frac{\mu_l^{turb}}{\sigma_\epsilon}\right) \nabla \epsilon_l\right) + \alpha_l \frac{\epsilon_l}{k_l} \left(C_{\epsilon P} T_l^{\mathrm{Re}} : \nabla u_l - C_{\epsilon D} \rho_l \epsilon_l\right) \tag{5.16}$$

The two phase $k-\epsilon$ model is quite similar to the single phase $k-\epsilon$ model. Every term of single phase $k-\epsilon$ model is simple multiplied by the liquid volume fraction to yield the two phase model. The turbulent viscosity is evaluated from the standard formula:

$$\mu_l^{turb} = C_\mu \rho_l \frac{k_l^2}{\epsilon} \tag{5.17}$$

The effective viscosity is calculated by:

$$\mu_l^{eff} = \mu_l^{mol} + \mu_l^{turb} \tag{5.18}$$

where μ_l^{mol} is the laminar viscosity of liquid.

All turbulence model parameters take their usual single phase values and are summarized in the following table:

C_μ	$C_{\epsilon 1}$	$C_{\epsilon 2}$	σ_k	σ_ϵ
0.09	1.44	1.92	1.0	1.3

Tab. 5.1: Summary of parameters used in the two-phase $k-\epsilon$ turbulence model

The form of the $k-\epsilon$ model presented is valid only for the flow at high Reynolds number. It is evident that the mean velocity in the near-wall region is greatly damped due to the influence caused by the existence of wall where the no-slip boundary condition has to be satisfied. The viscous stress reduces the axial velocity when approaching the wall and leads to a high velocity gradient. Hence, the turbulence is rapidly augmented by the production of turbulent kinetic energy due to the large velocity gradient towards the outer part of the near-wall region [1].

In order to capture the large velocity gradient in the near wall region, a fine resolution of mesh is required which leads to a high demand on the computational power. And it significantly impacts the reliability and stability of numerical simulation. This problem is circumvented by using the law of wall which describes the flow in the near wall region accurately. Numerous experiments have shown that the near-wall region can subdivided into three layers. In the viscous sublayer, which is closest to the wall, the flow is almost laminar, and the viscous stress plays a dominant role in the momentum transfer. In the outer layer, where the viscous effect is negligible, the turbulence plays a more important role and the velocity profile obeys a logarithmic law named as logarithmic sublayer. Finally, a transition sublayer exists between

the viscous and logarithmic sublayer, where the viscous and turbulent effects are of equal importance.

In the usage of the law of wall, the first node is placed in the logarithmic sublayer. The viscous and transition layer is not resolved. Instead, semi-empirical formulas called “wall functions" are employed to bridge the viscosity-affected region near the wall and the fully-turbulent region. With this method, the viscous and transition layers in which the flow properties exhibit a large gradient are neglected in the simulation so that the demand on the computational efforts is considerably reduced. Following this line of thought, the governing equations of momentum and turbulence can be simplified in the near wall region. In the logarithmic sublayer, the molecular diffusion and the pressure gradient are small in comparison with the turbulent diffusion term. Furthermore, it is assumed that the turbulent kinetic energy is essentially constant. This approximation is very strong and is only valid in a small region near the wall. Hence, the momentum and $k-\epsilon$ equations are simplified to:

$$\frac{d}{dy}\left(\alpha_l \mu_l^{turb} \frac{du_{l,x}}{dy}\right) = 0 \tag{5.19}$$

$$-\frac{d}{dy}\left(\alpha_l \mu_l^{turb} \frac{dk_l}{dy}\right) + \alpha_l \mu_l^{turb}\left(\frac{du_{l,x}}{dy}\right)^2 - \alpha_l \epsilon_l = 0 \tag{5.20}$$

$$-\frac{d}{dy}\left(\frac{\alpha_l \mu_l^{turb}}{\sigma_\epsilon} \frac{d\epsilon_l}{dy}\right) + C_{\epsilon 1} \alpha_l \mu_l^{turb}\left(\frac{du_{l,x}}{dy}\right)^2 - \alpha_l C_{\epsilon 2} \frac{\epsilon_l^2}{k} = 0 \tag{5.21}$$

The solutions of Eq. 5.19, Eq. 5.20 and Eq. 5.21 are:

$$u_{l,x} = \frac{u_\tau}{\sqrt{\alpha_l}}\left(\frac{\ln y^+}{\kappa} + B\right) \tag{5.22}$$

$$k_l = \frac{u_\tau^2}{\alpha_l \sqrt{C_\mu}} \tag{5.23}$$

$$\epsilon_l = \frac{u_\tau^3}{\alpha_l^{3/2} \kappa y_w} \tag{5.24}$$

where:

$$y^+ = \frac{y_w u_\tau \rho_l}{\mu_l} \tag{5.25}$$

$$u_\tau = \sqrt{\frac{\tau_w}{\rho_l}} \tag{5.26}$$

Here, y denotes the distance from the wall, $u_{l,x}$ stands for the liquid velocity parallel to the flow direction, κ is the von Karman constant taken the value of 0.41, and B is an empirical constant and equal to 5.5. From Eq. 5.22 to Eq. 5.24, the boundary conditions for momentum and $k-\epsilon$ equations in the near-wall region are summarized. The advantage of this approach lies in its economy, robustness and a reasonable prediction of concerned parameters.

Modeling approaches of bubble induced turbulence

In section 5.1.2, the conservation equations of two-fluid model has been described in detail. The modeling approaches of inter-phase momentum transfer and Reynolds stress T_l^{Re} are also included. However, the additional turbulence due to the existence of bubbles is not included in the modeling of Reynolds stress term T_l^{Re}. Concerning the enhanced turbulence in bubbly flow, we still adopt a two-equation turbulence model for liquid phase in which additional source terms are introduced to describe the additional turbulence caused by the relative motions between bubbles and liquid phase. Usually, additional source terms are introduced into both k and ϵ equations to account for the turbulence energy production and dissipation caused by the existence of bubbles. The modified governing equations of liquid turbulent kinetic energy k_l and turbulent dissipation ϵ_l have been derived and modified to the following form as (Rzehak and Krepper [70]):

$$\begin{aligned}\frac{\partial}{\partial t}\left(\alpha_l\rho_l k_l\right)+\nabla\cdot\left(\alpha_l\rho_l u_l k_l\right)=\\ \nabla\cdot\left(\alpha_l\left(\mu_l^{mol}+\frac{\mu_l^{turb}}{\sigma_k}\right)\nabla k_l\right)+\alpha_l\left(T_l^{\mathrm{Re}}:\nabla u_l-\rho_l\epsilon_l\right)+S_l^k\end{aligned} \tag{5.27}$$

$$\begin{aligned}\frac{\partial}{\partial t}\left(\alpha_l\rho_l \epsilon_l\right)+\nabla\cdot\left(\alpha_l\rho_l u_l \epsilon_l\right)=\\ \nabla\cdot\left(\alpha_l\left(\mu_l^{mol}+\frac{\mu_l^{turb}}{\sigma_\epsilon}\right)\nabla \epsilon_l\right)+\alpha_l\frac{\epsilon_l}{k_l}\left(C_{\epsilon P}T_l^{\mathrm{Re}}:\nabla u_l-C_{\epsilon D}\rho_l\epsilon_l\right)+S_l^\epsilon\end{aligned} \tag{5.28}$$

Eq. 5.27 and Eq. 5.28 are quite similar to the k_l and ϵ_l equations employed in the previous chapter. Every term in Eq. 5.15 and Eq. 5.16 are still kept. In order to modeling bubble induced turbulence, two additional source terms S_l^k and S_l^ϵ are introduced into k_l and ϵ_l equations, respectively. Source term S_l^k describes the turbulence production caused by the relative motions between bubbles and liquid phase. A plausible approximation is provided by the assumption that all energy lost by the bubble due to drag is converted to turbulent kinetic energy in the wake of bubble. Hence, this term is evaluated by:

$$S_l^k = |F_l^{drag}|\cdot|\mathbf{U}_r| \tag{5.29}$$

For the source term in the ϵ equation S_l^ϵ, S_l^k is divided by a time scale τ and multiplied by a constant $C_{\epsilon B}$. It yields:

$$S_l^\epsilon = C_{\epsilon B}\frac{S_l^k}{\tau_t} \tag{5.30}$$

The decision of the time scale relevant to bubble induced turbulence is widely discussed in the literature. The employed models for the source term S_l^ϵ are summarized in Tab. 5.2. The references in which they have been investigated for bubbly flow in pipe are also listed. The coefficient $C_{\epsilon B}$ has to be determined by comparison to the data. In the simulation the values recommended by the respective authors have been used for the presently investigated tests.

Since the bubble induced turbulence is included in k_l and ϵ_l equation due to the respective source terms, the standard formula is also employed to evaluate the turbulent viscosity as shown in Eq. 5.17. All turbulence model parameters also take their usual single phase values as summarized in Tab. 5.1.

Reference	Morel [52]	Troshko and Hassan [90]	Rzehak and Krepper [70]
τ_t	$\propto (d^2/\epsilon_l)^{1/3}$	$\propto d/\mathbf{U}_r$	$\propto d/\sqrt{k_l}$
$C_{\epsilon B}$	2.0	0.45	2.0

Tab. 5.2: Summary of time scale models considered in the following study

5.1.3 Vertical distance between neighboring bubbles

As summarized in chapter 3.5.4, the vertical distance between neighboring bubbles is required to estimate the required averaged wake velocity $\overline{U}_w$, as shown in Eq. 3.68 and Eq. 3.69. However, information about the vertical distance between neighboring bubbles is quite limited in the studies of bubbly flow. To employ the proposed model in the prediction of bubbly flow, if neglecting the lateral interactions between neighboring bubbles, the relative position between neighboring bubbles can be simplified to bubbles aligned in line vertically, as shown in Fig. 5.1. The second bubble is continuously affected by the wake generated by the first one. Hence, it is required to approximately estimate the value of L in the simulation of bubbly flow. However, due to the complex nature of bubbly flow, no information about this parameter is provided in the previous experimental studies of bubbly flow.

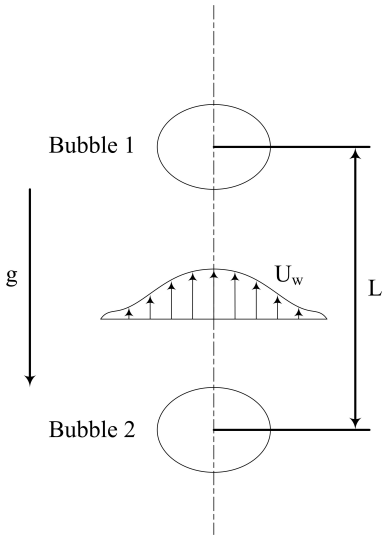

Fig. 5.1: Simplification of the relative position between neighboring bubbles in bubbly flow

In the current study, attempts are made to approximately evaluate the vertical distance between bubbles L for RANS simulation of bubbly flow. Recalling the time-averaged parameters employed in RANS simulation of bubbly flow, any quantities related to the estimation of drag force should be also time-averaged, such as the vertical distance between bubbles. Therefore, the time-averaged properties including volume fraction α and averaged bubble diameter $\bar{d}$ are chosen. There are several advantages of this consideration which are listed as follows: firstly, both of them are widely provided by lots of experimental studies and can be obtained easily; secondly, in RANS simulation, they are specified as the boundary condition of simulation domain and the uses of them are simple; thirdly, volume fraction is defined as the volume occupied by the gas divided by the total volume. The vertical distance can be obtained with volume fraction and averaged bubble diameter if the lateral distance between neighboring bubbles is known. The physical meaning of this idea is clear.

Until now, the vertical distance between bubbles is not even physically investigated in the previous studies of bubbly flow. Therefore, we have to pursue other alternatives. In the current study, appropriate assumptions are taken to approximate the lateral distance between

neighboring bubbles. In every small local region of bubbly flow, bubbles are assumed to have the same diameter and the change of lateral distance between bubbles during the evolution of time is neglected. As indicated in Fig. 5.2, the lateral distance between neighboring bubbles is assumed to be equal to their vertical distance. it is seen that the volume occupied by the bubble in this small local region is equal to the volume of a single bubble. In this case, the volume fraction α is defined as:

$$\alpha = \frac{\pi \overline{d}^3}{6L^3} \tag{5.31}$$

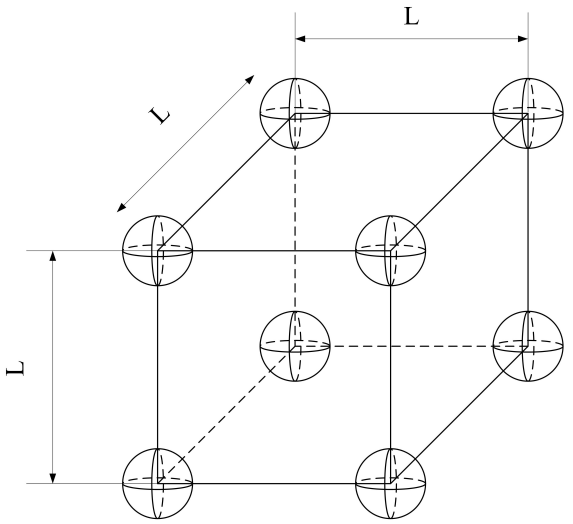

Fig. 5.2: A schematic description of the lateral distance between neighboring bubbles

And it yields:

$$L = \overline{d} \sqrt[3]{\frac{\pi}{6\alpha}} \tag{5.32}$$

where $\overline{d}$ denotes the averaged bubble diameter and it is calculated based on the bubble volume V as follows:

$$\overline{d} = \sqrt[3]{\frac{6V}{\pi}} \tag{5.33}$$

With this expression, the dependency of the vertical distance between bubbles L on the volume fraction α and averaged bubble diameter $\bar{d}$ is modeled. Then according to Eq. 3.66 and Eq. 3.69, the increased rising velocity of an affected bubble is estimated. The performance of Eq. 5.32 is shown in Fig. 5.3. It is illustrated that the vertical distance between bubbles decreases as volume fraction increases. And this effect is much stronger under low volume fraction condition.

The dependency of the reduced drag force coefficient on the volume fraction is shown in Fig. 5.4. Here, Tomiyama model is used to calculate the drag force coefficient of a single bubble. It is shown that the influence from volume fraction becomes smaller as volume fraction increases. This phenomenon is attributed to the dependency of L/d on volume fraction. When volume fraction is low, the variation of L/d is much larger, as shown in Fig. 5.3. As discussed before, assumptions used for an estimation of wake velocity are justified when L/d is larger than 2. In this case, volume fraction is smaller than 6.5%. Hence, the proposed drag force model is recommended for cases whose volume fraction is smaller than 6.5%. However, due to the limitation of experimental data, the performance of the proposed model is also examined when volume fraction is larger than this value.

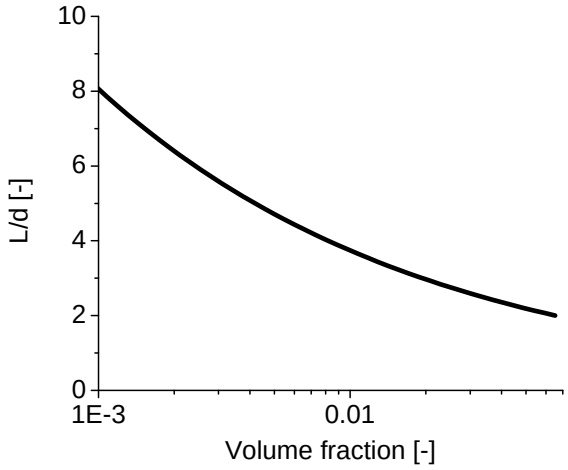

Fig. 5.3: Dependency of the dimensionless vertical distance between neighboring bubbles $L/\bar{d}$ on volume fraction

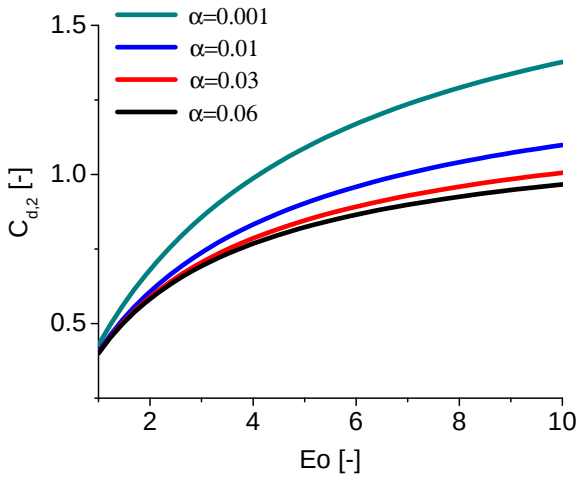

Fig. 5.4: Drag force coefficient of the affected bubble $C_{d,2}$ with relations to volume fraction α and Eo number predicted by the proposed drag force model

5.2 Description of selected experiments and numerical configurations

Due to the crucial importance of bubbly flow which is often encountered in many industrial processes, the main task of the current study is to propose a drag force model which improves the prediction accuracy of bubbly flow with consideration of the wake acceleration effect. For purposes of comparison, a thorough assessment of the proposed drag force model is quite necessary, and the employed experimental data should meet several requirements as discussed by Rzehak and Krepper [70]. Firstly, the measured values of relative velocity between gas and liquid phases should be included in the experiment, since this parameter is affected directly by the choice of drag force model. Secondly, the experimental data should contain quantities representing volume fraction, gas and liquid velocities, so that the modeling of other inter-phase momentum transfer terms can be compared independently. For an instance, a well predicted radial profile of volume fraction may prove the correctness of the calculated interfacial forces which is perpendicular to the motion of the bubble relative to the liquid. Thirdly,

information about the bubble size is also needed, since this parameter appears in all five components of interfacial momentum transfer term. Later on, it will be shown that the estimation of bubble induced turbulence is also dependent on the bubble diameter. Although only monodisperse method is employed in the current study, similar work can be found in Ničeno et al. [58]. The distribution of bubble diameter is not required in the simulation but still useful to judge the simplification used in the simulation. Finally, to ensure a broad range of validity of the assessment, a wide range of flow and geometric parameters should be covered in the simulation.

Experimental studies conducted by Serizawa et al. [80] and Shawkat et al. [81] which meet the requirements described above are selected in the current study. In all experiments, adiabatic, incompressible, air-water bubbly flows in vertical upward pipes of different diameters are studied at atmospheric pressure and room temperature. An overview of the major characteristics of each experiment chosen for the present work is given in Tab. 5.3 and Tab. 5.4 in which J_f and J_g denote the superficial velocities of liquid and gas phases, respectively. Overbar sign stands for the flow area average.

Name	Pipe diameter (mm)	$J_f(m/s)$	$J_g(m/s)$	$d(m)$	$\overline{\alpha}$	volume fraction profile
Sh1	200	0.20	-	-	-	-
Sh2	200	0.20	0.005	0.0043	0.013	Core peaking
Sh3	200	0.20	0.015	0.0044	0.036	Core peaking
Sh4	200	0.20	0.05	0.0050	0.083	Core peaking
Sh5	200	0.20	-	-	-	-
Sh6	200	0.26	0.015	0.0039	0.02	Core peaking
Sh7	200	0.26	0.05	0.0041	0.077	Core peaking
Sh8	200	0.26	0.085	0.0057	0.13	Core peaking

Tab. 5.3: Test cases from Shawkat et al. [81] selected for the present work

Name	Pipe diameter (mm)	$J_f(m/s)$	$J_g(m/s)$	$d(m)$	$\overline{\alpha}$	volume fraction profile
Se0	60	1.03	0	-	-	-
Se1	60	1.03	0.0753	0.004	0.0397	Wall peaking
Se2	60	1.03	0.151	0.004	0.1023	Wall peaking
Se3	60	1.03	0.302	0.004	0.1627	Wall peaking

Tab. 5.4: Test cases from Serizawa et al. [80] selected for the present work

Vertical up-flow of water and air in a round pipe with a large inner diameter D = 200 mm was conducted by Shawkat et al. [81] with varying liquid and gas mass fluxes. The investigated experiments were specially designed to show the liquid turbulence characteristics by using a dual optical probe and hot-film anemometry that volume fraction, liquid and gas velocities and velocity fluctuation at different liquid and gas superficial velocities can be measured. Liquid superficial J_f and gas superficial velocity J_g were varied in the investigation, corresponding to an area average void fraction α from 1.5% to 13%. Radial profiles of volume fraction, bubble size d, liquid velocity U_l, gas velocity U_g, axial liquid turbulence intensity u' and radial liquid turbulence intensity v' were measured at an axial position L/D = 42. For all selected tests, a core-peaking profile of volume fraction was observed.

Another study with some variations of gas mass fluxes in vertical upflow of water and air in a round pipe was carried out by Serizawa et al. [80]. Here, the pipe diameter D = 60 mm is rather small. Measurements were taken at axial positions L/D = 30. The instrument consisted of a double-sensor probe, a developed electronic circuit, a digital counter and a multichannel analyzer. A resistivity probe which required a sufficiently long time for sampling was developed

to measure the local void fraction based on the difference in electrical resistivity between the liquid and gas phases. Bubble velocity was detected by the velocity of displacement of the interface between the gas and the liquid. When a bubble hit two probes in succession, the distance between two probes and the time lag between two signals received by two probes were employed to estimate the bubble velocity. The liquid velocity and turbulent intensity were measured by the hot-film anemometer technique. Radial profiles of void fraction were given for all datasets. A wall-peak profile of volume fraction can be observed in all cases. Liquid velocity, axial turbulence intensity and Reynolds stress are given for many but not all of them. The bubble size was specified by a single value for each experiment.

All cases are simulated in 2D cylindrical geometry, i.e. a narrow cylindrical sector with wedge boundary condition imposed on the side boundaries, as indicated in Fig. 5.5. The radial size of simulation domain is enlarged for the sake of clearness. The boundary condition "wedge" is only for 2 dimensional axis-symmetric case and the geometry is specified as a wedge of small angle and one cell thick running along the plane of symmetry, straddling one of the coordinate planes. Equidistant spacing of griding points with $y^+ \approx 30$ is found suitable by a grid resolution study.

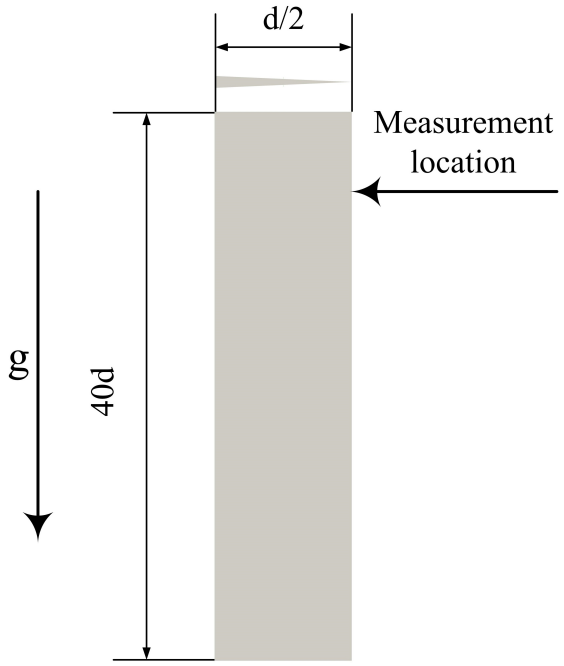

Fig. 5.5: Sketch of the simulation domain in the 2D computational domain

At the bottom of simulation domain, the inlet boundary conditions of liquid turbulent properties are specified according to a typical profile of single phase turbulent flow in a pipe. The values for k_l and ϵ_l are set using an estimated fluctuating component of velocity $\mathbf{u}_l'$ and a turbulent length scale l. k_l and ϵ_l are defined in terms of these parameters as follows:

$$k_l = \frac{1}{2}\overline{u_i' u_i'} \tag{5.34}$$

$$\epsilon_l = \frac{C_\mu^{0.75} k_l^{1.5}}{l} \tag{5.35}$$

The initial turbulence intensity is usually assumed to be equal to 5% and the turbulence length scale l is equal to 20% of the characteristic length of pipe. These form the initial inlet conditions for k_l and ϵ_l. Gas volume fraction and mass flux are set to uniform values at the

inlet. Precise conditions at the inlet do not have any influences as long as the axial distance to the measurement location is large enough for fully developed condition to be attained. In the simulation the axial length of simulation domain is 40 times of the characteristic length of the pipe.

Above the measurement location a flow abatement zone with a length of 10 times of the characteristic length of the pipe has been employed to ensure that there is no influence from the boundary conditions of outlet imposed at the top of the domain. A pressure boundary condition was set at the top. A no-slip condition is set on the wall for both the liquid and gas phases, with which the velocities of gas and liquid phases are neglected on the wall.

5.3 Prediction of flow properties of bubbly flow using the proposed drag force model

In this section, the proposed drag force model is implemented into two-fluid model and employed in RANS simulation of bubbly flow. The calculated values of the proposed model are compared with the experimental data and the existing drag force models. In the first section, the relative velocity between gas and liquid phases is calculated by the proposed drag force model, following by the analysis of the predicted turbulent kinetic energy. At last, the performance of different BIT models are analyzed.

5.3.1 Simulation and analysis of relative velocity

The proposed drag force is firstly compared with the experiment by Shawkat et al. [81], followed by the comparison against the experiment by Serizawa et al. [80].

Tests from Shawkat et al. [81]

The experimental data of Shawkat et al. [81] provide a variation of gas superficial velocity independent of liquid superficial velocity. Therefore, two series of tests have been selected for fixed values of liquid superficial velocity J_f = 0.20 or 0.26 m/s, but with different gas superficial velocities. Measured radial profiles of bubble diameter d for the selected test cases are shown in Fig. 5.6. From these profiles it is illustrated that the approximation of constant bubble diameter is well justified.

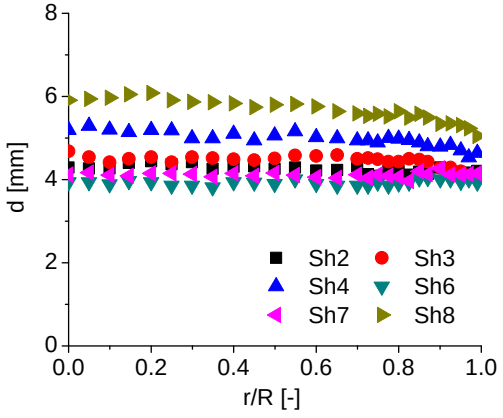

Fig. 5.6: Measured radial profiles of bubble diamter d for the selected cases from Shawkat et al. [81]

In the proposed drag force model, the increased bubble rising velocity is dependent on volume fraction, so that a well predicted volume fraction is very helpful to provide a good estimation of the relative velocity between gas and liquid phases when the wake acceleration effect is considered. Comparisons of calculated and measured volume fraction profiles are shown in Fig. 5.7. Overall, the calculated values obtained by Schiller-Naumann model are lowest in the four models while the highest value of volume fraction is provided by Tomiyama model. The results obtained by the proposed drag force model are in between them. Here, agreements of the radial profile of volume fraction provided by all three models are generally satisfying for all cases. However, the predicted values in Sh2 are not quite good in the near wall region as that in the pipe center. An underestimation of volume fraction is quite obvious. This discrepancy comes from an overestimation of lift force in the near wall region. As shown in Eq. 5.8, the value of lift force is proportional to velocity gradient. It is evident that the velocity gradient towards the wall is rapidly increased due to the existence of wall where no-slip boundary condition has to be satisfied. Consequently, the value of lift force which pushes bubbles away from the wall is overestimated. A smaller lift force coefficient in the near wall region is expected to reduce this discrepancy. In other cases (Sh3, Sh4, Sh7 and Sh8), a good agreement is found for the whole calculated profile. But signification deviations in the form of a too high value of volume fraction are observed in Sh6. As shown later, liquid and gas velocity profiles are in reasonable agreement but only for the volume fraction significant deviations occurred in Sh6. As discussed in Rzehak and Krepper [70], the source of these deviations ultimately has to be sought in the measurements and thus cannot be clarified here.

The relative velocity between gas and liquid phases directly assesses the performance of the employed drag force models. Comparisons of calculated and measured relative velocity profiles obtained in the study of Shawkat et al. [81] are plotted against the radial distance to the pipe center r and shown in Fig. 5.8. Overall, Schiller-Naumann model model which depends on Re_b predicts the highest values of relative velocity, while the predictions of Tomiyama model which depend on Eo number underestimate the relative velocity in all considered cases. For the proposed model, within the limits of expectation there is reasonable agreement between calculated and measured values for all considered cases. Among six tests, the proposed model here has an excellent performance in Sh7 and Sh8, and the predictions are much the same as the experimental data in the whole calculated profiles.

In spite of this, slight discrepancies are still found in other cases in which a more flattened profile of relative velocity is predicted with the drag force model. Especially in Sh2 and Sh6 whose averaged volume fraction is smallest in six tests, a good agreement is achieved in the pipe center but the predicted values in the near wall region are slightly overestimated. The discrepancies in these cases are not surprising since as discussed before, the increased rising velocity of the affected bubble is dependent on the vertical distance between neighboring bubbles L. An assumption that the distribution of bubbles in the axial direction is uniform is employed to calculate the value of L in terms of volume fractioin α and averaged bubble diameter $\bar{d}$. When volume fraction is low, this assumption may be not appropriate.

Tests from Serizawa et al. [80]

From the experimental data proposed by Serizawa et al. [80], a variation of gas superficial velocity independent of liquid superficial velocity was provided. In the simulation, three cases are chosen in which the value of liquid volumetric fluxes is fixed to 1.03 m/s and the gas superficial velocity varies from 0.0753 to 0.302 m/s. In three cases, the profiles of volume fraction are obvious wall-peaking in which bubbles tend to migrate to the near wall region.

The equivalent bubble diameter was obtained from bubble photographs with a planimeter. As shown in Fig. 5.9, although many corrugations of various shapes observed on the surface

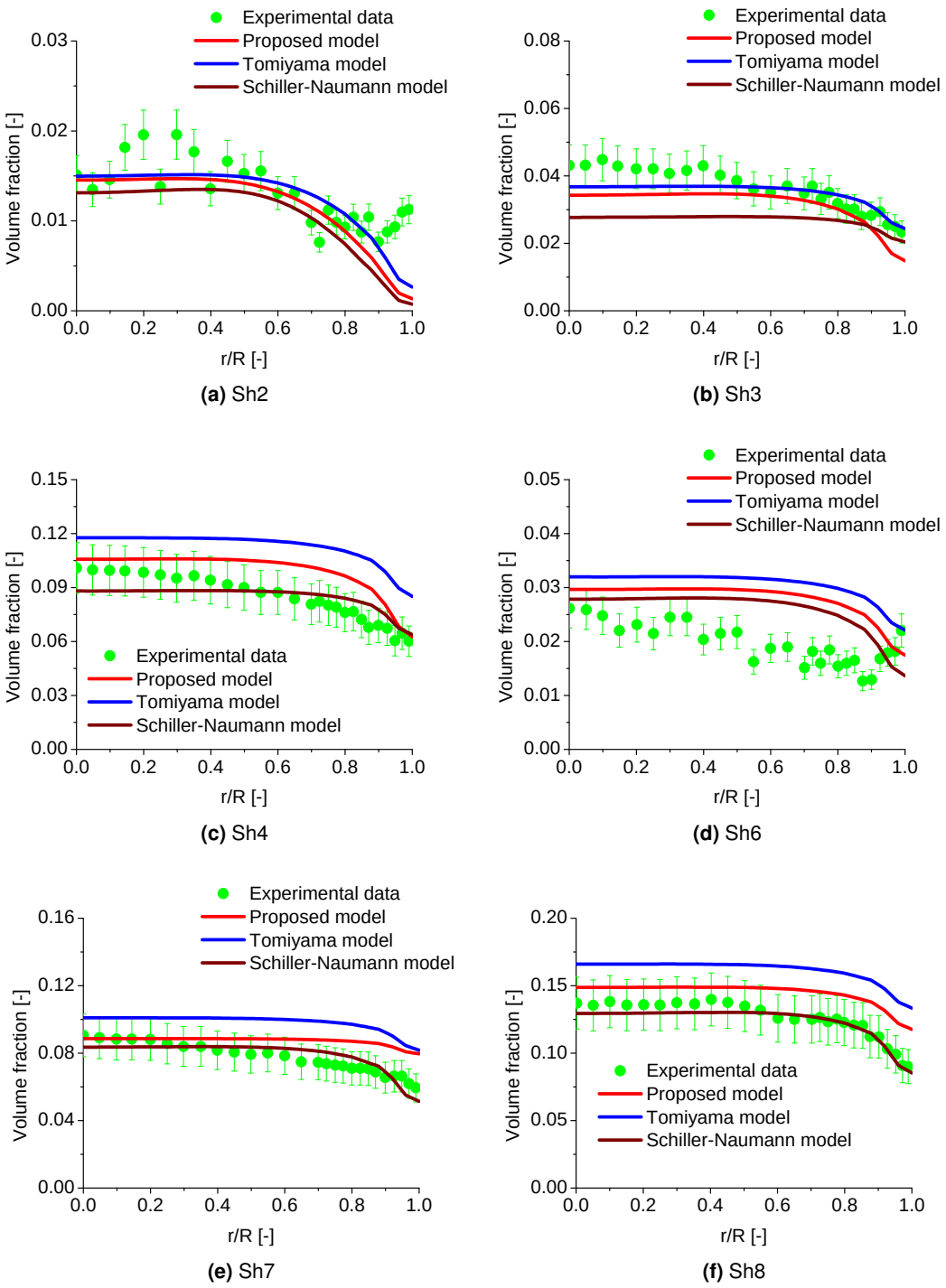

Fig. 5.7: Volume fraction profiles obtained with different drag force models and compared with the experimental data provided by Shawkat et al. [81]

of every bubble, the resulting bubble size distribution presented a uniform distribution in the radial direction [80]. The averaged bubble diameter over the flow area is used in the following simulation. In all simulations, the value of bubble diameter is taken as 4 mm, regardless of the gas superficial velocity.

Measured and calculated volume fraction profiles are compared in Fig. 5.10 for three cases. As for the simulation of Shawhat, agreements of the radial profile of volume fraction provided by all three models are generally satisfying for all cases. From these figures, it

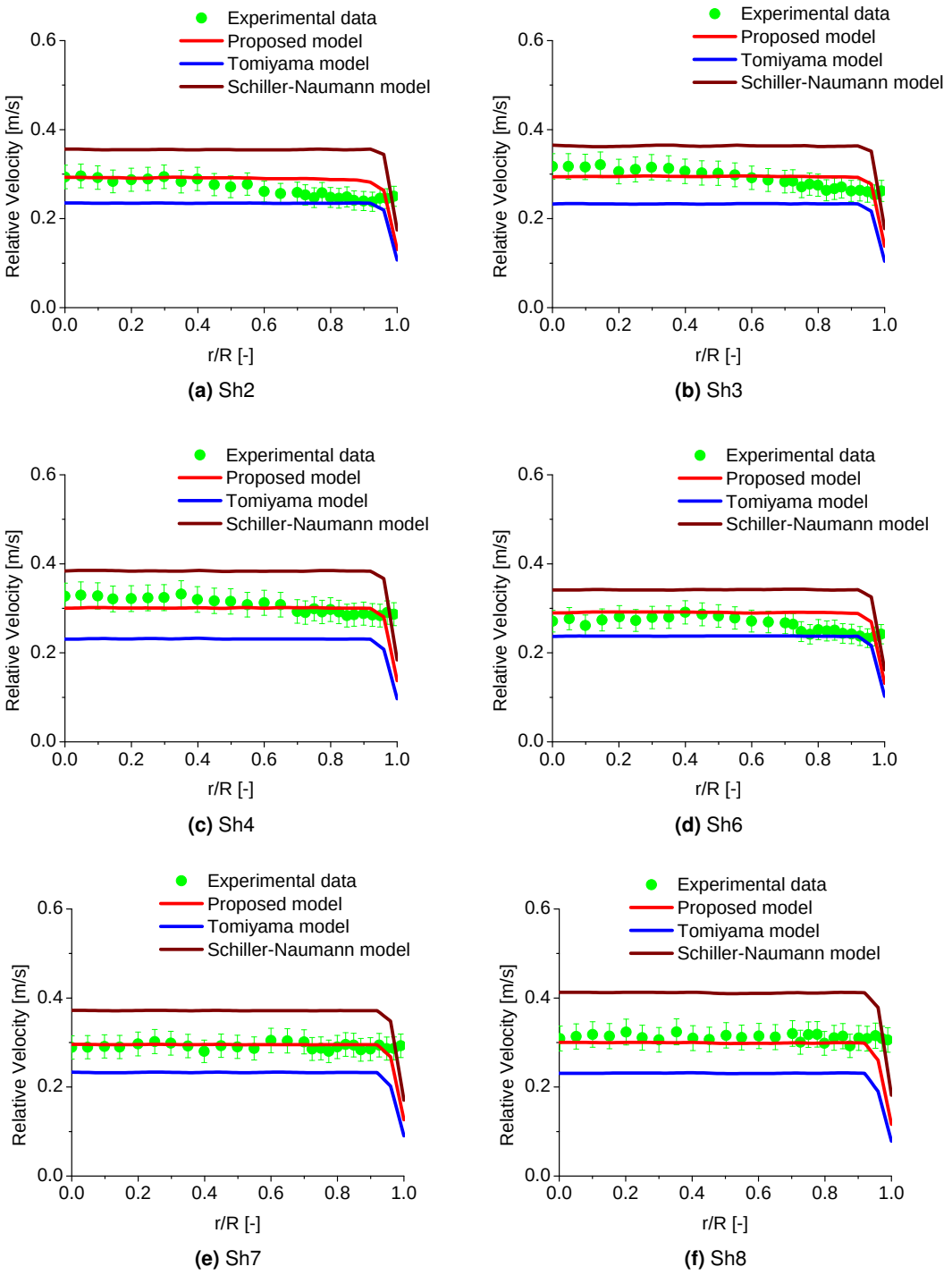

Fig. 5.8: Relative velocity profiles obtained with different drag force models and compared with the experimental data provided by Shawkat et al. [81]

is illustrated that the general trend of volume fraction profile that a dominant peak value exists in the near wall region is captured. However, deviations are still present and most prominent near the pipe center. It is shown that, in Se2 and Se3, the values of volume fraction are underestimated by all four models. They are most severe for Schiller-Naumann model with which volume fractions are greatly underestimated almost 4 % in the pipe center. For the other two models, the deviations persist for Se2 with a smaller difference. A similar tendency can be found in Se3 in which volume fraction tend to increase towards the pipe center and the smallest value of volume fraction can be found at $r/R = 0.8$. It is illustrated that the forces acting in

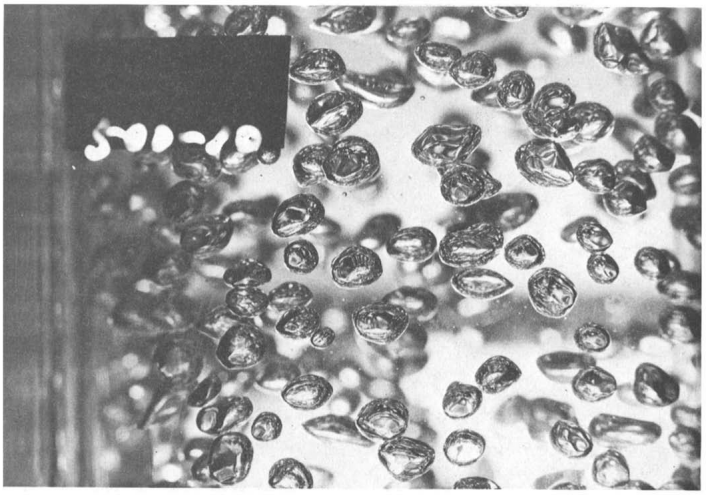

Fig. 5.9: Typical photograph taken from Serizawa et al. [80] to indicate the distribution of bubble diameter (Bubbly flow)

the transverse direction attempts to push bubbles to the near wall region when $r/R > 0.8$ and bubbles are forced to move to the pipe center when $r/R < 0.8$. A constant lift force coefficient is incapable to predict this phenomenon.

As shown in Fig. 5.11, significant differences between the various models are identified in the predicted profiles of relative velocity compared with experiment data. Relative to bubbly flow in a large diameter pipe, the profile of relative velocity varies much stronger in the radial direction. Although the model proposed by Legendre and Magnaudet [41] is employed to account for the influence from a large velocity gradient imposed on bubbles, especially in the near wall region, the predicted results provided by three drag force models still underestimate the variation of relative velocity in the radial direction. The predictions of Tomiyama model are smallest in all three models, while the calculated values by Schiller-Naumann model are highest. In three cases, the relative velocity calculated by the proposed model is in between the models selected from literature and its value is quite close to the averaged value of experimental data. Generally, the proposed model gives a best overall estimation of the relative velocity for all cases with acceptable errors when the relative velocity exhibits a strong variation in the radial direction.

5.3.2 Simulation and analysis of bubble induced turbulence

In the experimental studies of bubbly flow, the values of turbulent kinetic energy are not measured directly and an estimation thereof is derived from the measured turbulent intensity. Due to the fact that an anisotropic structure of turbulent exists in the wall-bounded flow, the components of the fluctuating velocity in axial, radial and azimuthal directions, u', v' and w', are different from each other. In the experiment conducted by Shawkat et al. [81], both axial and radial components of the fluctuating velocity are provided. From their study, the largest value of the ratio u'/v' is found in the near-wall region and it is also larger than that of single phase flow. It indicates that the turbulence in the bubbly flow is enhanced due to the relative motion of bubbles in the flow direction. However, data on the azimuthal component of the fluctuating velocity is not provided in the literature. By assuming that azimuthal and radial components of velocity fluctuation are equal, an estimation of $\sqrt{k}$ can be obtained as follows:

$$\sqrt{k} = \sqrt{\frac{1}{2}(u'u' + 2v'v')} \tag{5.36}$$

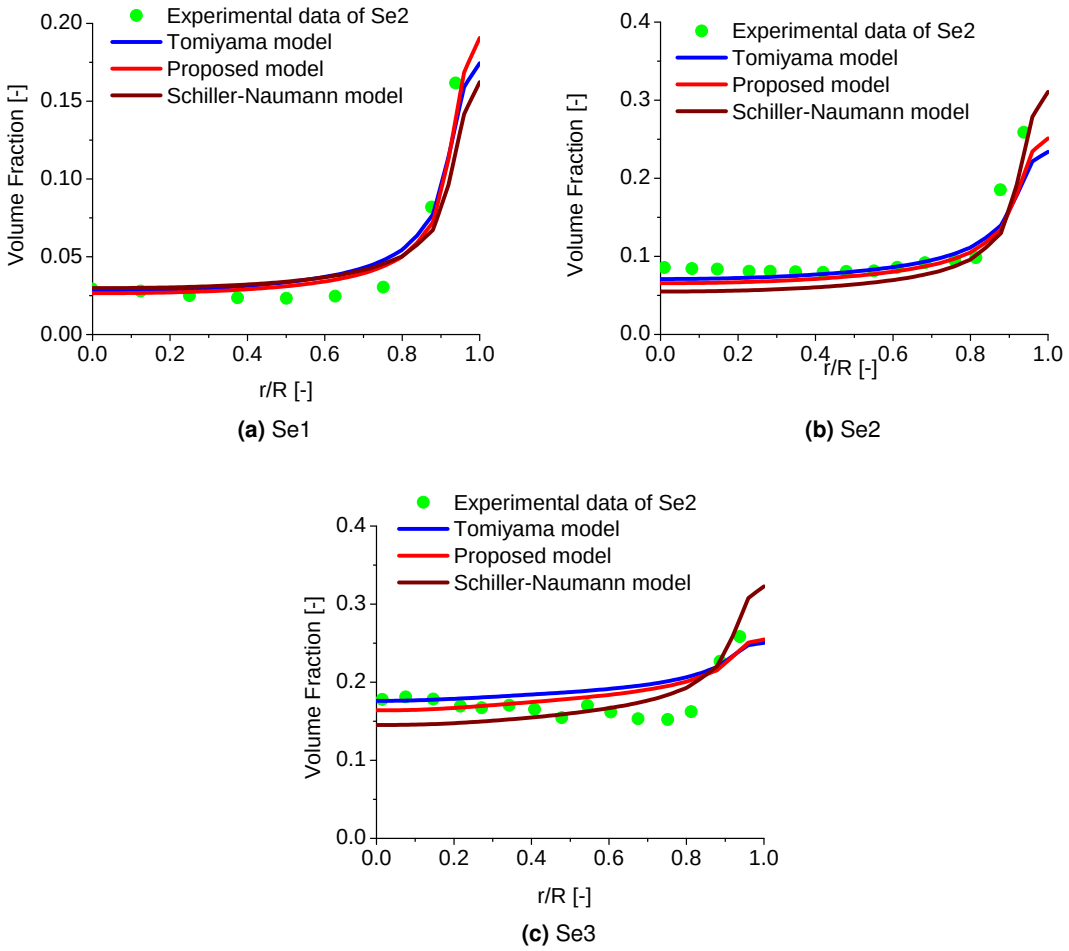

(a) Se1

(b) Se2

(c) Se3

Fig. 5.10: Volume fraction profiles obtained with different drag force models and compared with the experimental data provided by Serizawa et al. [80]

In the experiment of Serizawa et al. [80], the components of fluctuation velocity in the radial and azimuthal directions are not provided in the literature. Only the axial turbulence intensity was measured. Based on the assumption that the turbulence velocity scales are isotropic in axial, radial and azimuthal directions, the axial turbulent scale is introduced and equal to $(2k/3)^{1/2}$. Although this assumption is quite strong, several researchers still employed it to evaluate the turbulent properties of bubbly flow due to its simplicity and the limited measurement technology [90]. In this part of simulation, Rzehak model is employed to calculate the time scale τ_t. As discussed before, the predicted relative velocities by Ishii-Zuber model are quite similar to the results of Tomiyama model. Hence, Ishii-Zuber model is excluded in the following analysis.

Tests from Shawkat et al. [81]

The configuration of experiment conducted by Shawkat et al. [81] has been discussed in the previous chapter and it is not repeated here. Turning now to the major subject, assessment of the enhanced turbulent kinetic energy $\sqrt{k_l}$ with the proposed drag force model, we first take a look at the single phase test. Comparisons between calculated and measured values in Sh1 and Sh5 are shown in Fig. 5.12 for different liquid mass flow rates. In both cases, the wall peak of $\sqrt{k_l}$ is underestimated and values near the pipe center are slightly overestimated. In Sh1,

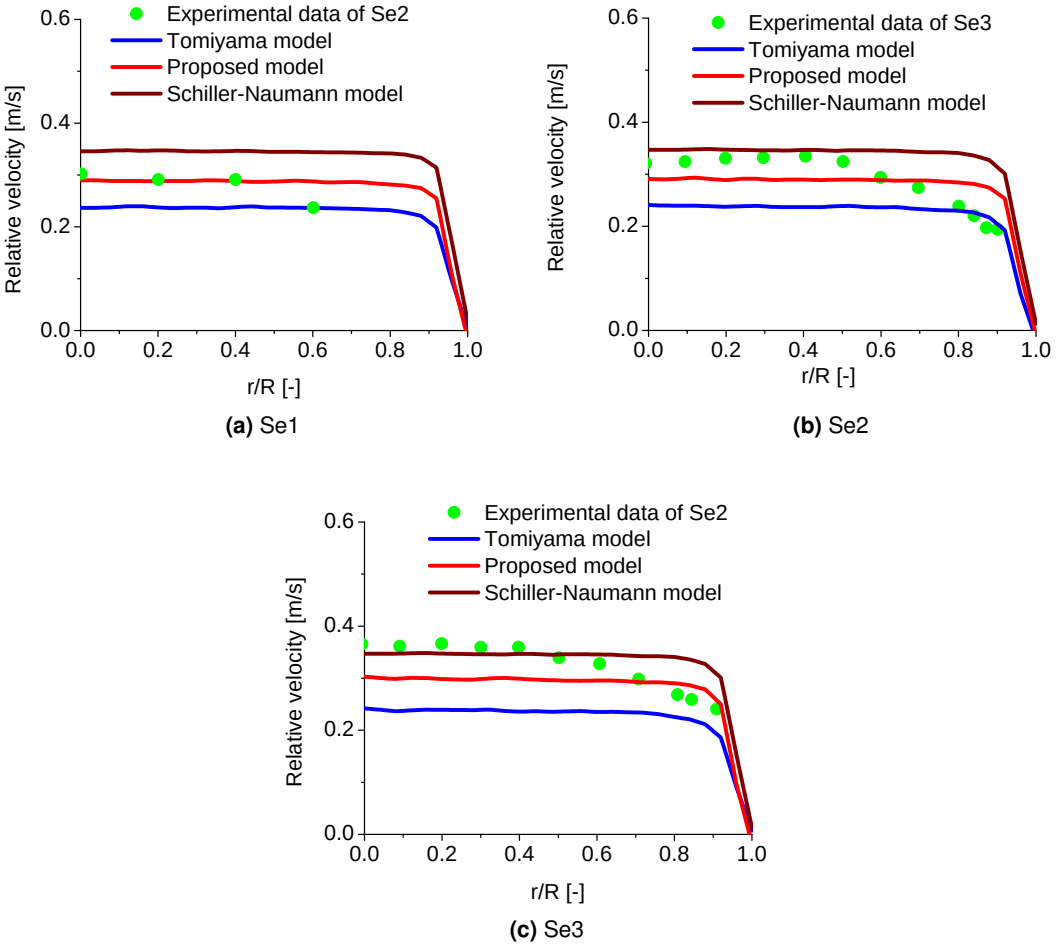

Fig. 5.11: Relative velocity profiles obtained with different drag force models and compared with the experimental data provided by Serizawa et al. [80]

the difference between calculated and measured values are more prominent in the near wall region, while the difference is more obvious in the pipe center as shown in the figure of the high flow rate case Sh5. As described in Wilcox [95], the flattened profile of $\sqrt{k_l}$ is attributed to the well-know shortcoming of the two equation turbulence model. The same trend is also reported in the work of Rzehak and Krepper [70] in which $\sqrt{k_l}$ is overestimated in the pipe center and agreement is improved near the pipe wall. In summary, the agreement between simulation and data is not quite good but still acceptable and corresponds to the general performance of the two equation turbulence model.

Measured and calculated volume fraction profiles are compared in Fig. 5.13. As for the simulation in the previous chapter, a quite good agreement is achieved in the radial direction. The discrepancy is most severe in Sh6 in which the whole calculated profiles are overestimated by all three drag force models. For the other cases, a good prediction is obtained while both liquid and gas fluxes vary from a low value to a high value. Hence, the error which comes from a bad result of volume fraction is minimized in the following analysis.

For the two-phase tests within the limits of expectation, there is reasonable agreement between calculated and measured values of turbulent kinetic energy as shown in Fig. 5.14. The radial profiles of $\sqrt{k_l}$ is qualitatively represented well by all three models, although the value of $\sqrt{k}$ is slightly overestimated in the near wall region. Among these models, the calculated values of Schiller-Naumann model are larger than the other models and this overestimation

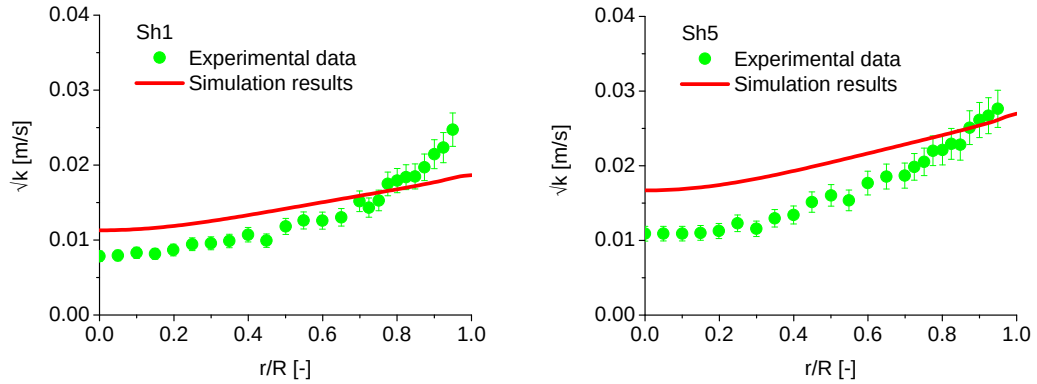

(a) Sh1 **(b)** Sh5

Fig. 5.12: Comparison of measured and predicted radial profiles of the square root of turbulent kinetic energy $\sqrt{k}$ for the single phase cases from Shawkat et al. [81]

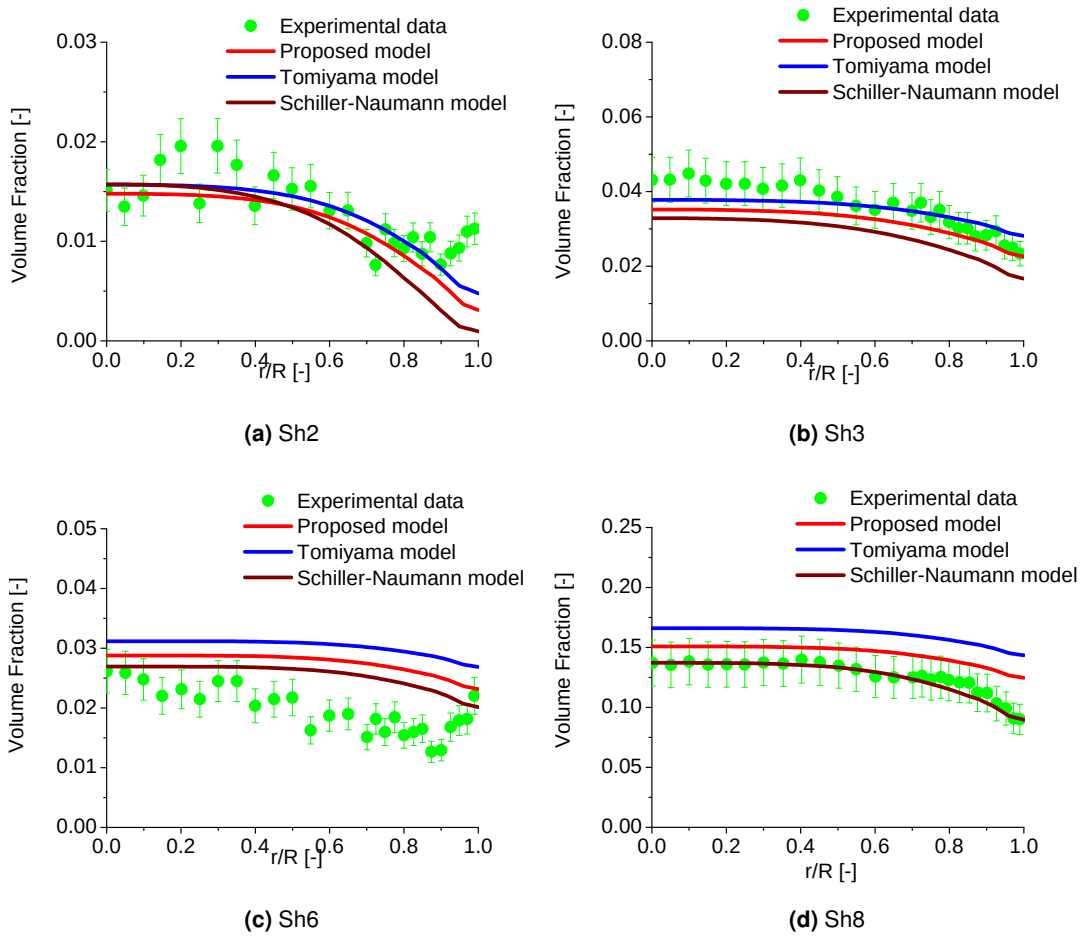

(a) Sh2 **(b)** Sh3

(c) Sh6 **(d)** Sh8

Fig. 5.13: Comparison of measured and predicted radial profiles of volume fraction for the two-phase cases from Shawkat et al. [81]

is more pronounced in the high volume fraction case Sh8. This is not surprising since as discussed before, the source term in k_l equation S_l^k is proportional to drag force and relative velocity. A larger value of turbulent kinetic energy can be expected if a higher relative velocity is predicted. Tomiyama model tends to provide the lowest value, while results of the proposed

drag force model are in between them.

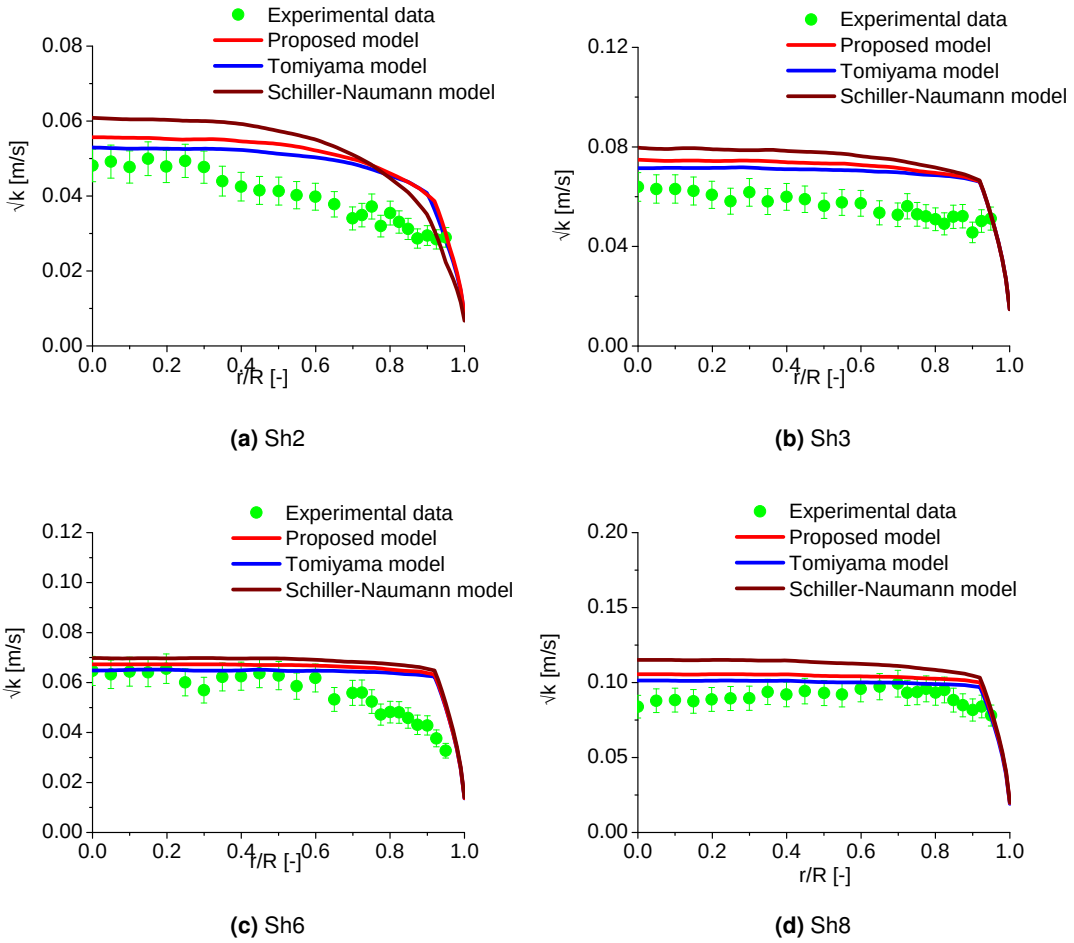

Fig. 5.14: Comparison of measured and predicted radial profiles of the square root of turbulent kinetic energy $\sqrt{k}$ for the two-phase cases from Shawkat et al. [81]

A corresponding comparison of liquid velocity is shown in Fig. 5.15. Here, agreement is satisfying in Sh2, Sh3 and Sh6 where resultant overestimations exist in the pipe center. Common to all tests is an underestimation of liquid velocity in the near wall region and it is attributed to the error in the measurement as discussed before. In addition, the profiles of relative velocity are not presented here for the reason that the choice of turbulence model has no influence on the determination of drag force.

Tests from Serizawa et al. [80]

The experiments conducted by Serizawa et al. [80] have two combinations of values for J_g as listed in Tab. 5.4, so that they are not repeated here. For the reason that turbulence in Se1 is obviously reduced, the prediction of Se1 is not included in the following analysis. Firstly, we take a look at the comparison of axial turbulent scale for the single phase test. The simulation and measurement data are plotted in Fig. 5.16. The phenomenon that the calculated profile is too flat is not observed in this figure while the calculated profile of axial turbulent scale is in an excellent agreement with experimental data. A similar prediction of the axial turbulent scale can be found in the single phase test by Troshko and Hassan [90].

Measured and calculated volume fraction profiles are compared in Fig. 5.17. Here, all profiles of volume fraction are wall-peaked. As for the simulations in the previous section,

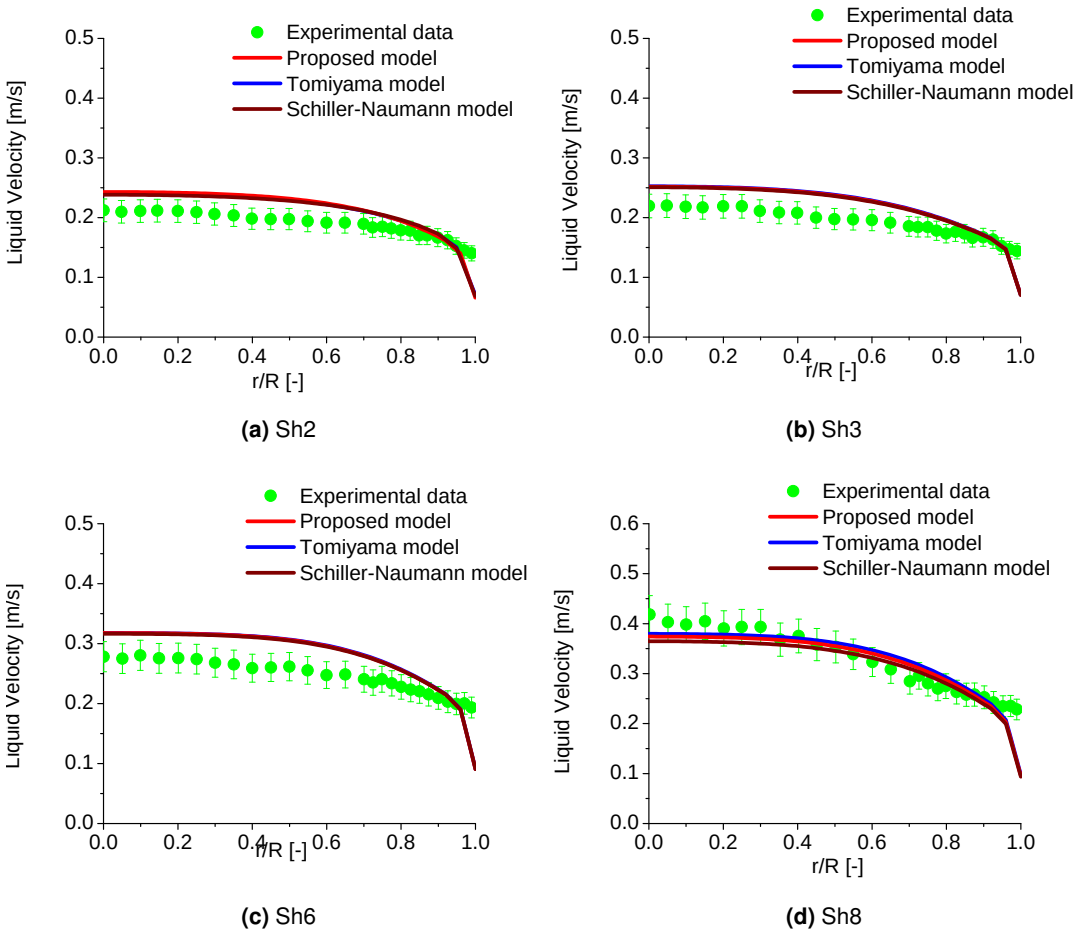

Fig. 5.15: Comparison of measured and predicted radial profiles of liquid velocity for the two-phase cases from Shawkat et al. [81]

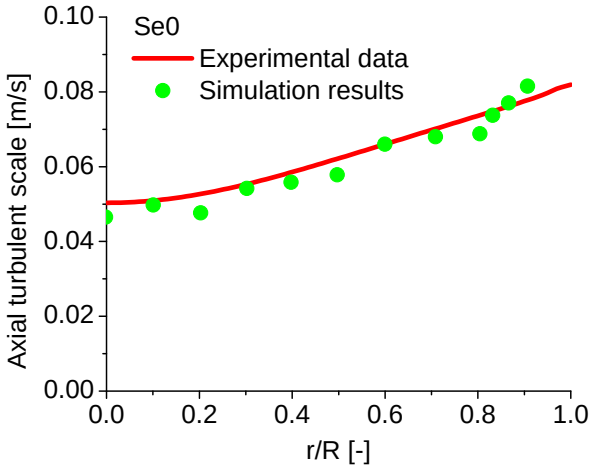

Fig. 5.16: Comparison of measured and predicted radial profiles of the axial turbulent scale for the single phase case from Serizawa et al. [80]

deviations are most prominent for the low gas flux case when r/R<0.6. They are most severe for Schiller-Naumann model and the proposed model, while the predition of Tomiyama model is relatively better. For Schiller-Naumann model, the deviations persist for the high gas flux

case, while Tomiyama model overestimates the volume fraction in the pipe center. It should be noted that the sharp increase of volume fraction in the near wall region is not captured in the simulation. The experimental data indicates that the lift force only exists in a small region near the wall. Hence, the employed lift force model needs further investigations.

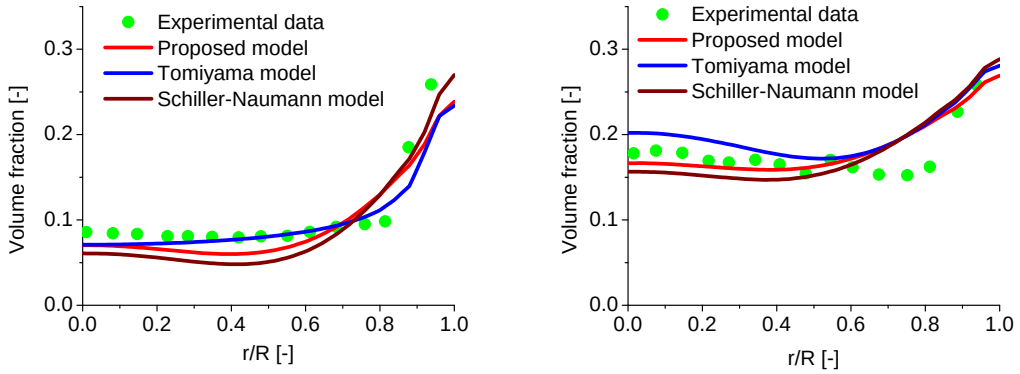

(a) Se2 **(b)** Se3

Fig. 5.17: Comparison of measured and predicted radial profiles of volume fraction for the two-phase cases from Serizawa et al. [80]

Results of axial turbulent scale for two phase tests are given in Fig. 5.18. All three drag force models generally give a good prediction of turbulent properties although they slightly overestimate the axial turbulent scale in the whole calculated profile, especially in the near wall region. In Se2, the results of the proposed drag force model approach the results of Schiller-Naumann model in the pipe center, but a small difference still exists in the near wall region. For the higher gas flux case, the predictions of the proposed model and Schiller-Naumann model are quite similar due to the similar profiles of relative velocity. Tomiyama model provides a relatively smaller value of axial turbulent scale due to the smallest relative velocity.

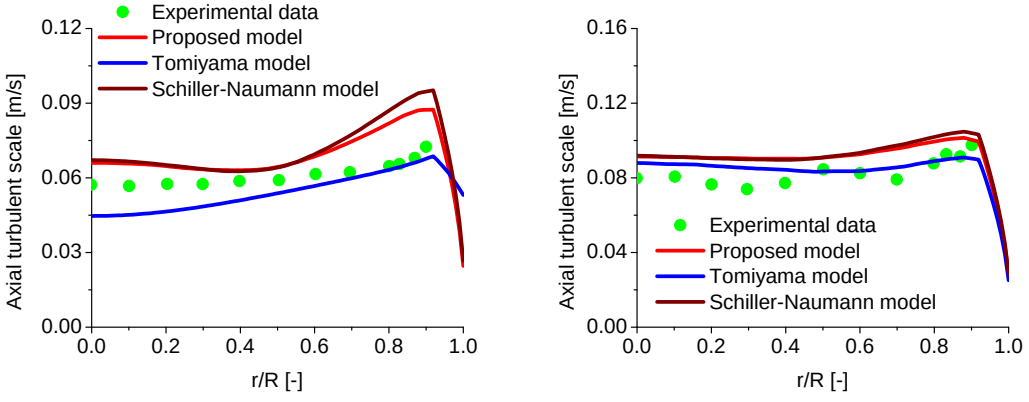

(a) Se2 **(b)** Se3

Fig. 5.18: Comparison of measured and predicted radial profiles of the axial turbulent scale for the two-phase cases from Serizawa et al. [80]

A corresponding comparison of the liquid velocity profiles is shown in Fig. 5.19. Differences among three models are more obvious. In the pipe center, the predictions are in agreement with the experiment, but liquid velocity is underestimated while approaching the wall. Given the agreement in the pipe center, it results in too steep profile of liquid velocity in the simulation

which is in agreement of the test of Liu [44] but in contrast to the tests of Serizawa [80]. In the original work of Hosokawa [30], a possible explanation and cure for this phenomenon has been given based on the analysis of the drag force. A flat profile of relative velocity is predicted by the simulation except the region near the wall, while experimental data show a substantial drop in the outer half of the pipe radius which is only slight for the lower value of liquid flux but significant for the higher value. Bubbles with a larger aspect ratio are observed near the wall and consequently lead to a higher drag force. This phenomenon may be caused by the small diameter pipe used in the experiment and still needs further investigations.

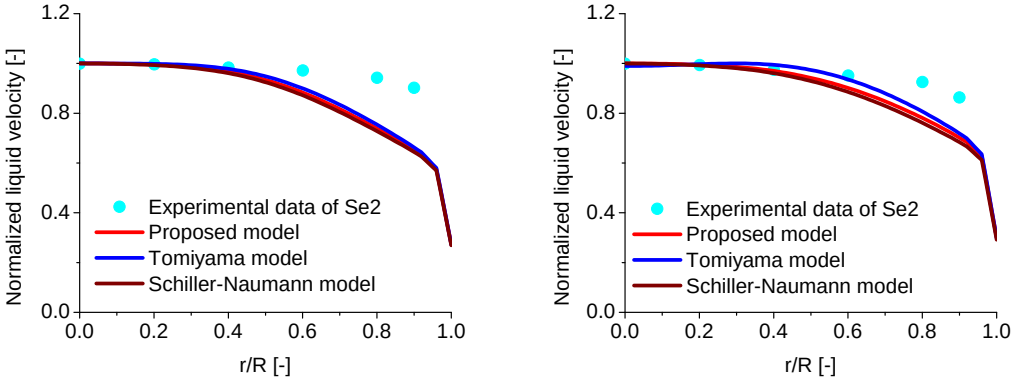

Fig. 5.19: Comparison of measured and predicted radial profiles of liquid velocity for the two-phase cases from Serizawa et al. [80]

5.3.3 Assessment of bubble induced turbulence models selected from literature

In section 5.1.2, different BIT models which are related to different modeling approaches of time scale τ_t are summarized in Tab. 5.2. In this section, the influence from the time scale will be studied and analyzed. The proposed drag force model is used to predict the drag force acting on dispersed bubbles.

Tests from Shawkat et al. [81]

As for the simulation in the previous section, measured and calculated volume fraction profiles of tests from Shawkat et al. [81] are compared in Fig. 5.20 and all three models discribed in Tab. 5.2 are included. Generally, the predicted profiles provided by three time scale models have a good agreement with experimental data. It is observed that the predictions obtained by three models are quite similar and the influence from the profile of volume fraction can be neglected in the following analysis.

A comparison for square root of turbulent kinetic energy $\sqrt{k_l}$ is shown in Fig. 5.21. For the two-phase tests within the limits of expectation, all three models predict the general trend of the radial profile of $\sqrt{k_l}$. The peak value of $\sqrt{k_l}$ is observed in the pipe center and its lowest value exists in the near-wall region. Among three models, Rezehak and Morel models provide good agreement between calculated and measured values. However, slight overestimations are still observed in Sh3. However, the values predicted by Troshko model are much larger than experimental data, especially in Sh3 and Sh8 in which averaged volume fraction is relatively larger. These discrepancies between calculated and measured values are supposed to be

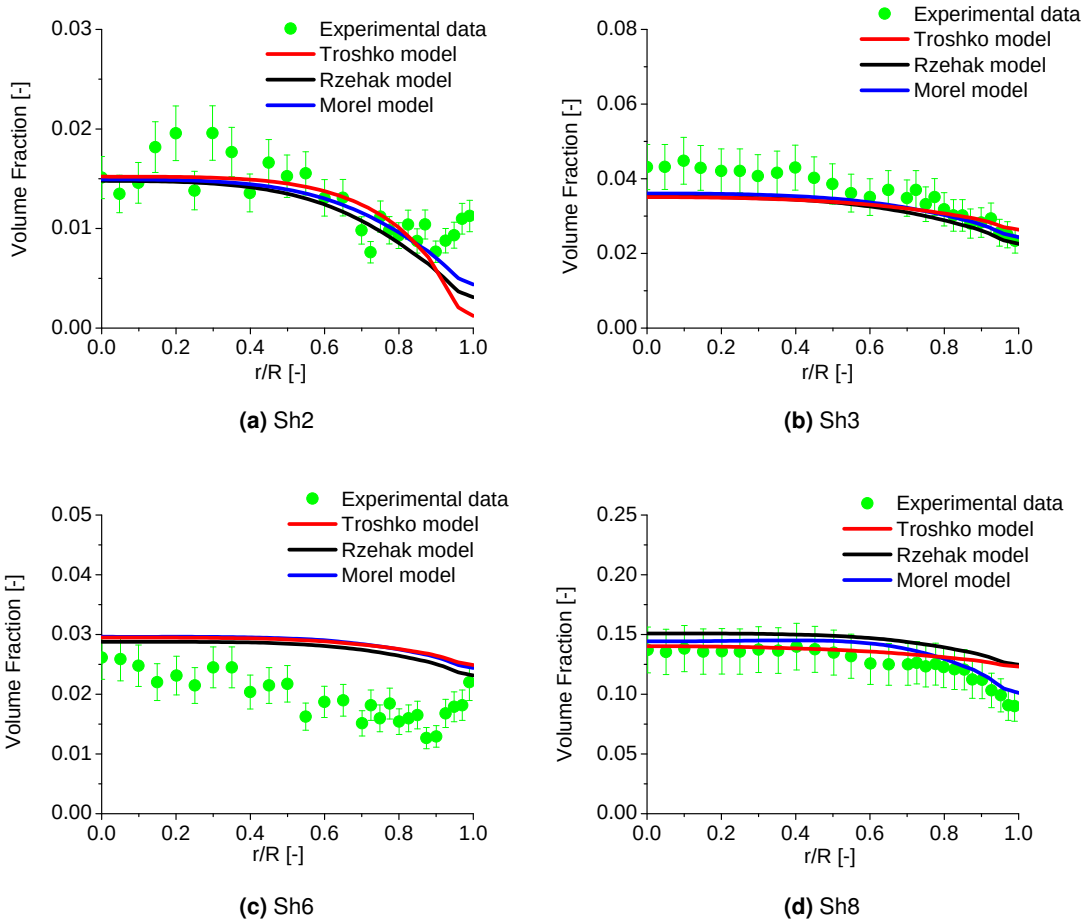

Fig. 5.20: Comparison of measured and predicted radial profiles of volume fraction for the two-phase cases from Shawkat et al. [81]

caused by the drawback of the two phase k-ϵ model. It is not surprising since as discussed before the contribution from turbulent dissipation term is adjusted by the factor $C_{\epsilon B}$. The value of $C_{\epsilon B}$ is optimized based on the experimental data. In the study of Troshko and Hassan [90], the measured magnitude of Reynolds shear peak was chosen as a calibration parameter to tune its value. To produce a good quantitative agreement, the value of this constant was set to 0.45. In other studies of bubble induced turbulence, its value varies from case to case. Until now, no general model is proposed to determine the value of $C_{\epsilon B}$. And this discrepancy is more pronounced in the high volume fraction cases in which a larger dissipation term can be expected.

Tests from Serizawa et al. [80]

Results of volume fraction profile in tests of Serizawa are given in Fig. 5.22. Here, the wall-peaked profiles of volume fraction in two cases are well produced. Generally, reasonable agreement between calculated and measured values is obtained in the radial direction. However, the deviations found in the previous section still exist here. The calculated profiles are quite similar to the simulation results obtained before. For the low gas flux case, most prominent deviations of simulation results are observed near the pipe center, while the calculated values of volume fraction near $r/R = 0.8$ are much larger in the high gas flux case.

Measured and calculated axial turbulent profiles are compared in Fig. 5.23. As shown

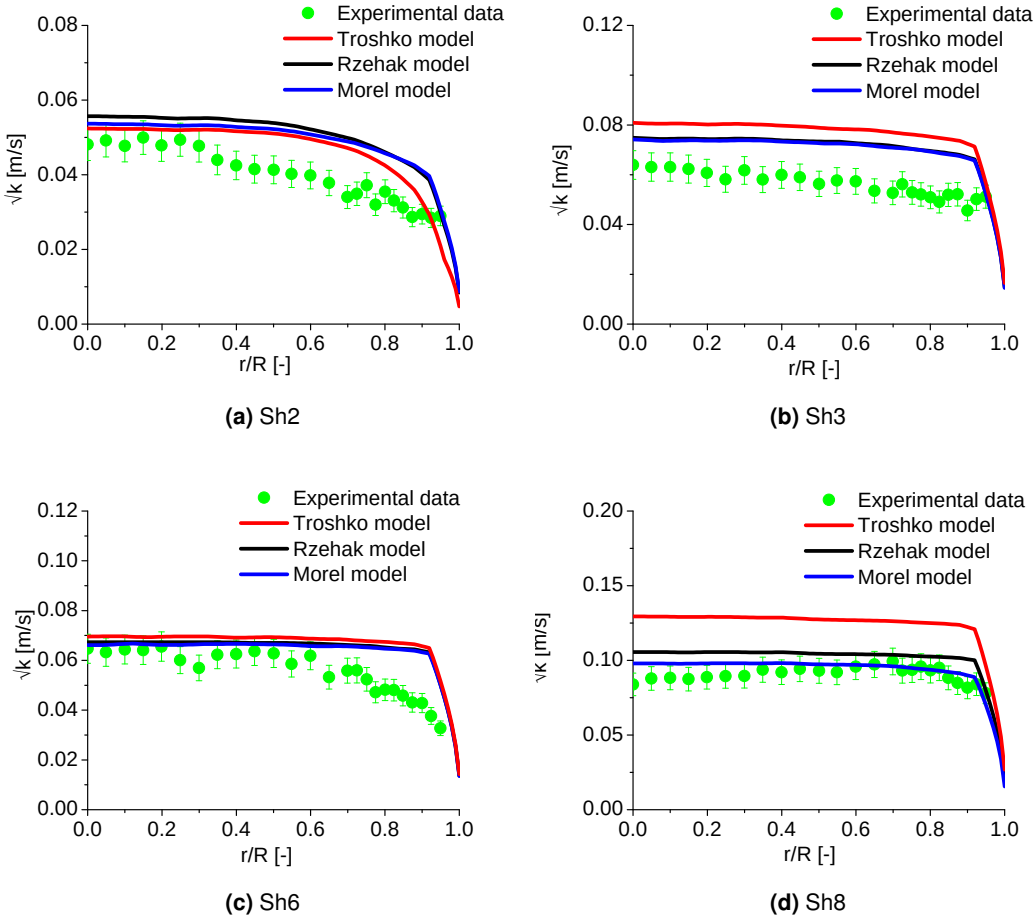

Fig. 5.21: Comparison of measured and predicted radial profiles of the square root of turbulent kinetic energy $\sqrt{k}$ for the two-phase cases from Shawkat et al. [81]

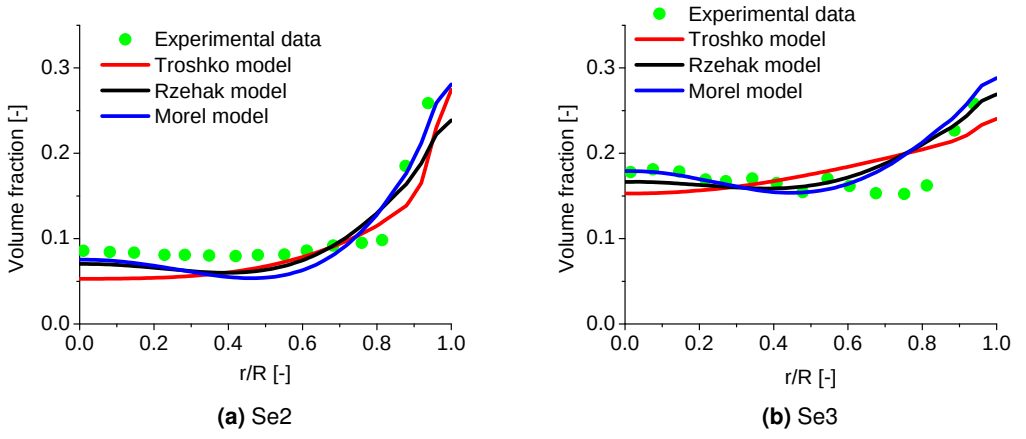

Fig. 5.22: Comparison of measured and predicted radial profiles of volume fraction for the two-phase cases from Serizawa et al. [80]

before, Rzehak and Morel models generally give good agreement of turbulent properties although they slightly overestimate the turbulent kinetic energy in the near-wall region when gas flux is small. For Troshko model, the profile of axial turbulence scale is quite similar to the predictions of Rzehak and Morel models but its value is much larger. A similar prediction can

be found in the work of Troshko and Hassan [90]. As discussed before, this discrepancy is caused by the factor $C_{\epsilon B}$ and a larger $C_{\epsilon B}$ is expected to minimize this discrepancy.

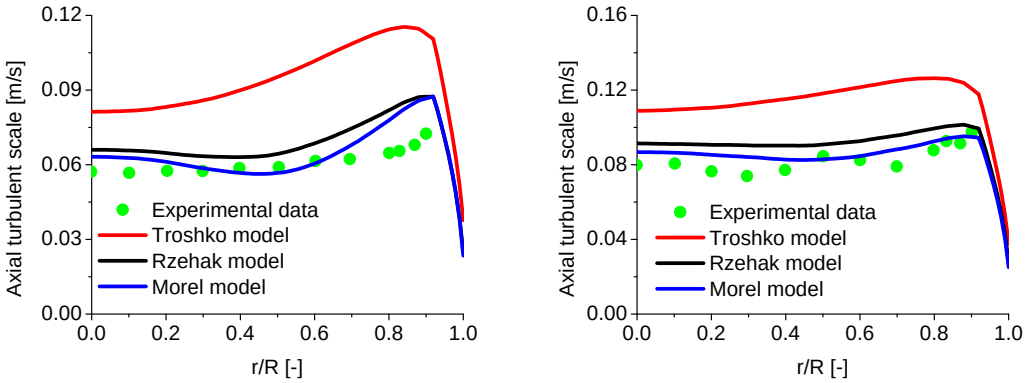

(a) Se2 **(b)** Se3

Fig. 5.23: Comparison of measured and predicted radial profiles of the axial turbulent scale for the two-phase cases from Serizawa et al. [80]

5.4 Conclusion and discussion

In this chapter, the proposed drag force model is implemented into two-fluid model and employed to predict flow properties of bubbly flow. The performance of the proposed drag force model is examined in comparison with the experimental data and the existing drag force models. To account for the enhanced turbulence due to the existence of bubbles, additional terms which are dependent on the drag force coefficient are introduced into k and ϵ equations to predict bubble induced turbulence. Moreover, the performances of different BIT models are also assessed. The most important conclusions are summarized here:

- With the proposed correlations of turbulent wake and vertical distance between neighboring bubbles, the selected test cases of bubbly flow are recalculated. The simulation results reveal that the proposed drag force model provides a better prediction accuracy of relative velocity than existing models which are available in most CFD codes. Especially, the proposed model gives a best overall estimation with acceptable errors when the distribution of relative velocity shows a strong variation in the radial direction. Moreover, comparing to the existing models, one important feature of the proposed model is the dependency of relative velocity on volume fraction. With the proposed model, a more physical interpretation of the wake acceleration effect is established without introducing any additional parameters.
- The dependency of the predicted turbulent kinetic energy on the drag force modeling is quite obvious. Generally, the proposed drag force model shows a good performance to predict the enhanced turbulent kinetic energy in liquid phase.
- The employed BIT models show a similar performance in the prediction of the enhanced turbulence kinetic energy. Rzehak model and Morel model give overall the best performance and is hence recommended for the future simulation However, deviations are still observed in the simulation, especially when averaged volume fraction is high. These discrepancy is related to the value of $C_{\epsilon B}$ which is tuned based on the experimental data. The determination of its value still needs further investigations.

6. Conclusion and outlook

Prediction accuracy of dispersed gas-liquid multiphase flow is strongly dependent on drag force modeling. Subject of the current study is to propose a drag force model which considers the wake acceleration effect under high volume fraction and high bubble Reynolds number conditions. With the proposed drag force model, the relationship between the increased rising velocity of the affected bubble and the wake velocity is modeled. It was found that there is a strong dependency of the increased bubble rising velocity on bubble aspect ratio, wake velocity and volume fraction. A systematic CFD simulation covering a wide range of bubble diameter was also carried out to investigate the velocity profile of unstable wake. Based on the simulation results, correlations are proposed to describe the wake velocity profile with some characteristics parameters of bubble. The proposed drag force model with the correlations of wake velocity was implemented into two-fluid model and employed in RANS simulation of bubbly flows which were conducted in pipes of different diameters. Finally, the proposed model was also used to assess the bubble inducted turbulence by comparing the turbulent kinetic energy with experimental data. The most important conclusions obtained in the present study can be summarized as below:

- Based on the concept of defining a new proper reference velocity, a detailed investigation of velocity field around an oblate bubble was carried out. Key constitutive relation of the new drag force model was proposed, with which the relationship between the increased rising velocity and the wake velocity was modeled. The improvement of the proposed drag force model includes two aspects:
  - The proposed drag force model includes the influence from bubble deformation and no artificial factor is employed in the model. The uses of the constants in the model are obtained by the derivation proposed by Lamb [39]. Hence, there is no necessary to optimize the proposed model.
  - The proposed drag force model is dependent on the wake velocity. For a laminar wake, its wake velocity profile is estimated based on laminar boundary layer theory. However, it is infeasible to give a solution of a turbulent wake with an analytical method. This problem is solved by using CFD approach.
- In order to determinate the required velocity profile of unstable wake, CFD approach, here VOF method with LES model was chosen, was employed to capture the motions of a single bubble rising freely in the stagnant water. By recalculating selected experimental and DNS studies conducted by Brücker [11] and Gaudlitz and Adams [25], the main features of the simulated bubble, which includes the rising velocity, the deformed shape and other characteristics parameters related to its oscillation in trajectory and velocity, were well captured. It demonstrated the capability of the employed approach to capture the interface movements and predict the wake properties under high Re_b condition.
- With the validated CFD approach, simulation and analysis of unstable wake was carried out under high bubble Reynolds number condition. A close examination of the simulation

results revealed that turbulent boundary layer theory has potential to evaluate the wake velocity profile in both vertical and radial directions. Based on a systematic simulation covering a wide range of bubble diameter, correlations were proposed to provide an estimation of wake velocity in terms of bubble terminal velocity, bubble diameter and so on.

- The above proposed drag force model was implemented into two-fluid model. RANS model was employed to predict the turbulent properties in the liquid field. Application of the proposed drag force model was performed by recalculating the selected test cases of bubbly flow conducted by Shawkat et al. [81] and Serizawa et al. [80]. It revealed that the proposed drag force model provides a better prediction accuracy of relative velocity than Tomiyama [87] model and Schiller-Naumann model [77] which are currently available in most CFD codes. In addition, the proposed drag force model was also validated against the experimental and numerical studies of bubbles pairs.
- Finally, the proposed drag force model with different BIT models was employed to assess the enhanced turbulence caused by the relative motions of dispersed bubbles. It revealed that the models proposed by Rzehak and Krepper [70] and Morel [52] show overall the best prediction accuracy and are hence recommended to predict the bubble induced turbulence in the future work.

As outlook for the future work the following points should be mentioned:

- In the current study, validation of the employed CFD approach is performed by comparing several macroscopic parameters of the rising bubble against the experimental and numerical data. 3-D measured data of wake velocity are highly required for validation of the employed CFD approach. As the measurement of wake velocity becomes available in the future, more validation calculations should be carried out.
- The proposed drag force model is validated under low and high Re_b number conditions, respectively. For completeness, the transition region needs to be further studied when experimental or simulation data are available.
- A constant factor $C_{\epsilon B}$ is introduced to adjust the contribution of a source term in the turbulent dissipation equation. This factor varies from case to case and its value is usually determined by comparison to experimental data. More experimental and numerical investigations should be carried out in the future.

A. Wake velocity profile at low bubble Reynolds number

For completeness, the expression of wake velocity profile at low Re_b number is derived in details for 2D axis-symmetric case. In the derivation, a single spherical bubble rising in the stagnant water is considered. In order to simplify the derivation, a moving cylindrical reference frame (x, r) whose origin is always attached to the bubble center is employed in the follow study, as shown in Fig. A.1. (X, Z) is a fixed Cartesian reference. The bubble rising velocity in the reference (X, Z) is V_T, so that the magnitude of the relative velocity between two reference frames is also V_T.

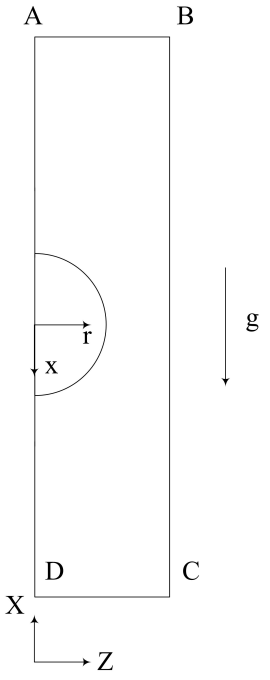

Fig. A.1: Axis-symmetry control volume outside the considered bubble

If neglecting the velocity fluctuation in liquid phase, the governing equation in the wake behind a bubble with a diameter d can be expressed in cylindrical coordinates as, see Schlichting and Gersten [78] for details:

$$V_T \frac{\partial U}{\partial x} = \frac{\nu}{r} \frac{\partial}{\partial r} \left(r \frac{\partial U}{\partial r} \right) \tag{A.1}$$

Here, U stands for the velocity in the x direction and ν is the dynamic viscosity of the fluid around the bubble.

With the trial solution:

$$U = -V_T C \left(\frac{x}{d} \right)^{-m} F(\eta) + C, \eta = \frac{r}{2} \sqrt{\frac{V_T}{\nu x}} \tag{A.2}$$

$F(\eta)$ stands for a function which depends on the η. In the reference of (x, r), when $x \to \infty$ and $r \to \infty$, the liquid velocity approaches V_T. The constant C in Eq. A.2 is equal to V_T.

Putting trial solution into both left and right hand sides of Eq. A.1 yields:

$$V_T \frac{\partial U}{\partial x} = -CV_T^2 d^m x^{-m-1} \left(-mF(\eta) - F'(\eta) \frac{r}{4} \sqrt{\frac{V_T}{\nu}} x^{-\frac{1}{2}} \right) \tag{A.3}$$

$$\begin{aligned} r\frac{\partial U}{\partial r} &= -rV_T rC\left(\frac{z}{d}\right)^{-m} F'(\eta) \frac{1}{2} \sqrt{\frac{V_T}{\nu z}} \\ \frac{\nu_{eff}}{r} \frac{\partial}{\partial r} \left(r\frac{\partial U}{\partial r} \right) &= -CV_T \frac{\nu_{eff}}{r} \left(\frac{z}{d}\right)^{-m} \frac{1}{2} \sqrt{\frac{V_T}{\nu z}} \left(F'(\eta) + rF''(\eta) \frac{1}{2} \sqrt{\frac{V_T}{\nu z}} \right) \end{aligned} \tag{A.4}$$

Putting Eq. A.3 and Eq. A.4 into Eq. A.1 yields:

$$\begin{aligned} &-CV_T^2 d^m z^{-m-1} \left(-mF(\eta) - F'(\eta) \frac{r}{4} \sqrt{\frac{V_T}{\nu}} z^{-\frac{1}{2}} \right) \\ &\quad = -CV_T \frac{\nu}{r} \left(\frac{z}{d}\right)^{-m} \frac{1}{2} \sqrt{\frac{V_T}{\nu z}} \left(F'(\eta) + rF''(\eta) \frac{1}{2} \sqrt{\frac{V_T}{\nu z}} \right) \end{aligned} \tag{A.5}$$

Simplify Eq. A.5:

$$\eta F''(\eta) + \left(2\eta^2 + 1\right) + 4m\eta F(\eta) = 0 \tag{A.6}$$

The component m is still unknown, and it can be determined via a global momentum balance around the body. The axis-symmetry control volume with angle θ is placed far enough away from the body that the pressure on it is unperturbed. The pressure is constant over the whole of the control surface and so there is no contribution of the momentum balance from the pressure forces. According to the continuity equation, the difference between that entering through *AB* and leaving through *CD* is equal to the quantity of fluid leaving through *BC*. The volume and momentum flux on each cross section are summarized in Tab. A.1.

Cross-section	Volume flux	Momentum flux
AB	$\rho \int_0^h V_T r\theta dr$	$\rho \int_0^h V_T^2 r\theta dr$
BC	$-\rho \int_0^h (V_T - U) r\theta dr$	$-\rho \int_0^h V_T (V_T - U) r\theta dr$
CD	$-\rho \int_0^h U r\theta dr$	$-\rho \int_0^h U^2 r\theta dr$
AD	0	0
$\sum$ = *control surface*	$\sum$ *volume flux* = 0	$\sum$ *momentum flux* = *drag*

Tab. A.1: Balance of volume flux and momentum on the control surface in Fig. A.1

The momentum loss D on the flow direction is caused by the drag force, thus giving us:

$$D = \rho \int_0^h U(V_T - U) r\theta dr \tag{A.7}$$

With the trial solution of u, yields:

$$D \approx \rho \int_0^h V_T \left(V_T - U\right) r\theta dr = 4C\rho\theta V_T^2 \left(\frac{x}{l}\right)^{-m} \frac{\nu x}{V_T} \int_0^{+\infty} F\left(\eta\right)\eta d\eta \tag{A.8}$$

Since the balance must be independent of x, it follows that m=1. Equation thus determined becomes:

$$\eta F''\left(\eta\right) + \left(2\eta^2 + 1\right) F'\left(\eta\right) + 4\eta F\left(\eta\right) = 0 \tag{A.9}$$

which, after integrating once, yields:

$$\eta\left(F'\left(\eta\right) + 2\eta F\left(\eta\right)\right) = 0 \tag{A.10}$$

With the solution:

$$F\left(\eta\right) = e^{-\eta^2} \tag{A.11}$$

Using the integral:

$$\int_0^{+\infty} F\left(\eta\right)\eta d\eta = \frac{1}{2} \int_0^{+\infty} e^{-\eta^2} d\eta^2 = \frac{1}{2} \tag{A.12}$$

It follows from Eq. A.8 that the drag coefficient is:

$$\begin{aligned} C_d &= \frac{D}{\frac{\rho}{2} V_T^2 \frac{\theta}{2\pi} \pi \frac{d^2}{4}} \\ &= \frac{4C\rho\theta V_T^2 \left(\frac{z}{l}\right)^{-1} \frac{\nu z}{V_T} \int_0^{+\infty} F\left(\eta\right)\eta d\eta}{\frac{\rho}{2} V_T^2 \frac{\theta}{2\pi} \pi \frac{d^2}{4}} \\ &= \frac{32C\nu}{dV_T} \end{aligned} \tag{A.13}$$

The final solution for the velocity profile of wake behind the spherical bubble with drag coefficient C_d is:

$$U = -V_T \frac{C_d d^2 V_T}{32x\nu} \exp\left(-\frac{r^2 V_T}{4x\nu}\right) + V_T \tag{A.14}$$

Thus, the velocity profile of wake in the Cartesian reference frame is obtained as:

$$\begin{aligned} U_w &= V_T - U \\ &= V_T - \left(-V_T \frac{C_d d}{32x} \mathrm{Re} \exp\left(-\frac{r^2 V_T}{4x\nu}\right) + V_T\right) \\ &= V_T \frac{C_d d}{32x} \mathrm{Re} \exp\left(-\frac{r^2 V_T}{4x\nu}\right) \end{aligned} \tag{A.15}$$

B. Wake velocity profile at high bubble Reynolds number

In Appendix A, an analytic expression of wake velocity profile is deduced based on the laminar boundary layer theory at low Re_b number. In this section, the derivation of the velocity profile of an unstable wake is provided based on the turbulent boundary layer theory. The configuration of the derivation is the same as that of the previous derivation.

If considering the velocity fluctuation of liquid phase and employing Reynolds decomposition, the governing equation in the wakes behind a deformed bubble with a equivalent diameter d, can be expressed in cylindrical coordinates as:

$$V_T \frac{\partial U}{\partial x} + \frac{1}{r}\frac{\partial \left(r\overline{u'v'}\right)}{\partial r} = \frac{\nu}{r}\frac{\partial}{\partial r}\left(r\frac{\partial U}{\partial r}\right) \tag{B.1}$$

Here, u' and v' stands for the velocity fluctuation in the vertical and radial directions, respectively. — stands for the time-averaging.

If we define a turbulent viscosity $\overline{u'v'} = -\nu_t \partial U/\partial r$, the governing equation can be modified to:

$$V_T \frac{\partial U}{\partial x} = \frac{\nu}{r}\frac{\partial}{\partial r}\left(r\frac{\partial U}{\partial r}\right) + \frac{1}{r}\frac{\partial}{\partial r}\left(r\nu_t\frac{\partial U}{\partial r}\right) \tag{B.2}$$

If assuming that the turbulent viscosity ν_t is a constant and employing $\nu_{eff} = \nu + \nu_t$, it yields:

$$V_T \frac{\partial U}{\partial x} = \frac{\nu_{eff}}{r}\frac{\partial}{\partial r}\left(r\frac{\partial U}{\partial r}\right) \tag{B.3}$$

Similar to the derivation in Appendix Appendix A, the trial solution is employed in the derivation as follows:

$$U = -V_T C\left(\frac{x}{d}\right)^{-m} F(\eta) + C, \eta = \frac{r}{2}\sqrt{\frac{V_T}{\nu_{eff} x}} \tag{B.4}$$

With the same approach employed in the previous derivation, the final solution to Eq. B.3 with drag coefficient C_d is written as:

$$U = -V_T \frac{C_d d^2 V_T}{32 x \nu_{eff}} \exp\left(-\frac{r^2 V_T}{4 x \nu_{eff}}\right) + V_T \tag{B.5}$$

Thus, the wake velocity profile in the Cartesian reference frame is obtained as:

$$\begin{aligned} U_w &= V_T - U \\ &= V_T - \left(-V_T \frac{C_d d}{32 x}\mathrm{Re}\exp\left(-\frac{r^2 V_T}{4 x \nu_{eff}}\right) + V_T\right) \\ &= V_T \frac{C_d d}{32 x}\mathrm{Re}\exp\left(-\frac{r^2 V_T}{4 x \nu_{eff}}\right) \end{aligned} \tag{B.6}$$

C. Velocity distribution around an oblate bubble

In this coordinate system shown in Fig. 3.4, the values of the linear elements δS_θ, δS_ϕ and δS_ξ described by the point (x, y, z) when θ, ϕ, ξ separately vary are:

$$\begin{aligned} \delta S_\theta &= h_\theta \delta\theta \\ \delta S_m &= h_m \delta m \\ \delta S_\xi &= h_\xi \delta\xi \end{aligned} \tag{C.1}$$

where h_θ, h_m and h_ξ are the scale factors for the coordinates θ, m and ξ, respectively. The value of them can be estimated as follows (Abramowitz and Stegun [2]):

$$\begin{aligned} h_\theta^2 &= \left(\frac{\partial x}{\partial \theta}\right)^2 + \left(\frac{\partial y}{\partial \theta}\right)^2 + \left(\frac{\partial z}{\partial \theta}\right)^2 = k^2\left(1+\xi^2\right)\left(1-m^2\right) \\ h_m^2 &= \left(\frac{\partial x}{\partial m}\right)^2 + \left(\frac{\partial y}{\partial m}\right)^2 + \left(\frac{\partial z}{\partial m}\right)^2 = k^2\left(\frac{\xi^2+m^2}{1-m^2}\right) \\ h_\xi^2 &= \left(\frac{\partial x}{\partial \xi}\right)^2 + \left(\frac{\partial y}{\partial \xi}\right)^2 + \left(\frac{\partial z}{\partial \xi}\right)^2 = k^2\left(\frac{\xi^2+m^2}{1+\xi^2}\right) \end{aligned} \tag{C.2}$$

In the Cartesian coordinates, the normal vector that is perpendicular to the surface of this spheroid can be expressed as:

$$\begin{aligned} \mathbf{n} =& k^2\lambda\sqrt{1+\lambda^2}\left(1-m^2\right)\cos\theta\mathbf{e}_x + k^2\lambda\sqrt{1+\lambda^2}\left(1-m^2\right)\sin\theta\mathbf{e}_y \\ &+ k^2\left(1+\lambda^2\right)\sqrt{1-m^2}\cos\phi\mathbf{e}_z \end{aligned} \tag{C.3}$$

where $\mathbf{e}_x$, $\mathbf{e}_y$, $\mathbf{e}_z$ are the unit vectors in the x, y and z directions.

In fluid dynamics, a potential flow is described by means of a velocity potential Φ, being a function of space and time. The governing equation of Φ in the Cartesian coordinates can be expressed as:

$$\frac{\partial^2\Phi}{\partial x^2} + \frac{\partial^2\Phi}{\partial y^2} + \frac{\partial^2\Phi}{\partial z^2} = 0 \tag{C.4}$$

Rewriting it in the oblate spheroidal coordinates yields:

$$\frac{\partial}{\partial\xi}\left[\left(1+\xi^2\right)\frac{\partial\Phi}{\partial\xi}\right] + \frac{\partial}{\partial m}\left[\left(1-m^2\right)\frac{\partial\Phi}{\partial m}\right] + \frac{\left(\xi^2+m^2\right)}{\left(1+\xi^2\right)\left(1-m^2\right)}\frac{\partial^2\Phi}{\partial\theta^2} = 0 \tag{C.5}$$

The flow velocity is a vector field equal to the gradient of the velocity potential and is

evaluated as follows:

$$\begin{aligned}\frac{\partial \Phi}{\partial S_\theta} &= v_\theta \\ \frac{\partial \Phi}{\partial S_m} &= v_m \\ \frac{\partial \Phi}{\partial S_\xi} &= v_\xi\end{aligned} \tag{C.6}$$

In the case of symmetry about the axis, the velocity u_θ can be neglected in the analysis. Hence, the last term in the Eq. C.5 is removed and it yields:

$$\frac{\partial}{\partial \xi}\left[\left(1+\xi^2\right)\frac{\partial \Phi}{\partial \xi}\right] + \frac{\partial}{\partial m}\left[\left(1-m^2\right)\frac{\partial \Phi}{\partial m}\right] = 0 \tag{C.7}$$

According to the analytic solution of Eq. C.7 provided by Lamb [39], the velocity potential Φ for an inviscid incompressible flow about a moving spheroid with the minor axis $b = k\xi_0$ and the major axis $a = k(1-\xi_0^2)^{1/2}$ is given by:

$$\Phi = Qm\left(1 - \xi_0 \cot^{-1}\xi_0\right) \tag{C.8}$$

where:

$$Q = \frac{kV_T}{\xi_0\left(\xi_0^2+1\right)^{-1} - \cot^{-1}\xi_0} \tag{C.9}$$

Substituting Eq. C.1 and Eq. C.2 into Eq. C.6, the velocity components u_m and u_ξ are given as follows:

$$\begin{aligned}u_m &= \frac{1}{k}\sqrt{\frac{1-m^2}{\xi^2+m^2}}\frac{\partial \Phi}{\partial m} \\ u_\xi &= \frac{1}{k}\sqrt{\frac{\xi^2+1}{\xi^2+m^2}}\frac{\partial \Phi}{\partial \xi}\end{aligned} \tag{C.10}$$

Substituting Eq. C.9 and Eq. C.8 into Eq. C.10 yields the following normal and tangential components of liquid velocity on the surface of an oblate spheroid:

$$\begin{aligned}u_\xi &= V_T m\sqrt{\frac{\xi_0^2+1}{\xi_0^2+m^2}} \\ u_m &= V_T\sqrt{\frac{1-m^2}{\xi_0^2+m^2}}\frac{1-\xi_0\cot^{-1}\xi_0}{\xi_0\left(\xi_0^2+1\right)^{-1} - \cot^{-1}\xi_0}\end{aligned} \tag{C.11}$$

The liquid velocity on the bubble upper surface in the frame of reference moving with the oblate bubble can be deduced by subtracting $V_T\mathbf{e}_z$ from the above equations. Here, $\mathbf{e}_z$ is the unit vector in the z direction. As shown in Fig. 3.2, if α is introduced to denote the angle between the unit normal vector of bubble interface $\mathbf{n}$ and the unit vector in the z direction $\mathbf{e}_z$, its cosine value is calculated as follows:

$$\begin{aligned}\mathbf{e}_z \cdot \mathbf{n} &= \cos\alpha = m\sqrt{\frac{\xi_0^2+1}{\xi_0^2+m^2}} \\ \mathbf{e}_z \cdot \mathbf{t} &= \sin\alpha = \xi_0\sqrt{\frac{1-m^2}{\xi_0^2+m^2}}\end{aligned} \tag{C.12}$$

Hence, $V_T\mathbf{e}_z$ can be decomposed into the ξ and θ components as follows:

$$\begin{aligned} V_\xi &= V_T\mathbf{e}_z \cdot \mathbf{n} = V_T m \sqrt{\frac{\xi_0^2+1}{\xi_0^2+m^2}} \\ V_m &= V_T\mathbf{e}_z \cdot \mathbf{t} = V_T \xi_0 \sqrt{\frac{1-m^2}{\xi_0^2+m^2}} \end{aligned} \tag{C.13}$$

Consequently, in the frame of reference moving with the oblate bubble, the normal and tangential components, u_n and u_t of liquid velocity on the upper part of bubble surface are given by:

$$\begin{aligned} u_n &= u_\xi - V_\xi = 0 \\ u_t &= u_m - V_m = V_T \sqrt{\frac{1-m^2}{\xi_0^2+m^2}} \frac{1}{\left(\xi_0^2+1\right)\cot^{-1}\xi_0 - \xi_0} \end{aligned} \tag{C.14}$$

Since $E = \xi_0/\sqrt{1+\xi_0^2}$, ξ_0 in the above equation can be replaced with $E/\sqrt{1-E^2}$. As a results, the distribution of $u_{L,A}$ around a single bubble with terminal velocity V_T is calculated as follows:

$$u_{L,A} = V_T \sqrt{\frac{\left(1-E^2\right)\sin^2\phi_A}{\cos^2\phi_A + E^2\sin^2\phi_A}} \frac{1-E^2}{\sin^{-1}\sqrt{1-E^2} - E\sqrt{1-E^2}} \tag{C.15}$$

Bibliography

[1] *ANSYS FLUENT Theory Guide*. November 2011. URL http://www.springerlink.com/content/u13552/#section=800779&page=21&locus=97.

[2] M. Abramowitz and I. A. Stegun. *Handbook of mathematical functions with formulas, graphs, and mathematical tables*, volume 55 of *National Bureau of Standards Applied Mathematics Series*. U.S. Government Printing Office, 1964.

[3] S. P. Antal, R. T. Lahey, and J. E. Flaherty. Analysis of phase distribution in fully developed laminar bubbly two-phase flow. *International Journal of Multiphase Flow*, 17(5): 635–652, 1991.

[4] T. R. Auton. The lift force on a spherical body in a rotational flow. *Journal of Fluid Mechanics*, 183:199–218, 1987.

[5] G. K. Batchelor. *An Introduction to Fluid Dynamics*. Cambridge University Press, 1968.

[6] D. Bhaga and M. E. Weber. In-line interaction of a pair of bubbles in a viscous liquid. *Chemical Engineering Science*, 35(12):2467–2474, 1980.

[7] A. Biesheuvel and L. Van Wijngaarden. The motion of pairs of gas bubbles in a perfect liquid. *Journal of Engineering Mathematics*, 16(4):349–365, 1982.

[8] D. Bothe, M. Schmidtke, and H. J. Warnecke. VOF-simulation of the lift force for single bubbles in a simple shear flow. *Chemical Engineering & Technology*, 29(9):1048–1053, 2006.

[9] D. C. Brabston and H. B. Keller. Viscous flows past spherical gas bubbles. *Journal of Fluid Mechanics*, 69(01):179–189, 1975.

[10] J. U. Brackbill, D. B. Kothe, and C. Zemach. A continuum method for modeling surface tension. *Journal of Computational Physics*, 100(2):335–354, 1992.

[11] C. Brücker. Structure and dynamics of the wake of bubbles and its relevance for bubble interaction. *Physics of fluids*, 11:1781, 1999.

[12] B. Bunner and G. Tryggvason. Direct numerical simulations of three-dimensional bubbly flows. *Physics of Fluids*, 11(8):1967, 1999.

[13] A. D. Burns, T. Frank, I. Hamill, and J. M. Shi. The favre averaged drag model for turbulent dispersion in Eulerian multi-phase flows. In *5th international conference on multiphase flow, ICMF*, volume 4, 2004.

[14] G. P. Celata, M. Cumo, F. D'Annibale, and A. Tomiyama. The wake effect on bubble rising velocity in one-component systems. *International Journal of Multiphase Flow*, 30 (7):939–961, 2004.

[15] R. C. Chen and Y. N. Lu. The flow characteristics of an interactive particle at low Reynolds numbers. *International Journal of Multiphase Flow*, 25(8):1645–1655, 1999.

[16] R. C. Chen and J. L. Wu. The flow characteristics between two interactive spheres. *Chemical Engineering Science*, 55(6):1143–1158, 2000.

[17] R. Clift, J.R. Grace, and M. E. Weber. Bubbles, drops, and particles. Academic Press (New York), 1978.

[18] J. R. Crabtree and J. Bridgwater. Bubble coalescence in viscous liquids. *Chemical Engineering Science*, 26(6):839–851, 1971.

[19] E. de Villiers. *The potential of large eddy simulation for the modeling of wall bounded flow*. PhD thesis, Imperial College, 2006.

[20] A. W. G. de Vries. *Path and wake of a rising bubble*. University of Twente, 2001.

[21] J. W. Deardorff. The use of subgrid transport equations in a three-dimensional model of atmospheric turbulence. *Journal of Fluids Engineering*, 95:429, 1973.

[22] J. W. Deardorff. Stratocumulus-capped mixed layers derived from a three-dimensional model. *Boundary-Layer Meteorology*, 18(4):495–527, 1980.

[23] L. S. Fan and K. Tsuchiya. *Bubble wake dynamics in liquids and liquid-solid suspensions*. Butterworth-Heinemann Stoneham, 1990.

[24] B. Francesco, B. Giancarlo, M. Daniele, and V. Marco. Momentum transfer in a swarm of bubbles: estimates from fluid-dynamic simulations. *Chemical engineering science*, 59(22):5209–5215, 2004.

[25] D. Gaudlitz and N. A. Adams. Numerical investigation of rising bubble wake and shape variations. *Physics of Fluids*, 21:122102, 2009.

[26] Y. Hallez and D. Legendre. Interaction between two spherical bubbles rising in a viscous liquid. *Journal of Fluid Mechanics*, 673:406–431, 2011.

[27] J. F. Harper. On bubbles rising in line at large Reynolds numbers. *Journal of Fluid Mechanics*, 41(4):751–758, 1970.

[28] J. F. Harper. Bubbles rising in line: why is the first approximation so bad? *Journal of Fluid Mechanics*, 351:289–300, 1997.

[29] C. W. Hirt and B. D. Nichols. Volume of fluid (VOF) method for the dynamics of free boundaries. *Journal of computational physics*, 39(1):201–225, 1981.

[30] S. Hosokawa and A. Tomiyama. Multi-fluid simulation of turbulent bubbly pipe flows. *Chemical Engineering Science*, 64(24):5308–5318, 2009.

[31] M. Ishii and T. Hibiki. *Thermo-fluid dynamics of two-phase flow*. Springer, 1975.

[32] M. Ishii and N. Zuber. Drag coefficient and relative velocity in bubbly, droplet or particulate flows. *AIChE Journal*, 25(5):843–855, 1979.

[33] P. B. V. Johansson. *The axisymmetric turbulent wake*. PhD thesis, Chalmers University of Technology, 2002.

[34] J. Katz and C. Meneveau. Wake-induced relative motion of bubbles rising in line. *International Journal of Multiphase Flow*, 22(2):239–258, 1996.

[35] J. Klostermann, K. Schaake, and R. Schwarze. Numerical simulation of a single rising bubble by VOF with surface compression. *International Journal for Numerical Methods in Fluids*, 2012.

[36] J. B. W. Kok. Dynamics of a pair of gas bubbles moving through liquid: part II: experiments. *European Journal of Mechanics - B/Fluids*, 12(4):541–560, 1993.

[37] A. N. Kolmogorov. The local structure of turbulence in incompressible viscous fluid for very large Reynolds numbers. In *Dokl. Akad. Nauk SSSR*, volume 30, pages 299–303, 1941.

[38] I. Komasawa, T. Otake, and M. Kamojima. Wake behavior and its effect on interaction between spherical-cap bubbles. *Journal of Chemical Engineering of Japan*, 13(2):103–109, 1980.

[39] H. Lamb. *Hydrodynamics*. Cambridge University Press, 1932.

[40] D. N. Lee and W. A. Sirignano. Heat and momentum transfer around a pair of spheres in viscous flow. *International Journal of Heat and Mass Transfer*, 27(11):1953–1962, 1984.

[41] D. Legendre and J. Magnaudet. The lift force on a spherical bubble in a viscous linear shear flow. *Journal of Fluid Mechanics*, 368:81–126, 1998.

[42] V. G. Levich and D. B. Spalding. *Physicochemical hydrodynamics*, volume 689. Prentice-Hall Englewood Cliffs, NJ, 1962.

[43] Y. Li, J. Zhang, and L. S. Fan. Numerical simulation of gas–liquid–solid fluidization systems using a combined CFD-VOF-DPM method: bubble wake behavior. *Chemical Engineering Science*, 54(21):5101–5107, 1999.

[44] T. J. Liu. The role of bubble size on liquid phase turbulent structure in two phase bubbly flow. In *Proceedings of the 3rd International Conference on Multiphase Flow*, 1998.

[45] K. Lunde and R. J. Perkins. Shape oscillations of rising bubbles. In *In Fascination of Fluid Dynamics*, pages 387–408. Springer, 1998.

[46] J. Magnaudet and I. Eames. The motion of high-*r*eynolds-number bubbles in inhomogeneous flows. *Annual Review of Fluid Mechanics*, 32(1):659–708, 2000.

[47] M. Manga and H. A. Stone. Buoyancy-driven interactions between two deformable viscous drops. *Journal of Fluid Mechanics*, 256:647–647, 1993.

[48] C. H. Marks. Measurements of the terminal velocity of bubbles rising in a chain. *Journal of Fluids Engineering*, 95:17, 1973.

[49] C. H. Moeng. A large-eddy-simulation model for the study of planetary boundary-layer turbulence. *Journal of the Atmospheric Sciences*, 41(13):2052–2062, 1984.

[50] D. W. Moore. The boundary layer on a spherical gas bubble. *Journal of Fluid Mechanics*, 16(2):161, 1963.

[51] D. W. Moore. The velocity of rise of distorted gas bubbles in a liquid of small viscosity. *Journal of Fluid Mechanics*, 23(4):749–766, 1965.

[52] C. Morel. Turbulence modeling and first numerical simulations in turbulent two-phase flows. Technical report, CEA/Grenoble, France., 1997.

[53] G. Mougin and J. Magnaudet. Path instability of a rising bubble. *Physical Review Letters*, 88(1):014502, 2001.

[54] G. Mougin and J. Magnaudet. Wake-induced forces and torques on a zigzagging/spiralling bubble. *Journal of Fluid Mechanics*, 567:185, 2006.

[55] NAG. Fortran library manual, mark 17. *Numerical Algorithms Group, Oxford*, 1995.

[56] S. Narayanan, L. H. J. Goossens, and N. W. F. Kossen. Coalescence of two bubbles rising in line at low *r*eynolds numbers. *Chemical Engineering Science*, 29(10):2071–2082, 1974.

[57] N. Nevers and J. L. Wu. Bubble coalescence in viscous fluids. *AIChE Journal*, 17(1): 182–186, 1971.

[58] B. Ničeno, M. T. Dhotre, and N. G. Deen. One-equation sub-grid scale (SGS) modelling for Euler–Euler large eddy simulation (EELES) of dispersed bubbly flow. *Chemical Engineering Science*, 63(15):3923–3931, 2008.

[59] F. Noca. *On the evaluation of time-dependent fluid-dynamic forces on bluff bodies*. PhD thesis, California Institute of Technology, Pasadena, Cal. USA., 1997.

[60] N. M. Omran and P. J. Foster. The terminal velocity of a chain of drops or bubbles in a liquid. *Trans. Instn. Chem. Eng*, 55:171–177, 1977.

[61] M. J. Pang and J. J. Wei. Analysis of drag and lift coefficient expressions of bubbly flow system for low to medium Reynolds number. *Nuclear Engineering and Design*, 241(6): 2204 – 2213, 2011. ISSN 0029-5493.

[62] L. Prandtl. Bemerkungen zur theorie der freien turbulenz. *ZAMM*, 22:241–243, 1942.

[63] R. S. Ramachandran, T. Y. Wang, C. Kleinstreuer, and H. Chiang. Laminar flow past three closely spaced monodisperse spheres or nonevaporating drops. *AIAA journal*, 29 (1):43–51, 1991.

[64] J. Ramírez-Muñoz, A. Gama-Goicochea, and E. Salinas-Rodríguez. Drag force on interacting spherical bubbles rising in-line at large Reynolds number. *International Journal of Multiphase Flow*, 37(8):983–986, 2011.

[65] J. Ramírez-Muñoz, E. Salinas-Rodríguez, A. Soria, and A. Gama-Goicochea. Hydrodynamic interaction on large-reynolds-number aligned bubbles: Drag effects. *Nuclear Engineering and Design*, 241(7):2371–2377, 2011.

[66] P. N. Rowe and G. A. Henwood. *Drag forces in a hydraulic model of a fluidised bed*. UKAEA, 1960.

[67] H. Rusche. *Computational fluid dynamics of dispersed two-phase flows at high phase fraction*. PhD thesis, Imperial Colege, 2002.

[68] M. C. Ruzicka. On bubbles rising in line. *International Journal of Multiphase Flow*, 26 (7):1141–1181, 2000.

[69] G. Ryskin and L. G. Leal. Numerical solution of free-boundary problems in fluid mechanics. part 1. the finite-difference technique. *Journal of Fluid Mechanics*, 148:1–17, 1984.

[70] R. Rzehak and E. Krepper. CFD modeling of bubble-induced turbulence. *International Journal of Multiphase Flow*, 2013.

[71] P. G. Saffman. On the rise of small air bubbles in water. *Journal of Fluid Mechanics*, 1 (03):249–275, 1956.

[72] P. Sagaut. *Large eddy simulation for incompressible flows*, volume 3. Springer Berlin, 2000.

[73] T. Sanada, M. Watanabe, T. Fukano, and A. Kariyasaki. Behavior of a single coherent gas bubble chain and surrounding liquid jet flow structure. *Chemical Engineering Science*, 60(17):4886–4900, 2005.

[74] A. S. Sangani and A. K. Didwania. Dynamic simulations of flows of bubbly liquids at large Reynolds numbers. *Journal of Fluid Mechanics*, 250:307–337, 1993.

[75] K. Sankaranarayanan, X. Shan, I. G. Kevrekidis, and S. Sundaresan. Analysis of drag and virtual mass forces in bubbly suspensions using an implicit formulation of the lattice boltzmann method. *Journal of Fluid Mechanics*, 452:61–96, 2 2002. ISSN 1469-7645.

[76] Y. Sato and M. Sadatomi. Momentum and heat transfer in two-phase bubble flow. *International Journal of Multiphase Flow*, 7:167–177, 1981.

[77] L. Schiller and A. Naumann. A drag coefficient correlation. *Vdi Zeitung*, 77:318–320, 1935.

[78] H. Schlichting and K. Gersten. *Boundary-layer theory*. Springer, 2000.

[79] A. Serizawa and I. Kataoka. Turbulence suppression in bubbly two-phase flow. *Nuclear Engineering and Design*, 122(1):1–16, 1990.

[80] A. Serizawa, I. Kataoka, and I. Michiyoshi. Turbulence structure of air-water bubbly flow. parts i-iii. *International Journal of Multiphase Flow*, 2:221–259, 1975.

[81] M. E. Shawkat, C. Y. Ching, and M. Shoukri. Bubble and liquid turbulence characteristics of bubbly flow in a large diameter vertical pipe. *International Journal of Multiphase Flow*, 34(8):767–785, 2008.

[82] M. Simonnet, C. Gentric, E. Olmos, and N. Midoux. Experimental determination of the drag coefficient in a swarm of bubbles. *Chemical Engineering Science*, 62(3):858 – 866, 2007. ISSN 0009-2509.

[83] J. Smagorinsky. General circulation experiments with the primitive equations: I. the basic experiment. *Monthly weather review*, 91(3):99–164, 1963.

[84] A. Sokolichin and G. Eigenberger. Gas-liquid flow in bubble columns and loop reactors: Part I: detailed modelling and numerical simulation. *Chemical Engineering Science*, 49 (24):5735–5746, 1994.

[85] C. W. Stewart. Bubble interaction in low-viscosity liquids. *International Journal of Multiphase Flow*, 21(6):1037–1046, 1995.

[86] H. Tennekes and J. L. Lumley. *A first course in turbulence*. The MIT press, 1972.

[87] A. Tomiyama, I. Kataoka, I. Zun, and T. Sakaguchi. Drag coefficients of single bubbles under normal and micro gravity conditions. *JSME international journal. Series B, fluids and thermal engineering*, 41(2):472–479, 1998.

[88] A. Tomiyama, G. P. Celata, S. Hosokawa, and S. Yoshida. Terminal velocity of single bubbles in surface tension force dominant regime. *International Journal of Multiphase Flow*, 28(9):1497–1519, 2002.

[89] M. Toshiro, K. Satoru, and T. Teruo. Studies on chains of bubbles rising through quiescent liquid. *The Canadian Journal of Chemical Engineering*, 62(2):186–193, 1984.

[90] A. A. Troshko and Y. A. Hassan. A two-equation turbulence model of turbulent bubbly flows. *International Journal of Multiphase Flow*, 27(11):1965–2000, 2001.

[91] H. Tsuge and S. Hibino. *The motion of gas bubbles generating from a single orifice submerged in a liquid*. Faculty of Engineering, Keio University, 1972.

[92] H. Tsuge and S. Hibino. The onset conditions of oscillatory motion of single gas bubbles rising in various liquids. *Journal of Chemical Engineering of Japan*, 10(1):66–68, 1977.

[93] P. F. Vassallo and R. Kumar. Liquid and gas velocity measurements using LDV in air–water duct flow. *Experimental Thermal and Fluid Science*, 19(2):85–92, 1999.

[94] R. M. Wellek, A. K. Agrawal, and A. H. P. Skelland. Shape of liquid drops moving in liquid media. *AIChE Journal*, 12(5):854–862, 1966.

[95] D. C. Wilcox. *Turbulence modeling for CFD*, volume 2. DCW industries La Canada, 1998.

[96] M. Wu and M. Gharib. Path instabilities of air bubbles rising in clean water. *arXiv preprint patt-sol/9804002*, 1998.

[97] A. Yoshizawa and K. Horiuti. A statistically-derived subgrid-scale kinetic energy model for the large- eddy simulation of turbulent flows. *Journal of the Physical Society of Japan*, 54:2834–2839, 1985.

[98] H. Yuan and A. Prosperetti. On the in-line motion of two spherical bubbles in a viscous fluid. *Journal of Fluid Mechanics*, 278:325–350, 1994.

[99] D. Zhang, N. G. Deen, and J. Kuipers. Numerical simulation of the dynamic flow behavior in a bubble column: a study of closures for turbulence and interface forces. *Chemical Engineering Science*, 61(23):7593–7608, 2006.

[100] J. Zhang and L. S. Fan. A semianalytical expression for the drag force of an interactive particle due to wake effect. *Industrial & Engineering Chemistry Research*, 41(20):5094–5097, 2002.

[101] J. Zhang and L. S. Fan. On the rise velocity of an interactive bubble in liquids. *Chemical Engineering Journal*, 92(1):169–176, 2003.